20000 km

GNSS

1000 km

800 km

SAR

12 km

MARION HEUBLEIN

FADWA ALSHAWAF

MICHAEL MAYER

STEFAN HINZ

BERNHARD HECK

Towards a rigorous fusion of GNSS and InSAR observations for the purpose of water vapor retrieval

KIT Scientific Publishing

Marion Heublein, Fadwa Alshawaf, Michael Mayer, Stefan Hinz, Berhard Heck

**Towards a rigorous fusion of GNSS and
InSAR observations for the purpose of
water vapor retrieval**

Towards a rigorous fusion of GNSS and InSAR observations for the purpose of water vapor retrieval

by
Marion Heublein
Fadwa Alshawaf
Michael Mayer
Stefan Hinz
Berhard Heck

KIT Scientific Publishing

Abstract

Incompletely or incorrectly modeled atmospheric effects limit the quality of the exploitation of observations of space-based geodetic sensors, such as GNSS (Global Navigation Satellite Systems) and InSAR (Interferometric Synthetic Aperture Radar). In contrast, state variables of the Earth's atmosphere, especially water vapor, contain valuable information for climate research and weather forecasting.

The Institute of Photogrammetry and Remote Sensing (IPF) and the Geodetic Institute (GIK) of the Karlsruhe Institute of Technology (KIT) carried out various research for atmospheric water vapor retrieval. For further investigations, we focus on the quality of water vapor estimates from the geodetic sensors GNSS and InSAR. Surface meteorological information is taken into account for the described analysis. Data from the MEdium Resolution Imaging Spectrometer (MERIS) are used for validating our estimates. The area under investigation is the Upper Rhine Graben (URG), which is covered by the dense GNSS network GURN (GNSS Upper Rhine Graben Network) since 2002. A stack of 17 Envisat SAR acquisitions was available. These SAR data cover a $100 \text{ km} \times 100 \text{ km}$ region in the URG. The SAR images were acquired between 2003 and 2008, but most of them are concentrated in the year 2005.

The described project aims at a straightforward comparison of the wet delay, caused by water vapor, derived from GNSS and InSAR. Therefore, the InSAR neutrospheric phase has to be separated from other components contained in InSAR measurements. For this purpose, it is assumed that the surface deformation within the area under investigation is negligible during the considered period of time. In the case of InSAR, persistent scatterer interferometry is used and leads to the observation of differential wet delays. Within the GNSS data processing, the Precise Point Positioning (PPP) approach is applied to estimate the total neutrospheric path delay. The total path delay deduced from GNSS is composed of a prediction model, estimated site-specific neutrosphere parameters (SSNP), and horizontal neutrospheric gradients as well as observation residuals.

Based on an additional, comparative GNSS study carried out with respect to the predicting Niell mapping function (NMF), the effect of the weather model based Vienna mapping function (VMF) on the GNSS results is evaluated. Most important findings of the GNSS-related research of this work are: The SSNP deduced by means of the VMF attain smaller values than those derived from NMF. However, their effect on the total wet delay is significant and they may not be neglected. On the contrary, independent of the mapping function, the effect of the estimated horizontal gradients deduced from observations down to $3°$ elevation is classified as insignificant with regard to path delays observed at elevation angles above $45°$ (InSAR elevation angle: about $65.5°$). However, the phase residuals contribution to the satellite-directed path delays is very important. The annual standard deviations of the site height components determined within the GNSS data processing based on NMF have larger values than those based on the VMF. In contrast, the site latitudes and longitudes based on the NMF and VMF remain unchanged at the representative sample of GNSS sites.

Comparisons of GNSS observations with the satellite-directed InSAR data show that only a partial component of the wet delay remains after the interferogram formation. A comparison with partial neutrospheric delays deduced from MERIS shows strong agreement between InSAR and MERIS data. This implies that a topography-dependent component as well as a linear trend contained in the wet delay from MERIS or GNSS have to be reduced to emulate the partial wet delays from InSAR.

Zusammenfassung

Unvollständig oder ungenau erstellte Modelle atmosphärischer Effekte schränken die Qualität geodätischer Weltraumverfahren wie GNSS (Globale Satelliten-Navigationssysteme) und InSAR (Interferometrisches Radar mit synthetischer Apertur) ein. Andererseits enthalten Zustandsgrößen der Erdatmosphäre, allen voran Wasserdampf, wertvolle Informationen für Klimaforschung und Wettervorhersage, welche aus GNSS- oder InSAR-Beobachtungen abgeleitet werden können.

Bislang wurden am Institut für Photogrammetrie und Fernerkundung (IPF) und am Geodätischen Institut (GIK) des Karlsruher Instituts für Technologie (KIT) schon mehrere Forschungsprojekte im Bereich der atmosphärischen Wasserdampfmodellierung realisiert, und auch die vorliegende Arbeit beschäftigt sich mit diesem Thema. Im Besonderen legt diese Arbeit Augenmerk auf einen bisher fehlenden, stringenten Vergleich der geodätischen Sensoren GNSS und InSAR. Zudem werden meteorologische Informationen und Daten des Erdbeobachtungssystems MERIS (Medium REsolution Imaging Spectrometer) genutzt. Untersucht wurde das Gebiet des Oberrheingrabens, welches seit 2002 über ein dichtes Netz an GNSS-Stationen verfügt. Neben den GNSS-Beobachtungen innerhalb dieses GNSS Upper Rhine Graben Network (GURN) stand ein Stack von 17 Envisat SAR-Aufnahmen zur Verfügung. Diese SAR-Daten decken eine 100 km × 100 km große Region im Oberrheingraben ab. Die meisten SAR-Bilder wurden im Jahr 2005 aufgenommen, doch es lagen auch Aufnahmen von einzelnen Tagen der Jahre 2003, 2004, und 2006 bis 2008 vor.

Im Rahmen dieser Arbeit wurde ein direkter Vergleich von GNSS und InSAR in Richtung des SAR-Satelliten durchgeführt. Hierbei wurden die Beiträge der beiden Sensoren zur feuchten Laufzeitverzögerung der Radiowellen-Signale gegenübergestellt. Die in den Interferogrammen enthaltene neutrosphärische Phase wurde für diesen Vergleich getrennt von anderen in den InSAR-Beobachtungen enthaltenen Komponenten und im Folgenden mit den GNSS-Messungen verglichen. Um eine solche Trennung der InSAR-Phasenanteile vornehmen zu können, wurde davon ausgegangen, dass im Beobachtungszeitraum keine signifikanten Deformationen des Oberrheingrabens auftraten. Die nach der Persistent Scatterer Methode durchgeführten InSAR-Prozessierungen ermöglichten die Messung von differentiellen feuchten Laufzeitverzögerungen. Im Vergleich hierzu wurde im Rahmen der GNSS-Auswertung Precise Point Positioning (PPP) genutzt, wodurch totale neutrosphärische Laufzeitverzögerungen bestimmt werden konnten. Solche über GNSS bestimmte totale Laufzeitverzögerungen setzen sich zusammen aus einem A priori-Modell, geschätzten stationsspezifischen Neutrosphärenparametern (SSNP), horizontalen Gradienten und Beobachtungsresiduen.

Die Auswirkungen der beiden zusätzlich untersuchten prädizierenden und Wettermodell-basierten Projektionsfunktionen "Niell mapping function" (NMF) und "Vienna mapping function" (VMF) auf die über GNSS bestimmten Koordinaten, die SSNP und die horizontalen Gradienten wurden vergleichend analysiert. Für den Bereich GNSS ist besonders hervorzuheben: Die anhand der VMF bestimmten SSNP ergeben kleinere Werte als jene, die über die NMF berechnet wurden. Trotzdem ist der Effekt der SSNP auf die feuchte Laufzeitverzögerung signifikant und darf demnach nicht vernachlässigt werden. Im Gegensatz hierzu können die Effekte der Gradienten, die aus Beobachtungen bis zu einer minimalen Elevation von 3° stammen, unabhängig von der Projektionsfunktion für Elevationen über 45° vernachlässigt werden. Der Beitrag der Phasenresiduen zur Laufzeitverzögerung in Signalrichtung hingegen ist bedeutend. Im Falle einer GNSS-Auswertung basierend auf der NMF variieren die Stationshöhen über den Zeitraum eines Jahres stärker als im Falle einer auf der VMF beruhenden Berechnung. Längen und Breiten der repräsentativ ausgewählten Stationen stimmen für beide Projektionsfunktionen überein.

Vergleiche der GNSS-Beobachtungen in Richtung des SAR-Satelliten mit den InSAR-Aufnahmen zeigen, dass nur ein partieller Anteil der feuchten Laufzeitverzögerung in den Interferogrammen enthalten ist. Aus MERIS-Beobachtungen abgeleitete partielle feuchte Laufzeitverzögerungen stimmen gut mit jenen des SAR-Sensors überein und veranschaulichen, dass ein höhenabhängiger Anteil der feuchten Laufzeitverzögerung sowie ein in MERIS- und GNSS-Beobachtungen vorliegender linearer Trend innerhalb der InSAR-Prozessierung wegfallen.

Contents

1 Motivation

In its global analysis for 2013, the U.S. National Oceanic and Atmospheric Administration declared that the past year represented, jointly with the year 2003, the fourth warmest year globally since the begin of the records in 1880. Only in the years 1998, 2005, and 2010 higher annual mean temperatures were observed. The U.S. National Space Agency classified the year 2013 slightly different and designated it to be on rank seven of the warmest years ever recorded. However, scientists agree on explaining this phenomenon by a sustained climate change causing global warming. The media report more and more about melting antarctic ice shields, rising sea levels, droughts, and increasing mean temperatures. In January, the newspaper "Süddeutsche Zeitung" stated that according to an internal paper of the Intergovernmental Panel on Climate Change, only 15 years were left to take effective and still affordable actions against climate change. Some weeks later, Reuters reported about the decision of the U.S. and China to work together for the attenuation of climate change. Wildlife diversity, the world's economy, and peaceful living conditions devoid of social conflicts depend largely on the evolution of our living planet's climate. Global warming is generally ascribed to the greenhouse effect, and in this context the amount of carbon dioxide (CO_2) emitted is particularly criticized. However, water vapor is the most abundant greenhouse gas (60 times larger than CO_2); therefore, its effect on climate and weather forecasting is of great importance.
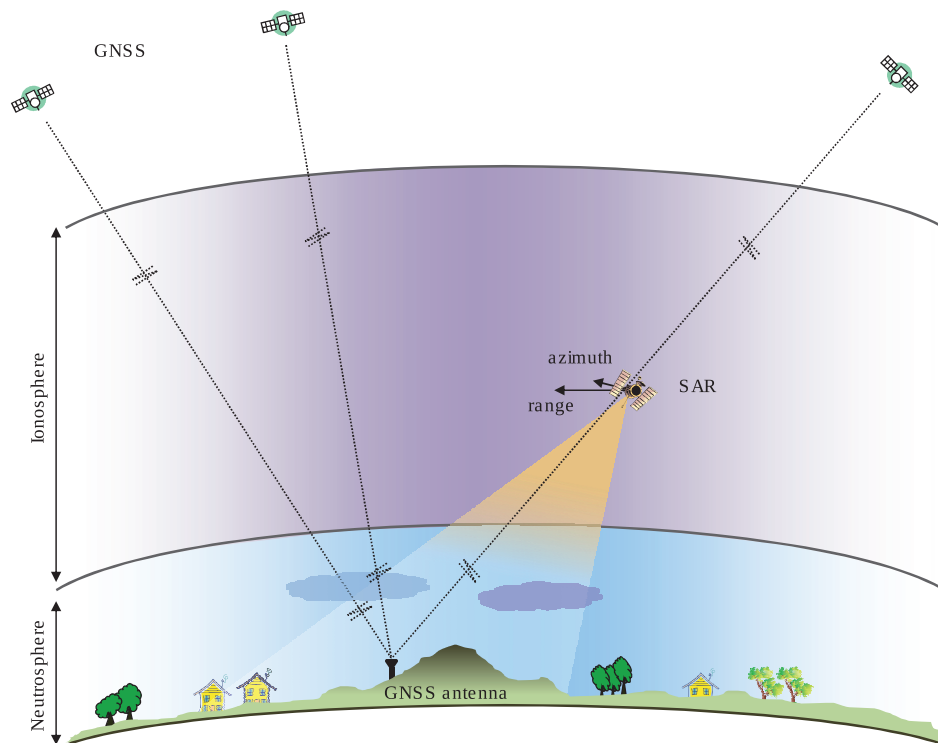
Figure 1.1: Viewing geometry and spatial coverage of GNSS and (In)SAR from Alshawaf [2013]

Water vapor represents a spatially and temporally highly variable constituent of the Earth's atmosphere. Its modeling is a big challenge for meteorologists, climatologists, and geodesists. Many different measurement techniques ranging from ground-based radars and meteorological registering balloons over radiosonde observations and measurements of satellite-based imaging spectrometers to Global Navigation Satellite Systems (GNSS) and Interferometric Synthetic Aperture Radar (InSAR) are used in order to observe the actual amount and distribution of water

vapor. Besides, empirical and numerical climate and weather models try to approximate and forecast the water vapor content. Not only it is possible to deduce valuable information for climate research and weather forecasting from GNSS and InSAR observations, but correctly modeled atmospheric effects also improve the quality of the observations from these space-based geodetic sensors.

In addition, in order to obtain precise information about surface deformation from InSAR data, the phase observations have to be corrected for orbit inaccuracies, surface topography, and the atmospheric delay between the two passes of the satellite. In contrast, if no deformation is assumed and if orbital ramps and topographic phases are reduced, information on the atmospheric delay difference can be extracted from the InSAR observations. Correspondingly, GNSS' precise point positioning techniques can only yield high precision coordinates with standard deviations in the range of several millimeters to centimeters, if all parameters affecting the GNSS signals are sufficiently reduced. Water vapor still represents one of the main limiting factors in Precise Point Positioning (PPP) using carrier phase measurements. Vice versa, assuming all other influencing parameters as known, an absolute modeling of the neutrospheric delay becomes possible based on GNSS observations.

The long-term goal of the research carried out by the working groups of IPF and GIK is the fusion of geodetic and additional meteorological data, e.g., from the MEdium Resolution and Imaging Spectrometer (MERIS), combining the benefits of each input data set. GNSS data are continuous with a high temporal observing rate, whereas the strength of InSAR is the high spatial resolution and the wide spatial coverage shown in Figure 1.1.

Chapter 2 provides basic information on the Earth's atmosphere and its impact on radio wave propagation. Different subdivisions of the atmosphere are explained and the most common model for the neutrospheric path delay affecting radio wave propagation is given. In the following chapter, emphasis is put on the neutrospheric delays in GNSS observations. Niell and Vienna mapping functions are explained and their effects on GNSS observables are compared. Then, chapter 4 introduces the used InSAR data sets and the approach of Persistent Scatterer Interferometry with the Stanford Method. InSAR interferometric phases are converted to neutrospheric delays and validated with MERIS data. Different master selection criteria are analyzed and an enhanced master selection algorithm based on the approach of Hooper et al. [2007] is introduced. A comparison of the wet delays deduced from GNSS and InSAR data is performed in chapter 5, and finally, an outlook on remaining questions and future work is given.

2 The Earth's atmosphere and its impact on radio wave propagation

The Earth's atmosphere can be subdivided into different layers. Different approaches for the classification of atmospheric layers are presented in section 2.1. The atmospheric effects on radio wave propagation are explained in section 2.2. Finally, section 2.3 provides an introduction into modeling of the neutrospheric delay.

2.1 Common subdivisions of the atmosphere

In meteorology, the variation of temperature with the height is used to distinguish the troposphere, stratosphere, mesosphere, thermosphere, and exosphere, as illustrated in Figure 2.1. Low tropospheric layers are characterized by their negative temperature gradient and extend up to about $10 - 12$ km, where an absolute temperature of about $-57\,^{\circ}$C is reached. According to Kraus [2004], the temperature initially stays co0nstant beyond the so-called tropopause, which represents the upper limit of the troposphere. The temperature starts then increasing up to about $0\,^{\circ}$C within the stratosphere. The stratosphere is limited by the stratopause and is followed by the mesosphere in which temperature decreases to about $-100\,^{\circ}$C at a height of about 80 km. In the higher atmospheric regions, above the mesopause, positive temperature gradients are observed again. Temperatures rise up to 1000 K in the thermosphere that extends up to about 400 km height and then stay approximately constant. Finally, the exosphere, that is separated from the thermosphere by the thermopause, fades away into interplanetary space at a height of about $500 - 600$ km or 800 km. These indications vary in meteorological literature, compare e.g. Kraus [2004] and Malberg [2007].
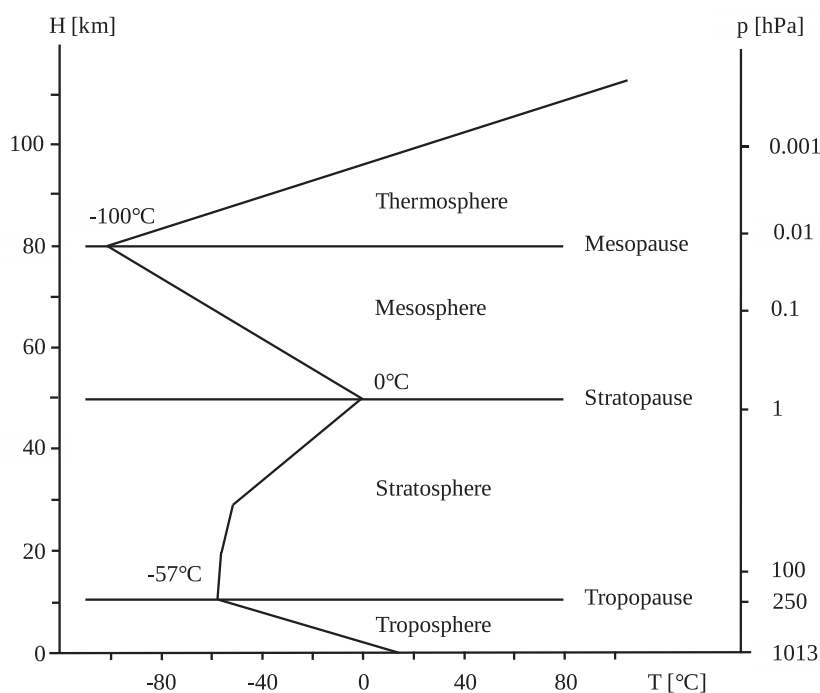

Figure 2.1: Subdivisions of the atmosphere according to Malberg [2007]

Another way to deal with the atmosphere is a distinction depending on the occurring density of free electrons. Next to the Earth's surface, up to heights of about 50 km, the ionization is virtually absent (Seeber [2003]); therefore, this region – mainly consisting of troposphere and stratosphere – is called the neutral atmosphere (neutrosphere). Above this neutrospheric layer, a significant density of free electrons is observed within the ionosphere that extends up to about 1000 km. In the following, this latter subdivision will be used because atmospheric effects mainly differ according to the ionization of the considered layer.

2.2 Atmospheric effects on radio wave propagation

Within the ionosphere, frequency dependent effects on GNSS signal propagation are observed. According to Hofmann-Wellenhof et al. [2001], linear combinations of dual resp. multi-frequency measurements can be used to dispersively eliminate the first order ionospheric effects (e.g., $f_{GPS,1} = 1575.42$ MHz, $f_{GPS,2} = 1227.60$ MHz). On the contrary, the neutrosphere is non-dispersive for frequencies below 15 GHz as indicated in Hofmann-Wellenhof et al. [2001]. Hence, it is not possible to eliminate neutrospheric refraction using similar methods. Not only does the neutrosphere cause a bending of the ray path, especially at low elevations (see Figure 2.2), but it also provokes a lower signal propagation velocity.
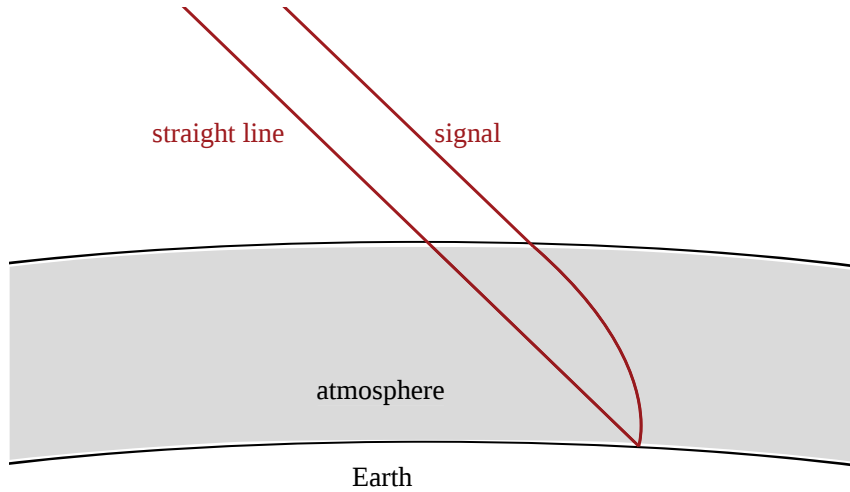
Figure 2.2: Continuously bent ray path in the neutrosphere, as described in Boehm [2004]

Due to gas molecules in the atmosphere, the refractive index $n(s)$ of the neutrosphere along the signal transmitting path s differs from that in vacuum (Forssell [2008]). The refractive index hence takes a value slightly greater than unity and is not constant because the neutrosphere is not a homogeneous medium. According to Fermat's principle cited in Hofmann-Wellenhof et al. [2001], variations in $n(s)$ result in a curved ray path deviating from the straight line. For numerical reasons, the refractivity $N(s)$ is introduced instead of the refraction index, i.e.

$$N(s) = (n(s) - 1) \cdot 10^6 \tag{2.1}$$

and accordingly

$$n(s) = 10^{-6} \cdot N(s) + 1 \tag{2.2}$$

Integrating along the signal path, the metric neutrospheric path delay Δ is

$$\Delta = \int n(s)ds - \int ds. \tag{2.3}$$

This yields, when neglecting the influence of the bending:

$$\Delta = \int \left(10^{-6} \cdot N(s) + 1\right) ds - \int ds = 10^{-6} \int N(s)ds + \int ds - \int ds = 10^{-6} \int N(s)ds \tag{2.4}$$

According to Hofmann-Wellenhof et al. [2001], the integration of the total delay from (2.4) is implemented by means of numerical methods or analytically after, for example, series expansions of the integrand. The first term $\int n(s)ds$ in (2.3) represents the bent propagation path shown in Figure 2.2, whereas the second term $\int ds$ stands for the straight line that the signal would take if the neutrospheric index equaled unity, i.e., if the atmosphere was a vacuum.

In a further step, the refractivity N can be subdivided into two parts — the dry refractivity N_{dry} and the wet refractivity N_{wet} – corresponding to the dry and wet neutrospheric delays, respectively.

$$N = N_{dry} + N_{wet} \tag{2.5}$$

Other approaches rather distinguish a hydrostatic (N_h) and a non-hydrostatic (N_{nh}) part of the neutrospheric delay, referring to atmospheric gases in hydrostatic equilibrium.

$$N = N_h + N_{nh} \tag{2.6}$$

About 90% of the total delay are related to the dry neutrospheric gases Nitrogen (78%), Oxygen (21%), and Argon (0.9%). Their effects result in the dry delay

$$\Delta_{dry} = 10^{-6} \cdot \int N_{dry}(s)ds \tag{2.7}$$

whereas only 10% of the neutrospheric delay arise from the wet resp. non-hydrostatic component caused by the dipolar momentum refraction of water vapor mentioned in Bevis et al. [1992]:

$$\Delta_{wet} = 10^{-6} \cdot \int N_{wet}(s)ds \tag{2.8}$$

The dry component introduced in (2.7) can easily be modeled from the air pressure measured at the observing site. The wet component from (2.8) varies much more in both time and space and hence, its precise computation is a big challenge. Leick [2004] mentiones values for the zenith wet delay of about 40 cm. The total neutrospheric delay reaches up to about 2.4 m at sea level.

Note that the term "troposphere" is often used instead of the term "neutrosphere" introduced in 2.1 when dealing with the sum of path delays originating from the non-significantly ionized, low atmospheric layer. To stay consistent, only the term "neutrosphere" will be used within this thesis.

Furthermore, the bending effect within the neutrosphere will be neglected and ionospheric effects will not be considered in more detail. In GNSS PPP, ionospheric effects are reduced within the Berner GPS Software (Bernese) by using the ionosphere-free linear combination L_3 from (2.9), as described in Dach et al. [2007].

$$L_3 = \frac{1}{f_1^2 - f_2^2} \cdot \left(f_1^2 \cdot L_1 - f_2^2 \cdot L_2 \right) \tag{2.9}$$

Here, L_1 and L_2 stand for the phase observables at the GPS (Global Positioning System) frequencies f_1 and f_2. According to Doin et al. [2009], InSAR acquisitions from C-band Envisat SAR at $\lambda = 0.0562356$ m are much less affected by the ionosphere than L-band observations of GNSS. Moreover, the ionospheric activity in the considered period of time (around 2005) is rather small as observed from Figure 2.3. Therefore, within this work, it is assumed that the ionospheric effects in GNSS and InSAR observations are negligible.

2.3 Modeling the neutrospheric delay

There are different models for computing the total delay caused by neutrospheric refraction. The neutrospheric path delay can be calculated based on the refractivity, if spatially sufficiently resolved meteorological parameters as well as empirical constants are available (Mayer [2006]). There are also approaches for the determination of N
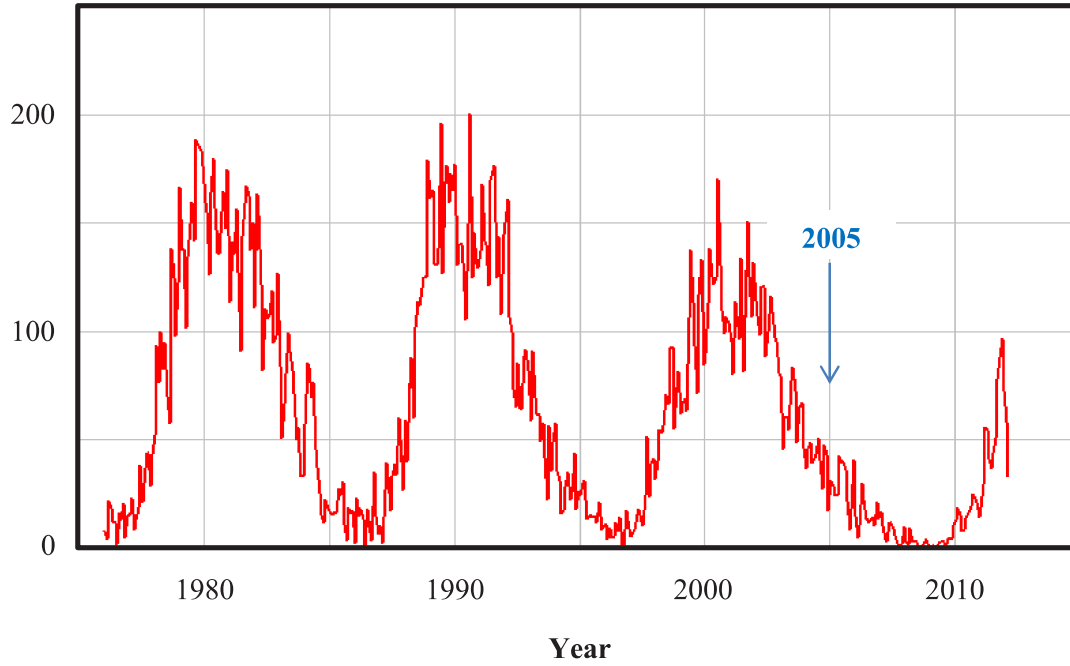
Figure 2.3: Monthly sunspot numbers from the Solar Influences Data Analysis Center (SIDC)

by ray-tracing or as a function of the height and surface meteorological data. The most common model related to neutrospheric effects on GNSS observations is that of Saastamoinen [1973].

Saastamoinen developed an approach for the determination of the total neutrospheric delay relying on site height and latitude φ, zenith angle, temperature, total barometric pressure, and partial pressure of water vapor (Saastamoinen [1973], formula 56b):

$$\Delta = \frac{0.002277 \cdot D}{\cos z} \cdot \left[p_0 + \left(\frac{1255}{T_0} + 0.05 \right) \cdot e_0 - B \cdot \tan^2 z \right] + \Delta_R \tag{2.10}$$

where

z	zenith angle
p_0	total barometric pressure at the surface in [mb]
T_0	temperature at the surface in [K]
e_0	partial pressure of water vapor at the surface in [mb]

The components D, B, and Δ_R are correction terms, where D is calculated from the formula

$$D = 1 + 0.0026 \cdot \cos 2\varphi + 0.00028 \cdot H \tag{2.11}$$

while B and Δ_R are taken from lookup tables depending on the site height H, or on the site height H and on the zenith angle z, respectively.

At most GNSS sites no meteorological parameters are observed that could be used to derive representative values for p_0, T_0, and e_0. That is why Dach et al. [2007] deduce these necessary input values from standard atmospheres (Berg [1948]). The relations between the total barometric pressure p_0 in mb, temperature T_0 in °C, and the relative humidity rh_0 in % at a certain surface height H in m and their corresponding initial values p_{H_0}, T_{H_0}, and rh_{H_0} at sea level H_0 are:

$$p_0 = p_{H_0} \cdot (1 - 0.0000226 \cdot (H - H_0))^{5.225}$$
$$T_0 = T_{H_0} - 0.0065 \cdot (H - H_0) \tag{2.12}$$
$$rh_0 = rh_{H_0} \cdot \exp\left(-0.0006396 \cdot (H - H_0)\right)$$

According to Xu [2003], values of the partial pressure e of water vapor result from the relative humidity in (2.12) by means of

$$e = \frac{rh}{100} \cdot exp\left(-37.2465 + 0.213166 \cdot T - 0.000256988 \cdot T^2\right) \tag{2.13}$$

with temperature T introduced in K and the relative humidity rh in %.

Within this thesis, the reference height H_0 and the reference values p_{H_0}, T_{H_0}, and rh_{H_0} for the extrapolation of the standard atmosphere are set to:

$$\begin{aligned} H_0 &= 0 \text{ m} \\ p_{H_0} &= 1013.25 \text{ mb} \\ T_{H_0} &= 18\,^\circ\text{C} \\ rh_{H_0} &= 50\% \end{aligned} \tag{2.14}$$

Up to now, only models for total neutrospheric delays have been introduced. Bernese models the hydrostatic component of these total delays by setting the relative humidity to zero, which yields a partial pressure of water vapor of $e = 0$ (2.13). This results in the hydrostatic and non-hydrostatic delays Δ_h and Δ_{nh} from Saastamoinen, each given in meter:

$$\begin{aligned} \Delta_h &= \frac{0.002277 \cdot D}{\cos z} \cdot \left[p_0 - B \cdot \tan^2 z\right] \\ \Delta_{nh} &= \frac{0.002277 \cdot D}{\cos z} \cdot \left[\left(\frac{1255}{T_0} + 0.05\right) \cdot e_0\right] \end{aligned} \tag{2.15}$$

Comparing the results of the above equation (2.15) with the equations distinguishing between the dry and the wet delays Δ_{dry} and Δ_{wet} as in Mayer [2006]

$$\begin{aligned} \Delta_{dry} &= \frac{0.002277 \cdot D}{\cos z} \cdot \left[p_0 - 0.155471 \cdot e_0 - B \cdot \tan^2 z\right] + \Delta_R \\ \Delta_{wet} &= \frac{0.002277 \cdot D}{\cos z} \cdot \left[\frac{1255}{T_0} + 0.205471\right] \cdot e_0 \end{aligned} \tag{2.16}$$

it can be noticed that the difference between "dry" and "hydrostatic", when ignoring the term Δ_R, is very small. Assuming a relative humidity of 50%, a temperature of 15 °C, and a total barometric pressure of 1010 mb in Karlsruhe ($\varphi \approx 49°$, $H \approx 115$ m), a delay difference of 0.01 mm between "dry" and "hydrostatic" is obtained for a satellite at $\varepsilon = 70°$ elevation. The difference in the wet or non-hydrostatic component attains similar values.

Of course,

$$\Delta_{total:\ dry+wet} = \Delta_{dry} + \Delta_{wet} = \Delta_h + \Delta_{nh} = \Delta_{total:\ h+nh} \tag{2.17}$$

holds when separating the total delay into its components.

Due to the difficulty in precisely modeling the wet component of the neutrospheric delay, this part of the delay is often estimated within a least squares adjustment instead of computing its value from models. As Bernese does not handle these notations consistently, neither "dry" - "wet" nor "hydrostatic" - "non-hydrostatic" are completely proper. For clearness, only the notations "dry" and "wet" will be kept in the following.

3 Neutrospheric delay within GNSS data

As introduced in section 2.2, GNSS observations are subject to neutrospheric refraction. It has also been explained how the neutrospheric delay is related to the refractivity $N(s)$ along the signal path s. As the value of $N(s)$ at the different positions along the ray path is unknown, the delay has been determined by other means in section 2.3. In the equations (2.15) and (2.16), the term $1/\cos z = 1/\sin \varepsilon$ represents a mapping of the zenith delay values Δ^{zenith} to any zenith angle z corresponding to an elevation $\varepsilon = 90° - z$ of the considered satellite resulting in Δ^{slant}. However, the mapping scheme illustrated in Figure 3.1 can only be seen as a rough approximation and does not yield accurate results at low elevation angles, especially.
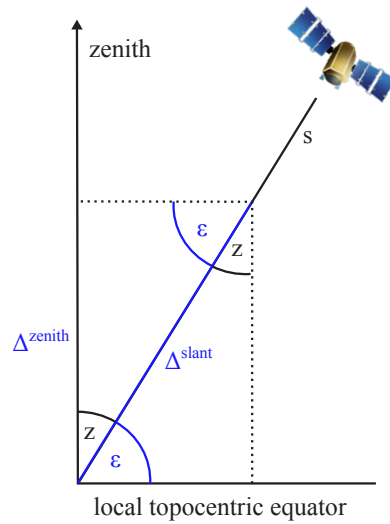
Figure 3.1: $1/\sin \varepsilon$ mapping

Different neutrospheric mapping functions and their effects on parameters derived from GNSS observables are therefore introduced and compared in the sections 3.1 and 3.4. Section 3.3 outlines the applied precise point positioning approach and explains how the considered observing sites have been selected.

3.1 Neutrospheric mapping functions in GNSS data processing

In the previous chapter zenith neutrospheric delays have been calculated and above, a simple mapping by means of the equation

$$\Delta^{slant}(\varepsilon) = \frac{\Delta^{zenith}}{\sin \varepsilon} \tag{3.1}$$

has been applied. For observations at lower elevation angles, the neutrospheric path delay increases because the signal path through the neutrospheric layers is longer and the water vapor content is higher, compared to that in the zenith direction. However, the bending effect at low elevations is poorly modeled by (3.1). Therefore, the Niell and Vienna Mapping Functions (NMF and VMF) allow the computation of slant delays based on delays in the zenith

direction. The effects of these mapping functions on parameters derived from GNSS observables are introduced and compared in this section. In general, a mapping function $mf(\varepsilon)$ can be described by

$$\Delta^{slant}(\varepsilon) = mf(\varepsilon) \cdot \Delta^{zenith} \tag{3.2}$$

projecting the zenith delay into a slant delay at an elevation angle ε. As in (2.17), this can again be split into:

$$\Delta^{slant} = mf_{dry}(\varepsilon) \cdot \Delta_{dry}^{slant} + mf_{wet}(\varepsilon) \cdot \Delta_{wet}^{slant} \tag{3.3}$$

As indicated in Boehm [2004], both mapping functions NMF and VMF are based on the Marini continued-fraction form extending the simple mapping of the zenith delay using $mf(\varepsilon) = \dfrac{1}{\sin \varepsilon}$

$$mf(\varepsilon) = \cfrac{1 + \cfrac{a}{1 + \cfrac{b}{1 + c}}}{\sin \varepsilon + \cfrac{a}{\sin \varepsilon + \cfrac{b}{\sin \varepsilon + c}}} \tag{3.4}$$

However, they differ in the

- values used for the zenith delay

- determination of the coefficients a, b, and c.

Independent of the choice of the mapping function, there are two different mapping functions for the corresponding dry and wet delay components.

3.1.1 Niell Mapping Function

Niell Mapping Functions use zenith delays computed following the model of Saastamoinen presented in section 2.3. In the case of the dry part of the atmospheric delay, Boehm [2004] deduce the coefficients a, b, and c in (3.4) by applying (3.5) with tabulated values for a_{avg}, b_{avg}, c_{avg}, a_{amp}, b_{amp}, and c_{amp}. According to Niell [1996], these latter coefficients, that can be found in Table 3.1, are determined based on radiosonde observations in 1987 and 1988 at four different sites and three representative heights in the atmosphere. Hence, they cannot represent actual and highly variable weather patterns.

$$a_{dry}(\varphi, DOY) = a_{avg}(\varphi) + a_{amp}(\varphi) \cdot \sin\left(2\pi \cdot \frac{DOY - DOY_0}{365.25}\right)$$

$$b_{dry}(\varphi, DOY) = b_{avg}(\varphi) + b_{amp}(\varphi) \cdot \sin\left(2\pi \cdot \frac{DOY - DOY_0}{365.25}\right) \tag{3.5}$$

$$c_{dry}(\varphi, DOY) = c_{avg}(\varphi) + c_{amp}(\varphi) \cdot \sin\left(2\pi \cdot \frac{DOY - DOY_0}{365.25}\right)$$

with DOY being the analyzed Day Of Year and DOY_0 equaling either 28 in case of the northern hemisphere, or 211 if the southern hemisphere is considered. The value of 211 results from the rounded value of

$$DOY_{0\ south} = DOY_{0\ north} + \frac{365.25}{2} \tag{3.6}$$

that is calculated within the module S_NMFDRY.f in Bernese.

In addition, a correction term Δmf_{dry} to account for the height of the observing site, for which the delay is calculated, has to be added within the modeling of the dry component of the mapping function, such that

$$\Delta mf_{dry} = H \cdot \left(\frac{1}{\sin(\varepsilon)} - f(\varepsilon, a_H, b_H, c_H)\right) \tag{3.7}$$

Table 3.1: Coefficients of the dry NMF as a function of the site latitude φ according to Boehm [2004]

	$\varphi = 15°$	$\varphi = 30°$	$\varphi = 45°$	$\varphi = 60°$	$\varphi = 75°$
a_{avg}	$1.2769934 \cdot 10^{-3}$	$1.2683230 \cdot 10^{-3}$	$1.2465397 \cdot 10^{-3}$	$1.2196049 \cdot 10^{-3}$	$1.2045996 \cdot 10^{-3}$
b_{avg}	$2.9153695 \cdot 10^{-3}$	$2.9152299 \cdot 10^{-3}$	$2.9288445 \cdot 10^{-3}$	$2.9022565 \cdot 10^{-3}$	$2.9024912 \cdot 10^{-3}$
c_{avg}	$62.610505 \cdot 10^{-3}$	$62.837393 \cdot 10^{-3}$	$63.721774 \cdot 10^{-3}$	$63.824265 \cdot 10^{-3}$	$64.258455 \cdot 10^{-3}$
a_{amp}	0.0	$1.2709626 \cdot 10^{-5}$	$2.6523662 \cdot 10^{-5}$	$3.4000452 \cdot 10^{-5}$	$4.1202191 \cdot 10^{-5}$
b_{amp}	0.0	$2.1414979 \cdot 10^{-5}$	$3.0160779 \cdot 10^{-5}$	$7.2562722 \cdot 10^{-5}$	$11.723375 \cdot 10^{-5}$
c_{amp}	0.0	$9.0128400 \cdot 10^{-5}$	$4.3497037 \cdot 10^{-5}$	$84.795348 \cdot 10^{-5}$	$170.37206 \cdot 10^{-5}$

The coefficients a_H, b_H, and c_H are given in Table 3.2, H is the height of the respective observing site in km, and ε is the elevation angle.

Table 3.2: Coefficients for the height correction of dry NMF according to Boehm [2004]

a_H	b_H	c_H
$2.53 \cdot 10^{-5}$	$5.49 \cdot 10^{-3}$	$1.14 \cdot 10^{-3}$

Corresponding to the dry mapping function, the wet NMF is also based on the Marini continued fraction form. A height correction is not necessary here and the coefficients a, b, and c can be interpolated linearly from Table 3.3.

Table 3.3: Coefficients of the wet NMF as a function of the site latitude φ according to Boehm [2004]

	$\varphi = 15°$	$\varphi = 30°$	$\varphi = 45°$	$\varphi = 60°$	$\varphi = 75°$
a	$5.8021897 \cdot 10^{-4}$	$5.6794847 \cdot 10^{-4}$	$5.8118019 \cdot 10^{-4}$	$5.9727542 \cdot 10^{-4}$	$6.1641693 \cdot 10^{-4}$
b	$1.4275268 \cdot 10^{-3}$	$1.5138625 \cdot 10^{-3}$	$1.4572752 \cdot 10^{-3}$	$1.5007428 \cdot 10^{-3}$	$1.7599082 \cdot 10^{-3}$
c	$4.3472961 \cdot 10^{-2}$	$4.6729510 \cdot 10^{-2}$	$4.3908931 \cdot 10^{-2}$	$4.4626982 \cdot 10^{-2}$	$5.4736038 \cdot 10^{-2}$

3.1.2 Vienna Mapping Functions

Instead of using zenith delays calculated according to the Saastamoinen model as in the case of the Niell Mapping Functions introduced in 3.1.1, the VMF described in Boehm and Schuh [2003] refer to zenith delays resulting from direct ray-tracing through Numerical Weather Models (NWMs). VMF are provided by Vienna University of Technology on

http://ggosatm.hg.tuwien.ac.at/DELAY/GRID/VMFG (08.07.2014)

This web page also provides the dry and wet coefficients a_{dry} and a_{wet}. The structure of the downloaded grid files containing these values is presented below. Then, the computation of the b and c coefficients is given. Moreover, necessary temporal and spatial interpolation steps as well as the height correction are explained. The height correction is necessary in the case of the computation of the dry VMF and has to be applied to the delays. Finally the computation of the already used coefficients a and that of the delays given in the grids is described. As the VMF was used for the first time at the GIK within this work, detailed information on its computation are given. The appendix summarizes the main steps and settings within the VMF processing in Bernese.

The structure of the grid files containing the VMF coefficients a_{dry} and a_{wet} as well as the dry and wet zenith delays deduced from ray-tracing through numerical weather models is shown in Figure 3.2. In the first two columns, the grid points are defined by their respective latitudes and longitudes. The resolution in latitude is 2° and that in longitude is 2.5°. The next two columns provide the dry coefficients a_{dry} and the wet coefficients a_{wet} for the Marini continued fraction form from (3.4). Finally, in the last two columns, values for the zenith dry and zenith

```
! Version:          1.0
! Source:           J. Boehm, TU Vienna
! Data_types:       VMF1 (lat lon ah aw zhd zwd)
! Epoch:            2005 01 01 00 00  0.0
! Scale_factor:     1.e+00
! Range/resolution: -90 90 0 360 2 2.5
! Comment:          www.hg.tuwien.ac.at/~ecmwf1
90.0    0.0 0.00115751  0.00051480  2.3093  0.0102
90.0    2.5 0.00115751  0.00051480  2.3093  0.0102
90.0    5.0 0.00115751  0.00051480  2.3093  0.0102
90.0    7.5 0.00115751  0.00051480  2.3093  0.0102
90.0   10.0 0.00115751  0.00051480  2.3093  0.0102
90.0   12.5 0.00115751  0.00051480  2.3093  0.0102
90.0   15.0 0.00115751  0.00051480  2.3093  0.0102
  .      .      .          .          .       .
  .      .      .          .          .       .
  .      .      .          .          .       .
90.0  342.5 0.00115751  0.00051480  2.3093  0.0102
90.0  345.0 0.00115751  0.00051480  2.3093  0.0102
90.0  347.5 0.00115751  0.00051480  2.3093  0.0102
90.0  350.0 0.00115751  0.00051480  2.3093  0.0102
90.0  352.5 0.00115751  0.00051480  2.3093  0.0102
90.0  355.0 0.00115751  0.00051480  2.3093  0.0102
90.0  357.5 0.00115751  0.00051480  2.3093  0.0102
88.0    0.0 0.00116061  0.00059625  2.2962  0.0168
88.0    2.5 0.00116063  0.00059629  2.2956  0.0169
88.0    5.0 0.00116066  0.00059703  2.2951  0.0170
88.0    7.5 0.00116069  0.00059730  2.2947  0.0170
88.0   10.0 0.00116071  0.00059714  2.2939  0.0170
88.0   12.5 0.00116073  0.00059723  2.2937  0.0170
88.0   15.0 0.00116076  0.00059711  2.2933  0.0170
  .      .      .          .          .       .
  .      .      .          .          .       .
```

Figure 3.2: Gridded VMF coefficients and delays

wet delays at the grid points are given. While the coefficients a_{dry} refer to zero height, the modeled delay values $\Delta^{zenith}_{dry,\,model}$ and $\Delta^{zenith}_{wet,\,model}$ are related to the ellipsoidal heights of the respective grid points provided on

http://ggosatm.hg.tuwien.ac.at/DELAY/GRID/orography_ell (08.07.2014)

Consequently, height corrections, as described below, have to be applied to the delays and to the dry VMF coefficients interpolated spatially and temporally to the considered observing site. Each grid file covers six hours and is called *VMFG_yyyymmdd.Hhh* by convention, where

yyyy	year
mm	month
dd	day
hh	00, 06, 12, or 18 for each of the four six-hours files

Five of these six-hours files are merged at a time to obtain one single file *VMF_yyyyDOY.GRD* for a specific *DOY*. That means four files of the day itself are merged together with the first file ($hh = 00$) of the following day. It is not necessary to remove the headers before the file concatenation.

In case of the dry VMF, $b_{dry} = 0.0029$ is kept fixed according to Boehm et al. [2006] and c_{dry} results from

$$c_{dry} = c_0 + \left[\left(\cos\left(\frac{DOY - 28}{365} \cdot 2\pi + \Psi\right) + 1\right) \cdot \frac{c_{11}}{2} + c_{10}\right] \cdot (1 - \cos\varphi) \tag{3.8}$$

Table 3.4: Coefficients for the determination of c_{dry} according to **?**

	Northern hemisphere	Southern hemisphere
c_0	0.062	0.062
c_{10}	0.001	0.002
c_{11}	0.005	0.007
Ψ	0	π

where the coefficients c_0, c_{10}, and c_{11} as well as Ψ are given in Table 3.4.

The values of a_{dry} are taken from the grid files and interpolated spatially and temporally as described below. A height correction is applied as in the case of the NMF because the gridded VMF coefficients refer to a height of zero as indicated in Boehm [2010]. Here, the coefficients a_H, b_H, and c_H from (3.7) equal those of the NMF height correction. Based on the coefficients a_{dry}, b_{dry}, and c_{dry}, the dry component of the VMF can then be computed using the Marini continued fraction form in (3.4).

In order to determine the wet VMF, the values of b_{wet} and c_{wet} correspond to the values of the NMF at a latitude of $\varphi = 45°$

$$b_{wet} = 0.00146$$
$$c_{wet} = 0.04391$$

(3.9)

and a_{wet} is again taken from the grid file and interpolated spatially and temporally. As in the case of the dry VMF, the wet mapping function results from evaluating (3.4) with the respective coefficients.
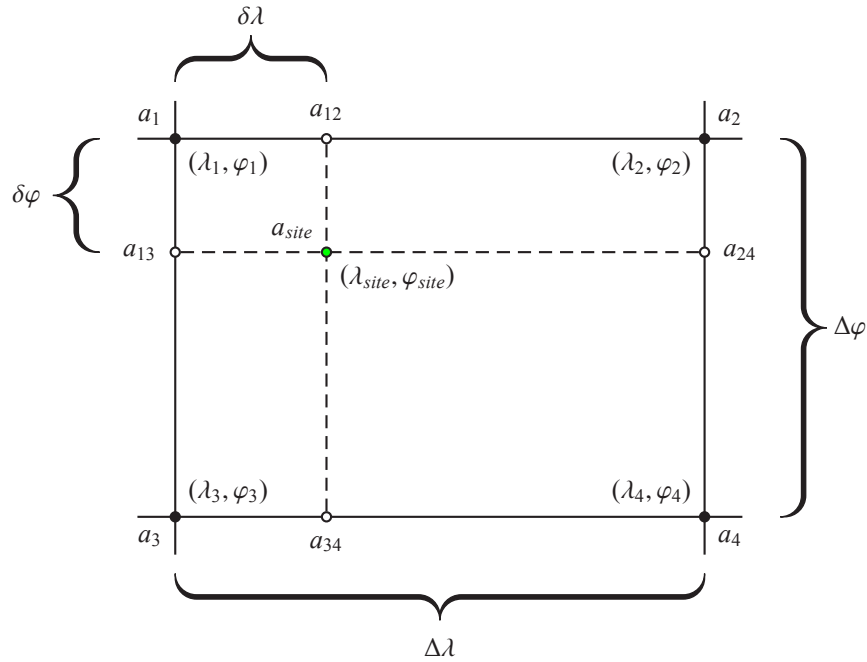
Figure 3.3: Bilinear interpolation on the grid of the VMF coefficients

The coefficients a_{dry} and a_{wet} read from the VMF grid files are interpolated bilinearly in space as illustrated in Figure 3.3

$$a_{13} = \frac{\delta\varphi \cdot (a_3 - a_1)}{\Delta\varphi} + a_1$$
$$a_{24} = \frac{\delta\varphi \cdot (a_4 - a_2)}{\Delta\varphi} + a_2$$
$$a_{site} = \frac{(\Delta\lambda - \delta\lambda) \cdot (a_{13} - a_{24})}{\Delta\lambda} + a_{13}$$

(3.10)

and interpolated linearly in time

$$a_{interpolated} = a_{site} + \frac{t - t_1}{t_2 - t_1} \cdot (a_{site,\,t_1} - a_{site,\,t_2}) \tag{3.11}$$

Here t stands for the interpolation time, whereas t_1 and t_2 represent epochs of 30 s at which GNSS data are available.

Within the module VMF1ELL.f90 of Bernese, the modeled delays $\Delta_{dry,\,model}^{zenith}$ and $\Delta_{wet,\,model}^{zenith}$ are interpolated bilinearly within the grid analogously to the coefficients a and corrected for the differences between the ellipsoidal heights and the actual height of the considered observing site. Figure 3.4 illustrates the height definition with respect to the ellipsoid and geoid. The choice of the height system depends on the application. If during the whole project only ellipsoidal coordinates are considered, no height correction is needed. The ellipsoidal heights observed by GNSS are geometric quantities depending on the chosen reference ellipsoid WGS84 (World Geodetic System 1984). However, if a fusion with observations referring to non-geometric heights H_{ngeo} is aimed, i.e. if the observations refer to the gravity field, the height correction becomes essential. Such heights may refer to the geoid (orthometric heights) or to a quasi-geoid (normal heights). Torge [2001] defines orthometric heights as the distance along the plumb line between the surface point and the geoid. Unfortunately, these heights require introducing a model of the density distribution of the topographic masses. This might cause uncertainties in the determined heights. To overcome this weakness of orthometric heights, normal heights are used in the current DHHN92 (Deutsches Haupthöhennetz 1992) in Germany. Their reference surface is the so-called quasi-geoid which agrees with the geoid within the mm to cm order at low altitudes. Within mountainous regions, deviations of up to one meter are reached.
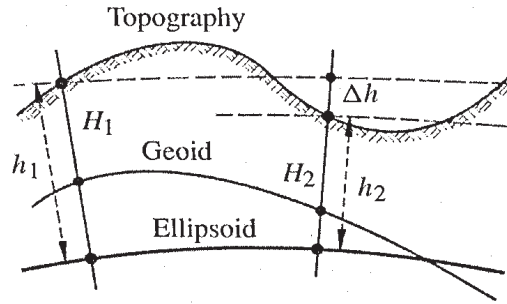
Figure 3.4: Ellipsoidal and orthometric heights h and H according to Seeber [2003]

Both the interpolation in space and that in time are implemented within the Bernese module D_GRID.f90. Although the delays are determined by means of ray-tracing, the height correction of the dry delays contained in the grid files appears in the form

$$\Delta_{dry,\,approx}^{zenith} = 0.0022768 \cdot \frac{p_0}{1 - 0.00266 \cdot \cos(2\varphi) - 0.28 \cdot 10^{-6} \cdot H} \tag{3.12}$$

from Boehm et al. [2006] and referring to Saastamoinen [1973]. In this context Berg [1948] computes p_0 by

$$p_0 = 1.01325 \cdot (1 - 0.0000226 \cdot H)^{5.225} \tag{3.13}$$

and a value for the dry delay corrected for height Δ_{dry}^{zenith} is obtained from:

$$\Delta_{dry}^{zenith} = \Delta_{dry,\,model}^{zenith} \cdot \frac{1 - 2.26 \cdot 10^{-5} \cdot H_{site,\,ell}}{1 - 2.26 \cdot 10^{-5} \cdot H_{site,\,ngeo}} \cdot \frac{1 - 0.00266 \cdot \cos(2\varphi) - 0.28 \cdot 10^{-6} \cdot H_{site,\,ngeo}}{1 - 0.00266 \cdot \cos(2\varphi) - 0.28 \cdot 10^{-6} \cdot H_{site,\,ell}} \tag{3.14}$$

For the wet delay provided by the VMF grids, no comparable approach exists for the conversion of the delays referring to ellipsoidal heights. Therefore an empirical model

$$\Delta_{wet}^{zenith} = \Delta_{wet,\,model}^{zenith} \cdot e^{-\left(H_{site,\,ell} - H_{site,\,ngeo}\right)/2000} \tag{3.15}$$

has been developed assuming an exponential decay. According to Kouba [2008], the decay coefficient was deduced from the averaged differences between the zenith wet delay at an observing site located about 1100 m above the mean grid height and the values of the zenith wet delay at the mean grid heights. Alternatively to the gridded VMF, site-dependent VMF data are available for selected sites of the International GNSS Service (IGS). Although the gridded VMF coefficients are interpolated within a grid of $2° \times 2.5°$, their comparison with the site-dependent VMF data in Kouba [2008] shows a very good agreement. The coefficients a_{dry} and a_{wet} from the gridded VMF and the site-dependent correspond to each other at an RMS level of 1×10^{-6} and 2×10^{-5}, respectively.

The coefficients a as well as the delays $\Delta_{dry, model}^{zenith}$ and $\Delta_{wet, model}^{zenith}$ provided in the grids result from direct ray-tracings through NWMs. Following Nafisi et al. [2012], the idea behind this method is the description of the total delay along the signal path through the atmosphere. Thereby, no intermediate steps as in the case of previous mapping functions (e.g., isobaric mapping function) are necessary. For this purpose, the neutrosphere is subdivided into k height levels, where $k \approx 1000$. As described in Boehm and Schuh [2003], the necessary input parameters are an initial elevation angle ε_0 as well as values for the height and the corresponding temperatures and partial pressures of water vapor originating from the NWM. The values of the height, the temperature and the water vapor pressure are provided on 15 different pressure levels extending from 1000 hPa to 10 hPa, and they have to be interpolated spatially. Different horizontal interpolation techniques and an optimum number of height levels regarding the accuracy as well as the computing time are discussed in Nafisi et al. [2012]. Figure 3.5 shows the distinct height levels deduced from the ECMWF (European Center for Medium-Range Weather Forecasts) pressure data and their respective refractivities.
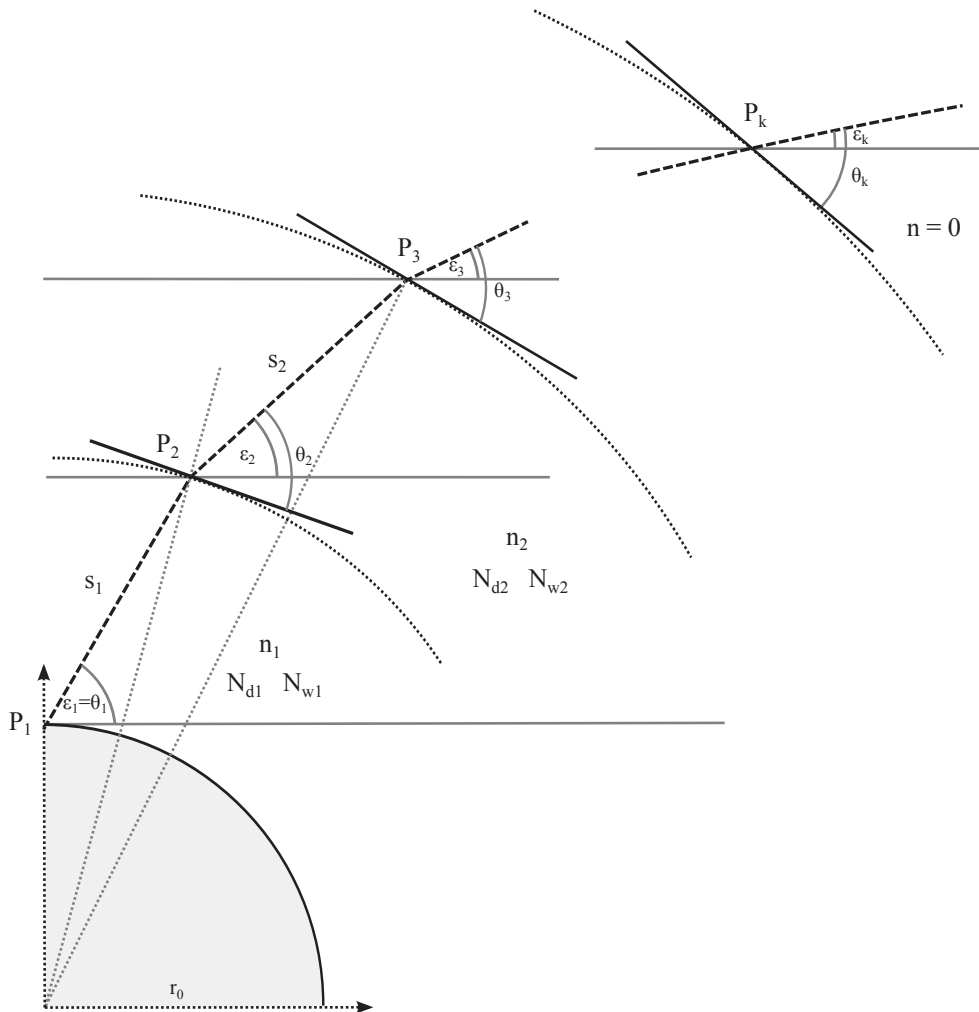
Figure 3.5: Geometry of a 1D ray-tracing method in local topocentric coordinates according to Boehm and Schuh [2004]

Two different determination methods exist for the coefficients a_{dry} and a_{wet}. The rigorous approach computes the mapping functions as well as the outgoing elevation angles for ten different initial elevation angles, whereas the fast approach only uses one single initial elevation angle $\varepsilon_0 = 3.3°$. Hence, in the fast version, one value at a time is obtained for the dry and wet mapping function and for the vacuum elevation angle. This vacuum elevation angle has to be imagined as the elevation angle at the boundary of the outermost neutrospheric layer, denoted ε_k in Figure 3.5.

In this figure, the point P_1 represents the position of the receiver and P_k identifies the piercing point of the ray with the upper limit of the neutrosphere. The x-axis and y-axis of the Cartesian coordinate system are considered to be parallel to the zenith direction and to the horizon of the site. The distances between two consecutive points on the ray path are denoted with s_i. The elevation angles ε_i are measured with respect to a horizontal plane. In contrast, the angles θ_i are computed with respect to the tangents to the layers characterized by their dry and wet refractivities N_{di} and N_{wi} or their refractive index n_i, respectively. Mathematically, the ray-tracing system is based on the Eikonal Equation derived from Maxwell's Equations. The aforementioned values of b_{dry}, c_{dry}, b_{wet}, and c_{wet} are used to deduce a_{dry} and a_{wet} by inversion of (3.4). In contrast to this comparatively easy fast determination, the ten times slower rigorous approach estimates the coefficients within a least-squares adjustment. In Bernese, grid files resulting from the fast method are used.

In case of the VMF, a horizontal symmetry is assumed in the ray-tracing. According to Nafisi et al. [2012], there are other, more realistic approaches considering horizontal asymmetries in 2D or 3D. However, the two-dimensional hypothesis does not account for rays leaving the constant azimuth plane and the three-dimensional hypothesis causes computational problems.

As a mapping by means of the VMF has been performed for the first time at GIK within this work, additional information on the NMF and VMF processing steps within Bernese are given in the appendix.

3.2 Modeling the neutrospheric delay within GNSS data processing

Generally, the modeling of the neutrospheric path delay between a receiver and a satellite is performed within the Bernese software by means of

$$\Delta^{slant}(t,A,\varepsilon) = \Delta^{slant}_{a\,priori}(\varepsilon) + \Delta^U(t) \cdot mf_{wet}(\varepsilon) + \Delta^N(t) \cdot \frac{\partial mf_{wet}}{\partial \varepsilon} \cdot \cos A + \Delta^E(t) \cdot \frac{\partial mf_{wet}}{\partial \varepsilon} \cdot \sin A \qquad (3.16)$$

from Dach et al. [2007] with

$\Delta^{slant}(t,A,\varepsilon)$	neutrospheric path delay between the receiver and the satellite
t	time
A	azimuth observed from the receiver to the satellite
ε	elevation of the satellite when observed by the receiver
$\Delta^{slant}_{a\,priori} = \Delta^{zenith}_{a\,priori} \cdot mf_{dry}$	slant neutrospheric path delay from the chosen a priori model
$\Delta^U(t)$	time-dependent site-specific neutrosphere parameters (SSNP) added to the a priori model
$mf_{dry}(\varepsilon)$ and $mf_{wet}(\varepsilon)$	dry and wet mapping functions
$\Delta^N(t)$ and $\Delta^E(t)$	time-dependent horizontal gradients in Northing and Easting

The a priori model can be chosen by the user. In case of the NMF, either NIELL or DRY_NIELL are possible. Both are determined by means of the formula of Saastamoinen, in which the second summand The a priori model can be chosen by the user. In case of the NMF, either NIELL or DRY_NIELL are possible. Both are determined by means of the formula of Saastamoinen, in which the second summand

$$p + \left(\frac{1255}{T} + 0.05 \right) \cdot e \qquad (3.17)$$

is neglected in the case of DRY_NIELL. If the option VMF or DRY_VMF is chosen, the a priori zenith path delays are provided by the grid files.

When estimating the SSNP for a comparison with the partial wet delays from InSAR, the option DRY_NIELL is very useful, because Dach et al. [2007] assume that the estimated SSNP represent the wet delay, whereas the a priori model gives the dry delay. Additional to the SSNP and horizontal gradients tilting the local zenith direction by an angle β as illustrated in Figure 3.6, residuals are computed after the parameter estimation. Figure 3.7 summarizes all components of the modeled path delay.
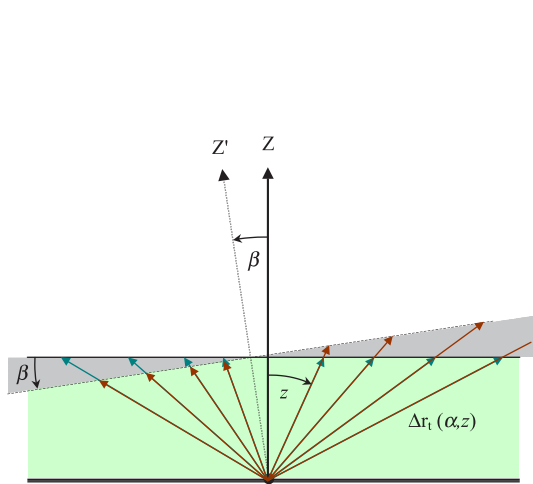
Figure 3.6: Tilting of the neutrospheric zenith by an angle β from Dach et al. [2007]

Figure 3.7: Components of the total zenith path delay

The a priori neutrospheric model, the SSNP, and the horizontal gradients are written to a Bernese troposphere file with the file extension *.TRP. An example is given in Figure 3.8. The header summarizes the selected options for the a priori model, mapping function, gradient model, minimum elevation, and the temporal sampling interval. The first eight columns represent the name of the considered observing site, a flag marking the estimated coordinates depending on the 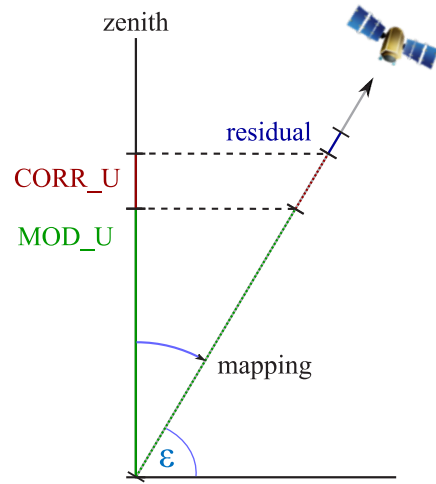modifying program, and the respective date and time for which the parameters have been computed. The following eight columns give values of the a priori model $\Delta_{a\ priori}^{zenith} = MOD\_U$ and the site-specific neutrosphere parameters $\Delta^U = CORR\_U$ in zenith direction, as well as horizontal gradients $\Delta^N = CORR\_N$ and $\Delta^E = CORR\_E$. All values are given in meter. The sum of MOD_U and CORR_U is written to the column TOTAL_U. Standard deviations SIGMA_U, SIGMA_N, and SIGMA_E for the respective values of the a priori model, the SSNP, and the horizontal gradients can also be found in the file. Generally one might assume a height accuracy of about $2-3$ mm within static GPS. Following the rule of thumb of Niell [1991] and its refinements in Boehm et al. [2006], the error in site height corresponds to about one third or one fifth of the delay error at the lowest elevation angle included in the analysis. A short estimation based on a simple $1/\sin\varepsilon$ mapping function is used to check the plausibility of the standard deviations given by Bernese. If an error of $dH = 2$ mm $- 3$ mm in

```
stacking_SSNP_2013_10_24                                      24-OCT-13 13:53
---------------------------------------------------------------------------------------------------------
A PRIORI MODEL:  -15   MAPPING FUNCTION:   4   GRADIENT MODEL:   4   MIN. ELEVATION:   3   TABULAR INTERVAL:  3600 / 86400

STATION NAME    FLG   YYYY MM DD HH MM SS   YYYY MM DD HH MM SS   MOD_U   CORR_U  SIGMA_U TOTAL_U  CORR_N   SIGMA_N   CORR_E  SIGMA_E

0384            A     2005 01 01 00 00 00                         2.2158  0.11691 0.00099 2.33269 -0.00038 0.00004  0.00033 0.00004
0384            A     2005 01 01 01 00 00                         2.2158  0.09669 0.00061 2.31246 -0.00039 0.00004  0.00033 0.00004
0384            A     2005 01 01 02 00 00                         2.2158  0.10537 0.00041 2.32114 -0.00040 0.00004  0.00033 0.00004
0384            A     2005 01 01 03 00 00                         2.2158  0.10203 0.00059 2.31781 -0.00040 0.00003  0.00032 0.00003
0384            A     2005 01 01 04 00 00                         2.2158  0.10847 0.00047 2.32424 -0.00041 0.00003  0.00032 0.00003
0384            A     2005 01 01 05 00 00                         2.2158  0.10689 0.00042 2.32266 -0.00042 0.00003  0.00031 0.00003
0384            A     2005 01 01 06 00 00                         2.2158  0.11565 0.00059 2.33143 -0.00042 0.00003  0.00031 0.00003
0384            A     2005 01 01 07 00 00                         2.2158  0.10881 0.00048 2.32458 -0.00043 0.00003  0.00031 0.00003
0384            A     2005 01 01 08 00 00                         2.2158  0.09947 0.00039 2.31525 -0.00044 0.00003  0.00030 0.00002
0384            A     2005 01 01 09 00 00                         2.2158  0.10060 0.00046 2.31638 -0.00044 0.00002  0.00030 0.00002
```

Figure 3.8: Header and first lines of a Bernese *.TRP-file

site height is assumed and if the lowest elevation angle included in the analysis corresponds to $3°$, then the error in slant delay at this ε equals

$$d\Delta^{slant} = 5 \cdot dH \approx 10 \text{ mm} - 15 \text{ mm} \tag{3.18}$$

and the mapping function yields an error in the zenith delay of

$$d\Delta^{zenith} = \sin\varepsilon \cdot d\Delta^{slant} = 0.5 \text{ mm} - 0.8 \text{ mm} \tag{3.19}$$

This agrees well with the standard deviations of the SSNP resulting from Bernese. The a priori model is introduced as exact into the computations of the software and therefore does not contribute to the standard deviation given in the troposphere files. The SSNP values represent corrections to the a priori model. Therefore, the precondition of an error-free a priori model is legitimate even though this a priori model does not perfectly represent the actual total delay.

The described troposphere files originate from a sequential least squares adjustment, splitting the complete least squares adjustment over all considered days into different parts. An additional call of the panel ADDNEQ combines the daily troposphere files resulting from the run of the BPE to one large file containing the troposphere parameters for all considered days. During this step, offsets appearing at the intersection of different days are reduced. This also involves an improvement of the accuracies of the values corresponding to the first or to the last hours of a day. Initially, their standard deviations are larger than those of the values at midday because less data are available around them when splitting the solution of the normal equations into day-wise computations. Thus, the changes of the values at midday that are caused by the normal equation stacking within ADDNEQ should be smaller than those early or late in the night. This implies that the normal equation stacking might be omitted in further processings aiming at a comparison of GNSS and InSAR observations because SAR data are acquired at 9:51 UTC. However, detailed analyses of the true effects of the normal equation (NEQ) stacking on the troposphere parameters at different times of the day should be carried out before declaring the stacking as useless.

3.3 Precise point positioning and selection of the representative GNSS sites

Differential positioning and absolute positioning are the two possible strategies used to determine positions from the observed GNSS signals. According to Hofmann-Wellenhof et al. [2001], absolute point positioning methods can be subdivided into point positioning with code ranges, carrier phases and Doppler radar. Precise point positioning uses accurate orbits and satellite clock data provided by the IGS to account for orbit and clock errors. Moreover, the ionosphere-free combination of code pseudoranges and carrier phases introduced in (2.9) is computed from dual- reps. multi-frequency observations in order to reduce ionospheric delays. Contrary to differential positioning methods with small baselines, where neutrospheric delays are mostly eliminated, the entire impact of the neutrosphere has to be modeled in the case of PPP measurements.

The observation equation for point positioning using carrier phases can be written as

$$\Phi_R^S(t) = \frac{f^S}{c} \cdot \delta_R^S(t) + N_R^S + f^S \cdot \delta_R(t) - f^S \cdot \delta^S(t) \tag{3.20}$$

with

$\Phi_R^S(t)$	carrier phase
f^S	frequency of the signal
c	speed of light in vacuum
$\delta_R^S(t)$	geometric distance from the receiver's antenna R to the satellite antenna S
N_R^S	integer phase ambiguity
$\delta_R(t)$	receiver clock error
$\delta^S(t)$	satellite clock error

and

$$\delta_R^S(t) = \sqrt{(X^S - X_R)^2 + (Y^S - Y_R)^2 + (Z^S - Z_R)^2} \tag{3.21}$$

where

X_S, Y_S, Z_S geocentric Cartesian coordinates of the satellite antenna

X_R, Y_R, Z_R geocentric Cartesian coordinates of the receiver's antenna

Equation 3.20 yields, when assuming the satellite clock error $\delta^S(t)$ given by the IGS, considering neutrospheric delays Δ^{slant} as well as noise n, and applying the ionosphere-free linear combination L_3, the PPP observation equation

$$\Phi_R^S(t) + f^S \cdot \delta^S(t) = \frac{f^S}{c} \cdot \delta_R^S(t) + R_R^S + f^S \cdot \delta_R(t) + \frac{f^S}{c} \cdot \Delta^{slant} + n \tag{3.22}$$

where R_R^S represents the floating-point number ambiguities of L_3.

Ten GNSS sites from the GNSS Upper Rhine Graben Network have been chosen for the following comparison of the effects of NMF and VMF. Five of them belong to the SAtellite POsitioning Service (Satellitepositionierungsdienst SA*POS*®) of the German Federal Land Rheinland-Pfalz, the remaining sites are part of SA*POS*® Baden-Württemberg. The main focus within the selection lies on including both particularly high and particularly low sites into the analysis. Moreover, the availability of observations at low elevations ($\varepsilon \leq 5°$) has been checked at these sites by means of the toolkit TEQC (translation, editing, and quality check) often also used for the pre-processing of GNSS data. The selected observing sites' number of observations at low elevation angles are shown in Figure 3.9 and Figure 3.10. Figure 3.11 and Table 3.5 give an overview of the location and of the height of the selected GNSS sites.

Besides the total number of measurements at low elevation angles, attention has also been paid to a constant number of observations (see Figure 3.10). An observing site of a permanent, comparable, rather small number of observations at low elevation angles is preferred over a site as that in Figure 3.10, at which the number of observations changes clearly from day to day. The analyses carried out at the beginning of the thesis are performed by TEQC and based on the first ten days of January 2005 and the first ten days of July 2005 in order to verify data of winter and summer days.

Table 3.5: Selected GURN observing sites

Site acronym	Site name	Longitude [°]	Latitude [°]	Height [m]
0387	Heidelberg	8.7	49.4	169
0388	Iffezheim	8.1	48.8	185
0391	Geislingen	9.8	48.6	736
0396	Biberach	8.5	48.3	599
0399	Villingen-Schwenningen	9.8	48.1	793
0512	Koblenz	7.6	50.4	184
0514	Simmern	7.5	50.0	419
0518	Bingen	7.9	50.0	263
0520	Ludwigshafen	8.5	49.5	158
0521	Landau	8.1	49.2	208

For the final comparison of GNSS and InSAR data, only the sites 0387, 0388, 0520, and 0521 located within the considered SAR frame are used. In order to be sure that no wet delay components are contained in the a priori model, the respective options in Bernese have been set to DRY_NIELL and DRY_VMF.
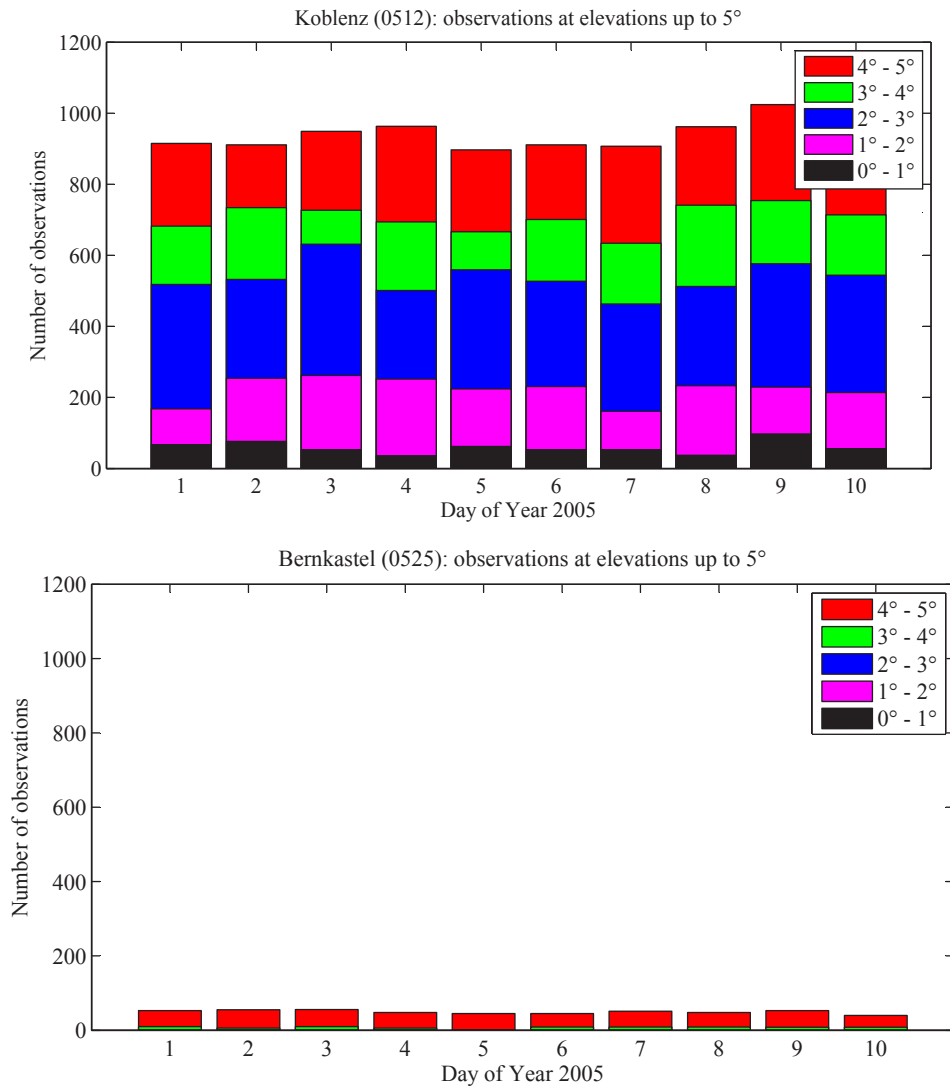
Figure 3.9: Comparison of two sites with many and very few observations at low elevation angles; top: Koblenz; bottom: Bernkastel
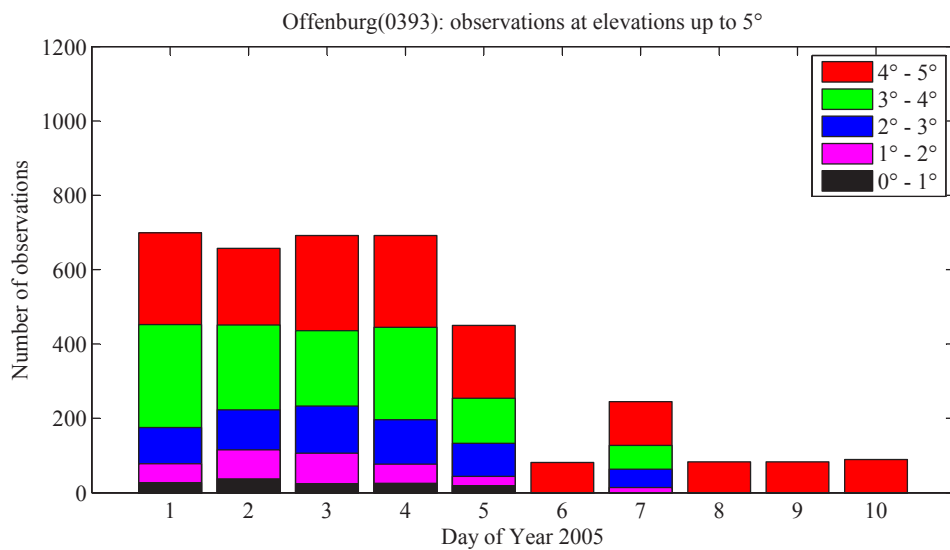
Figure 3.10: Number of observations at the observing site Offenburg
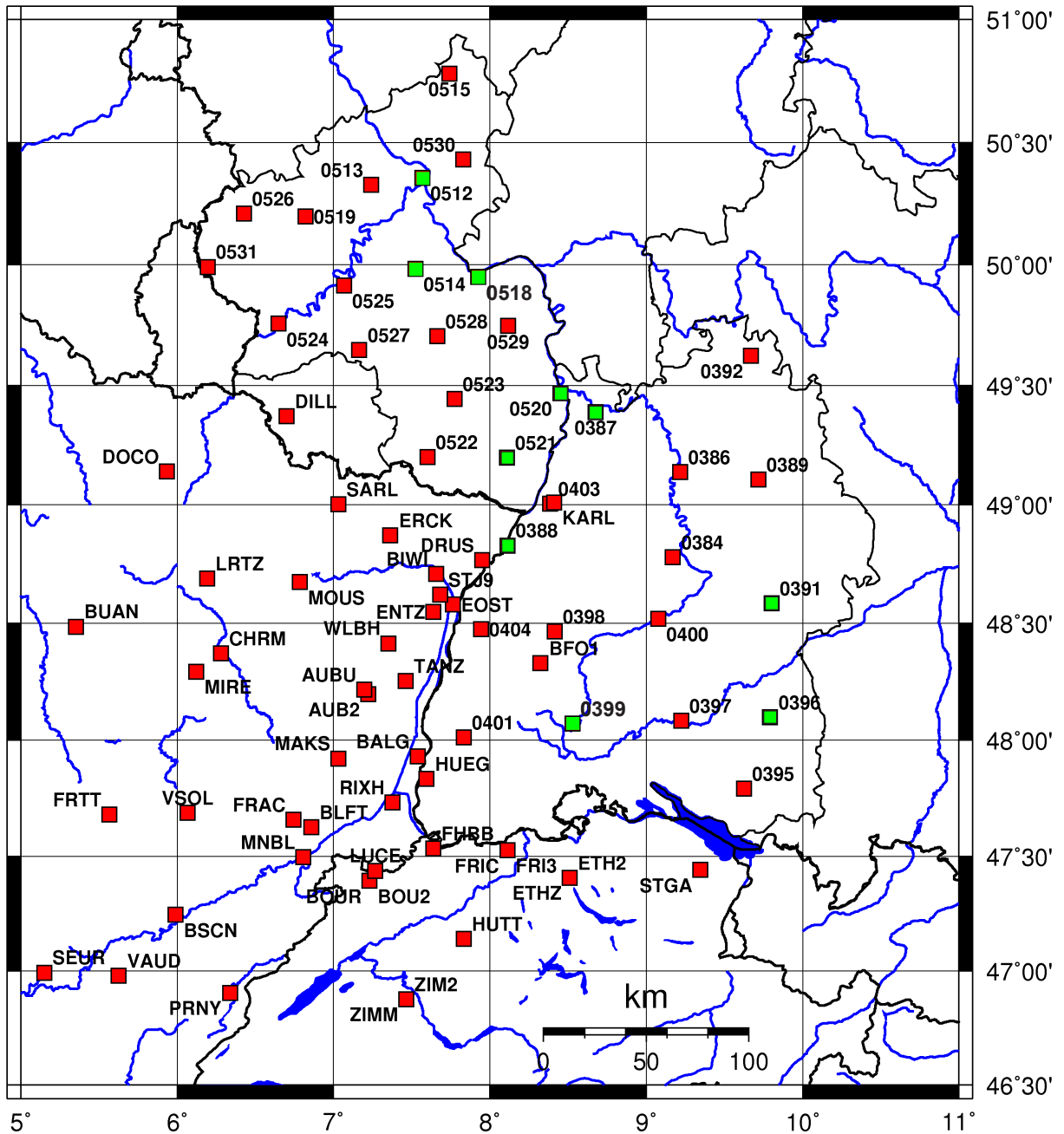
Figure 3.11: Selected GURN observing sites are shown in green (figure provided by Andreas Knöpfler, see also Knöpfler et al. [2010] for basic information on GURN); The four sites used for the final comparison with InSAR observations are Heidelberg (0387), Iffezheim (0388), Ludwigshafen (0520), and Landau (0521).

3.4 Comparison of the effects of NMF and VMF on GNSS estimates

While the NMF is determined purely empirically, VMF values are based on real weather data and may represent short-scale temporal variations more accurately. Therefore, the two mapping functions introduced in section 3.1 have been compared with respect to different criteria over the whole year 2005. The resulting heights, SSNP, and horizontal gradients estimated using the PPP method with both Niell and Vienna mapping functions are analyzed in the following subsections.

3.4.1 Height component

While the clock estimation is independent of elevation, Boehm and Schuh [2013] illustrate the elevation-dependency of the neutrospheric delays and the height components as in Figure 3.12.

Figure 3.12: Elevation-dependency of the neutrospheric delays Δ and the height components H according to Boehm and Schuh [2013]

The partial derivative $\partial \Delta^{slant} / \partial H = \sin \varepsilon$ for the estimation of the height component is easy to determine within the rectangular triangles spanned by the blue arrows. On the contrary, the derivative with respect to the zenith delay $\partial \Delta_{slant} / \partial \Delta_{zenith}$ is close to $\sin \varepsilon$, but its exact value is difficult to determine. However, an erroneous mapping fun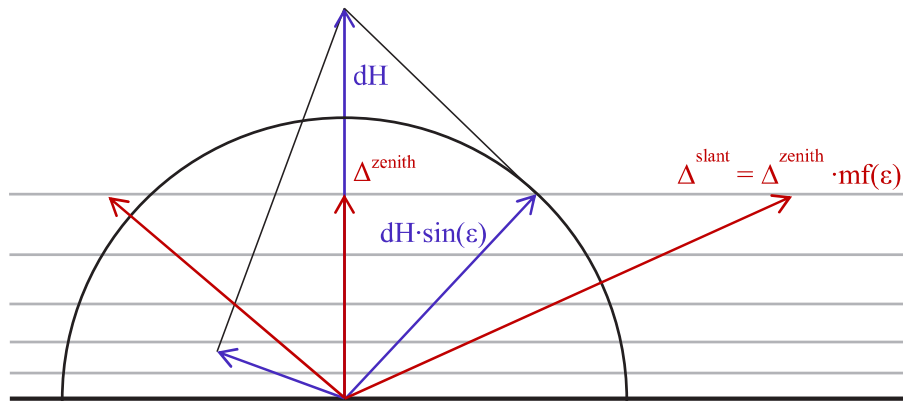ction results in a wrong zenith delay because the zenith neutrospheric delay Δ^{zenith} stays constant and equation (3.2) still holds. As a result, in case of erroneous mapping functions, the site height is also estimated in a wrong way. Table 3.6 illustrates this relation between the mapping function, the zenith delay, and the site height.

Table 3.6: Relation between mapping function, zenith delay, and site height

Mapping function		Zenith delay		Site height
too large	$\rightleftharpoons$	too small	$\rightleftharpoons$	too large
too small	$\rightleftharpoons$	too large	$\rightleftharpoons$	too small

For this reason, a comparison of the resulting heights is of great interest when aiming at modeling neutrospheric delays. The largest difference in height $H_{NMF} - H_{VMF}$ occurring within the year 2005 at one of the selected observing sites equals about 16 mm (on 11-12-2005 at GPS site 0512, i.e. Koblenz). The mean height differences $H_{NMF} - H_{VMF}$ for the ten selected observing sites averaged over the whole year take values of up to 1.3 mm (at the site 0512, i.e. Koblenz).

As illustrated in Table 3.7, the standard deviations of those mean heights deduced from processings with the VMF are smaller than those derived from processings with NMF, which might be due to a slightly better model of the neutrospheric delays in case of the VMF. Figure 3.13 exemplary shows the differences in height observed at the

Table 3.7: Mean heights in m and their standard deviations in mm with respect to applied MF

Acronym	Site name	Mean H_{NMF}	Mean H_{VMF}	Std H_{NMF}	Std H_{VMF}
0387	Heidelberg	168.818	168.817	6	5
0388	Iffezheim	185.433	185.432	6	6
0391	Geislingen	736.265	736.265	6	5
0396	Biberach	599.285	599.284	5	5
0399	Villingen-Schwenningen	792.874	792.873	6	5
0512	Koblenz	183.989	183.987	7	6
0514	Simmern	419.419	419.418	6	5
0518	Bingen	262.802	262.801	7	6
0520	Ludwigshafen	158.310	158.309	6	5
0521	Landau	208.028	208.028	6	5

site 0387 (Heidelberg) over the year 2005. This particular site has been selected because of the availability of a complete dataset without gaps within 2005.
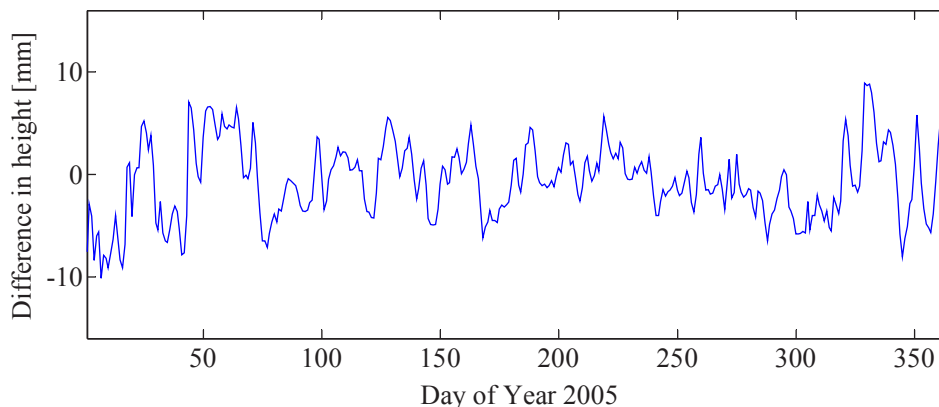
Figure 3.13: Differences in height $H_{NMF} - H_{VMF}$ observed at the observing site 0387 (Heidelberg)

Besides the height, longitude and latitude complete the determined position. However, these two latter coordinates remain unchanged for NMF and VMF. The maximum differences that have occurred within 2005 correspond to a change in distance of less than 0.02 mm. As a consequence, there is no significant change in the height determination when applying the VMF. Also, there is no impact if the user decides to use a conventional NMF processing in order to determine heights.

3.4.2 Site-specific neutrospheric parameters and horizontal gradients

In addition to the a priori model for the neutrospheric delay, SSNP and horizontal gradients are estimated within an hourly sampling and compared with respect to the underlying mapping function.

When comparing the SSNP values deduced by selecting NMF and VMF during the processing, it can be noticed that the mean SSNP over two selected short periods of time (ten days in January and in July 2005) are larger in the case of an NMF processing than in the case of a VMF processing. As seen in Table 3.8, this statement is valid throughout the whole year of 2005. These particular periods of time have been opposed because they typically represent dry winters and humid summers within the GURN region. Moreover, the two periods of time try to oppose the abilities of both mapping functions to model extreme or short-time weather occurrences. The higher values of the SSNP observed during the ten days in July can be explained by the typical annual climate trend within the GURN region. This climate is dominated by dry winters and comparatively wet summers and its annual trend is superposed by quite high short-scale temporal variations that can be seen in Figure 3.14.
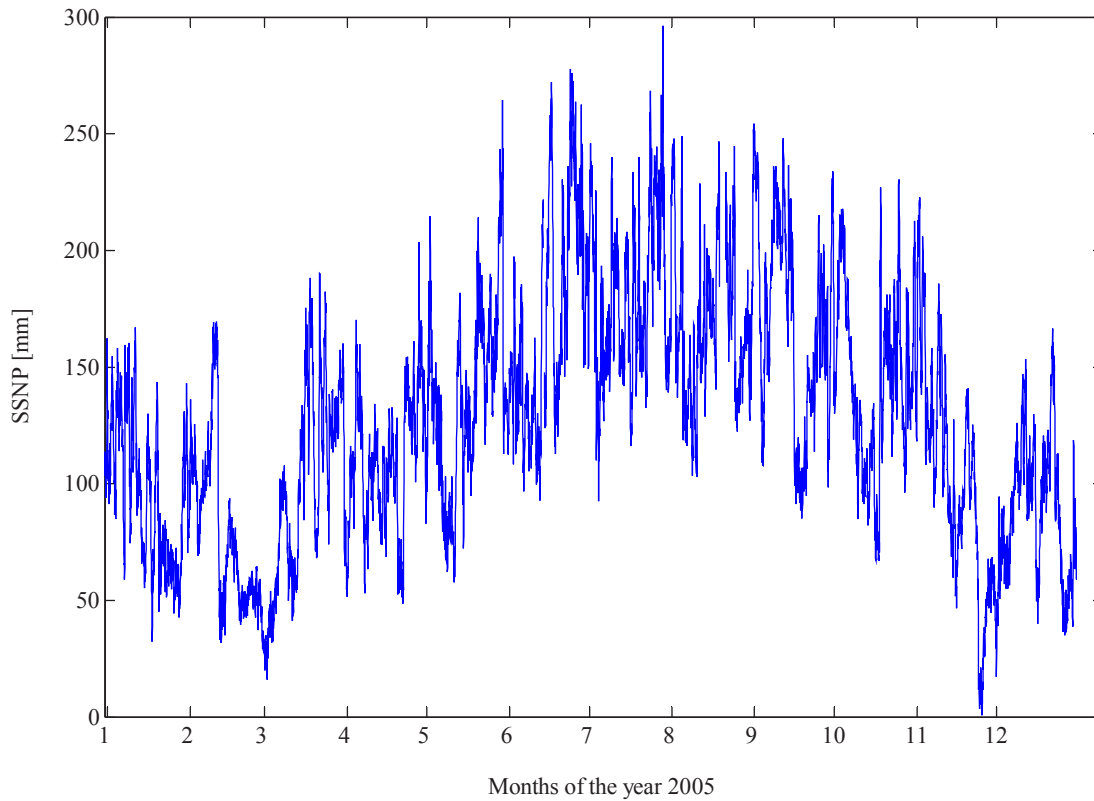
Figure 3.14: Iffezheim (0388): Annual trend of the SSNP from NMF after NEQ stacking

Due to the smaller values of the SSNP in case of the VMF, it can be assumed that the a priori model deduced from a direct ray-tracing through numerical weather models represents the current water vapor occurrence more precisely than the empirical approach of Niell. However, the SSNP derived from the VMF processing with a mean value of 9.9 cm over the year 2005 are still significant and may not be neglected. If the a priori model became more accurate by using the VMF, the SSNP would attain even smaller values and might be omitted. If such an achievement of the a priori model became possible, the computation of the total zenith path delay illustrated in Figure 3.7 could be simplified.

Table 3.8: Mean differences of the SSNP in cm w.r.t. NMF and VMF

Time period	01-01-2005 to 10-01-2005	01-07-2005 to 10-07-2005	over the whole year 2005
Mean SSNP NMF	11	16	12
Mean SSNP VMF	7	14	10

The date is given in the form DD-MM-YYYY in Table 3.8. Obviously, the mean SSNP values for both NMF and VMF are much larger in the first ten days of July 2005 than in the first ten days of January 2005. Besides the annual trend, this might also be explained by short-term weather occurrences causing a turbulent atmosphere. On the web page

http://www.wetterzentrale.de/topkarten/fskldwd.html (13.03.2014)

daily mean, minimum, and maximum temperatures, the amount of precipitation per day, as well as the maximum wind velocity from sites of the German Weather Service (Deutscher Wetterdienst) are provided. In Karlsruhe, a precipitation of 20.2 mm has been recorded on July 4, 2005, whereas the maximum precipitation value within the considered period in January 2005 equals only 5.2 mm at this site. The maximum wind speed is also much higher within the days in July.

No seasonal dependence of the SSNP related to the $\sin \varepsilon$ term occurring in the determination of the Niell mapping function has been identified. The sums of the respective a priori models from NMF and VMF and their corrections represented by the SSNP are exemplary shown for the observing site 0388 (Iffezheim) in Figure 3.15. Although the differences vary of about ± 5 mm over the year, their mean difference over the year 2005 equals 0.3 mm. Hence, the differences between the total delays from NMF and VMF are not systematic, but attain both positive and negative values. This might be explained by the ability of VMF to represent short-scale temporal variations that cannot be modeled by NMF.
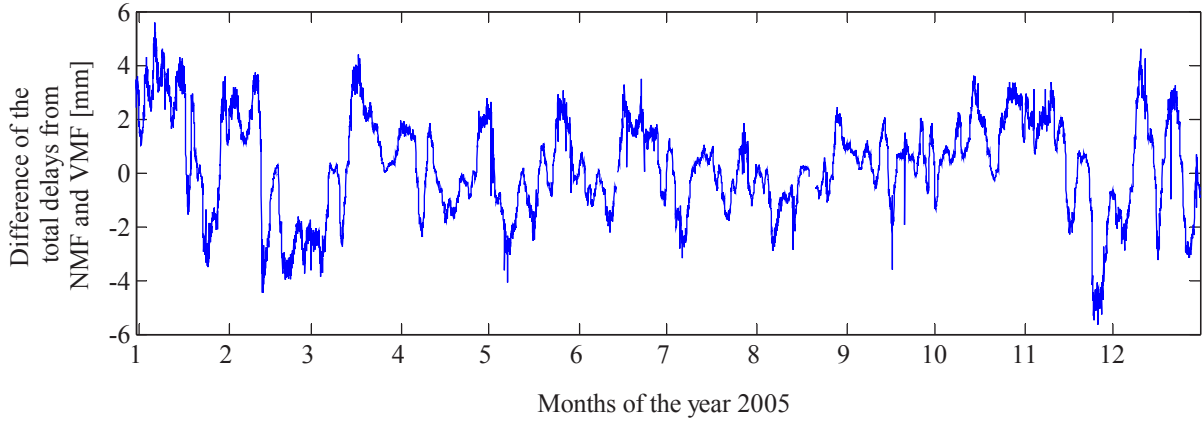
Figure 3.15: Differences between the total delays deduced from the two mapping functions at site Iffezheim (0388); VMF − NMF

Contrary to the SSNP, the computed horizontal gradients from NMF and VMF agree within the submillimeter. As shown in Figure 3.16, there are no systematic differences in the gradients deduced by NMF or VMF. Consequently, the horizontal gradients determined from observations down to $\varepsilon = 3°$ can be neglected at the considered elevation angles of $\varepsilon > 45°$.

3.5 Phase residuals

Besides the SSNP and horizontal gradients, phase residuals also represent a valuable contribution to the wet delay from GNSS. They are assumed to represent a large part of the satellite-directed wet delay. Within Bernese, these phase residuals $\hat{v}$ are determined additional to the parameters $\hat{x}$ within a least squares adjustment

$$l + \hat{v} = A \cdot \hat{x} \tag{3.23}$$

where the matrix A stands for the functional dependence of $\hat{x}$ on the observations l. Generally they are considered as corrections to the observations

$$\hat{v} = \hat{l} - l \tag{3.24}$$

and contain useful information about the neutrospheric water vapor. However, the phase residuals also contain other components not modeled within section 3.2, such as multipath effects especially. These multipath effects still represent an important limitation of high-precision GNSS observations. Here, these residuals represent the only possibility of getting a non-averaged signal component exactly pointing from the receiver to the GPS satellite. The SSNP are averaged values w.r.t. time and space referring to the considered observing site and not to a particular GPS satellite. This is due to the observation geometry of GPS illustrated in Figure 3.17. For each site, one single neutrospheric delay is obtained from all signals received within an averaging cone with a vertex at the observing site and a radius dependent of the minimum elevation ε_{min}. Due to the absence of GNSS satellites over the poles, the averaging cone is anisotropic. Moreover, the residuals are temporally much higher resolved than the SSNP.
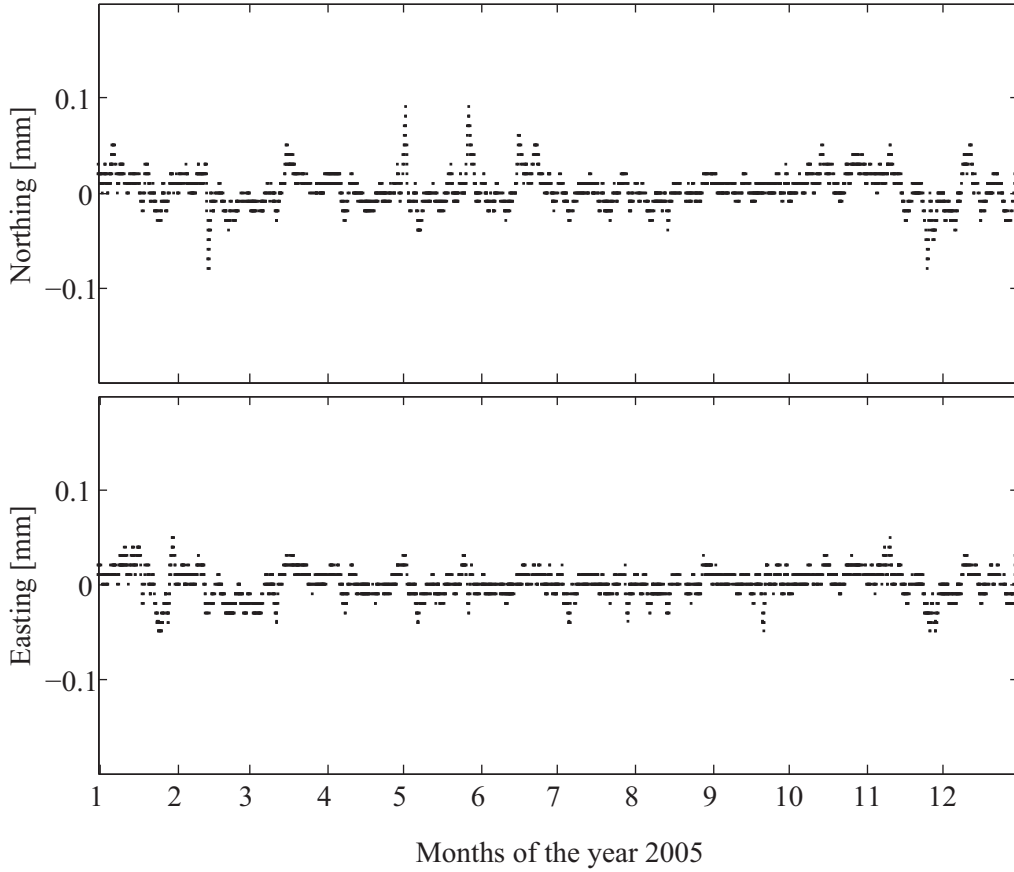
Figure 3.16: Differences of the horizontal gradients in Northing and Easting at site 0388 (Iffezheim): VMF − NMF

Whereas one single SSNP value is estimated per hour within this thesis, the residuals are computed for each epoch of 30 seconds.

Contrary to the SSNP given in zenith direction at a temporal sampling of one hour, phase residuals are computed for each observation l, i.e. every 30 seconds. They are written to residual files also containing the respective elevation and azimuth values of the GPS satellite. Bernese distinguishes three kinds of residuals. The user can choose between normalized and real residuals and an option called NORM APRIORI. Real residuals correspond to the values resulting from (3.24) and are computed with respect to the ionosphere-free linear combination L_3 used in the analysis. According to Dach et al. [2007], normalized residuals are calculated from

$$\hat{v}_{norm}(i) = \frac{\hat{v}_i}{\sqrt{C_{\hat{v}_i \hat{v}_i}}} \tag{3.25}$$

where $C_{\hat{v}\hat{v}}$ stands for the cofactor matrix of the residuals computed from the difference of the inverse weighting matrix P^{-1} of the available observations and the cofactor matrix $C_{\hat{l}\hat{l}}$ of the adjusted observations

$$C_{\hat{v}\hat{v}} = P^{-1} - C_{\hat{l}\hat{l}} \tag{3.26}$$

with

$$C_{\hat{l}\hat{l}} = A(A^T P A)^{-1} A^T \tag{3.27}$$

Contrary to the real residuals, normalized residuals refer to the L_1 signal. Finally, the option NORM APRIORI enables a transformation of real residuals to normalized residuals by means of the a priori variance of the observations

$$C_{\hat{v}\hat{v}} \approx P^{-1} \tag{3.28}$$
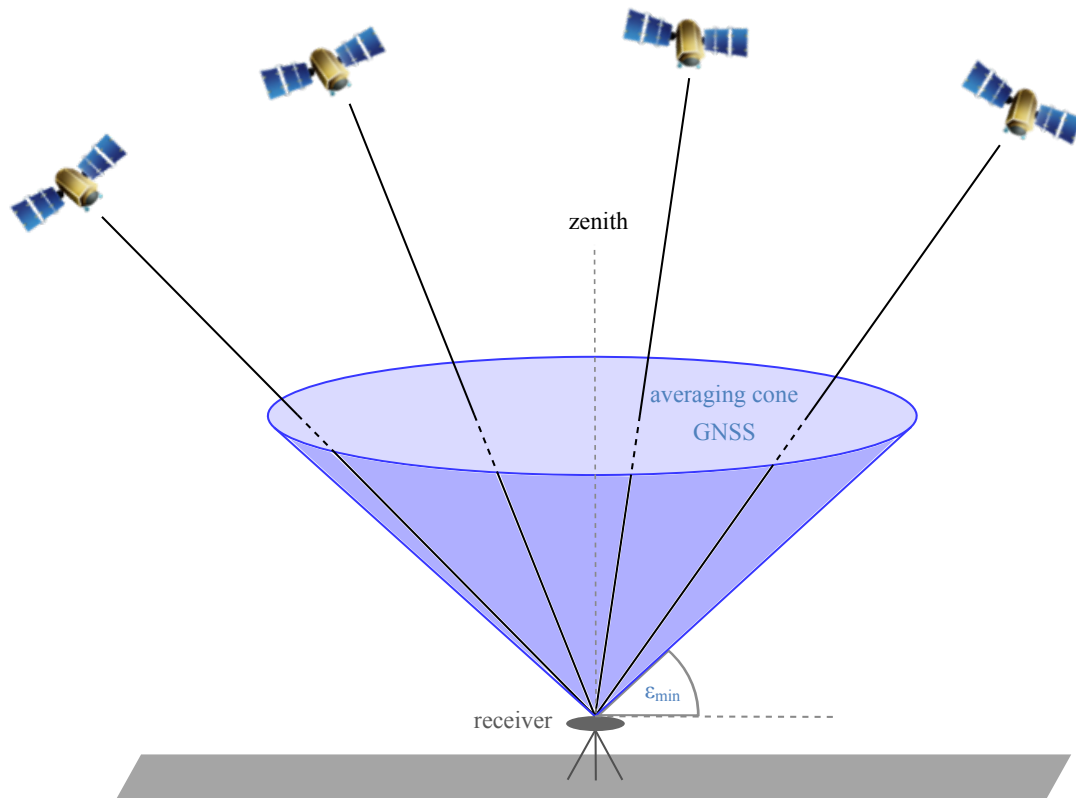
Figure 3.17: Temporal and spatial conic averaging property of the GNSS-based path delay

For the comparison of neutrospheric delays deduced from GPS and InSAR observations, no normalization is desired. However, as the real residuals computed in Bernese refer to the L_3 signal, they are unsuitable, too. For this reason a modified routine RESOUT.f computing real residuals with reference to L_1 has been implemented according to the modifications described in Fuhrmann et al. [2010]. They correspond to the values of $\hat{v}_i$ in (3.25) before division by $\sqrt{C_{\hat{v}\hat{v}}}$. As both the effects of multipath and water vapor are observed in the phase residuals, the residuals have to be properly analyzed before simply being added to the other components that are shown in Figure 3.7 in section 3.2.

3.6 Summary

In this chapter, neutrospheric modeling by applying the technique of PPP to the GNSS observations was described. The recent processing was carried out based on GPS observations only. The necessity of accurate mapping functions to account for the bending effect at low elevations led to a comparison of NMF and VMF. These mapping functions are both based on the Marini continued fraction form and distinguish dry and wet mapping. In contrast to the empirical NMF, the VMF is based on direct ray-tracing through NWMs. In general, the SSNP computed based on the VMF were smaller than those deduced from NMF, but the total delays derived from VMF showed strong agreement with those of NMF. The horizontal gradients in longitude and latitude direction did not significantly vary depending on the selected mapping function. The annual standard deviations of a site's height was larger in the case of NMF than in the case of VMF. Consequently the VMF a priori model determined by ray-tracing seemed to represent the actual neutrospheric patterns more accurately than the empirical NMF. Finally, the determination strategy of the phase residuals representing a satellite-direction contribution to the neutrospheric path delay was explained. Whereas the choice of an appropriate mapping function has been classified as important in the case of water vapor retrieval, both NMF and VMF yielded comparable accuracies in the height determination.

# 4 Neutrospheric delay in Interferometric Synthetic Aperture Radar data

Massonnet et al. [1994] first suspected significant errors to Interferometric Synthetic Aperture Radar measurements of the Landers earthquake to be caused by neutrospheric gases. Later, researches confirmed the assumption that neutrospheric water vapor affected the propagation of the radio waves transmitted by the SAR. Neutrospheric corrections have to be performed within InSAR observations in a similar way as in the case of GNSS. Even one more step can be done by comparing independent water vapor products derived from InSAR and GNSS data. In this way, a rigorous fusion of the data from both sensors for the purpose of water vapor retrieval might be achieved. Further improvements of the existent water vapor maps from GNSS and InSAR observations could become possible. As an important step into this direction, partial wet delay maps from InSAR and the corresponding maps deduced from acquisitions of MERIS are compared here. This enables an evaluation of the available interferograms with respect to the selected master and the results of the inversion discussed in 4.3.1 and 4.3.3. Section 4.1 presents the input data. In section 4.2, there is an overview given of the different processing steps required for the interferogram formation within the applied Stanford Method for Persistent Scatterers (StaMPS). In section 4.3, both InSAR and MERIS observations are converted to comparable quantities, i.e. wet delays. Moreover, the effect of the selected master image on the agreement between the partial zenith wet delays deduced from InSAR and MERIS is shown. Finally, the conventional master selection algorithm is compared to new considerations that result from InSAR processing with the aim of atmosphere modeling.

4.1 Input data sets

In the following subsections, the two instruments MERIS and ASAR on board of the Environmental Satellite (Envisat) as well as the data deduced from their observations are presented. InSAR provides measurements of the interferometric phase and MERIS provides simultaneous maps of the atmospheric water vapor.

4.1.1 InSAR observations from Envisat ASAR

InSAR measurements are based on the interferometric principle, i.e. differences of two simple ASAR acquisitions are computed for any further analysis. In contrast to the pointwise measurements originating from GNSS observations, SAR acquisitions yield images of wide areas. The viewing geometry of ASAR is schematically represented in Figure 4.1. In order to obtain interferograms from this kind of single SAR acquisition, a second, spatially and/or temporally separated acquisition is used. The distance between the antennas at the two acquisitions is known as geometric baseline, and the difference in time is called temporal baseline. Moreira [2000] distinguishes two different modes of SAR interferometry. In across-track interferometry, the antennas are spatially arranged such that a baseline component across the flight direction is generated. This configuration is of particular interest when determining the terrain topography of the observed area. Contrary to this mode, along-track interferometry benefits from geometric baselines parallel to the flight direction in order to detect long-term surface motions. In this case, the antennas are situated on the same orbit, but shifted spatially in the direction of flight. In the case of the neutrospheric modeling from measurements of the ASAR instrument, the two SAR observations producing the interferogram are acquired from two flyovers in along-track interferometry. Within this so-called repeat pass interferometry,
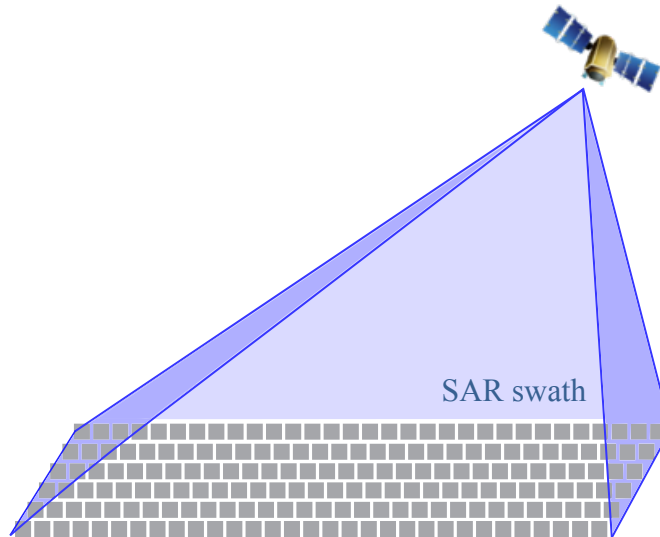
Figure 4.1: Viewing geometry of a single SAR acquisition

temporal decorrelation is particularly problematic (Hooper et al. [2007]). The coherence representing the degree of correlation between the two SAR acquisitions plays a decisive role. Besides classical approaches of the SAR interferometry that apply multilooking to suppress noise and to increase the obtained correlation, Persistent Scatterer (PS) InSAR overcomes this correlation problem by defining the constant backscattering characteristic of the points, i.e., persistent scatterers.

4.1.2 Measurements of Envisat MERIS instrument

The MERIS instrument, a passive 68.5° field-of-view nadir looking push-broom imaging spectrometer, observes the solar radiation reflected by the Earth (ESA [2006]). Its main mission is the observation of the sea color from which the chlorophyll pigment concentration can be determined. Several other applications within ocean, land, and atmospheric missions are also ensured by MERIS. In our context, its atmospheric mission yielding the column amount of water vapor is of particular interest. The instrument measures in 15 spectral bands at wavelengths from the visible violet at 390 nm to the near infrared around 1040 nm. MERIS produces column water vapor images of a maximum resolution of 290 m x 260 m at the sub-satellite point. These images are derived through intermediate processing steps from directly measured top of atmosphere radiances at the bands 14 and 15.

Channel	Band center [nm]	Band width [nm]
14	885	10
15	900	10

As illustrated in Figure 4.2, channel 15 is located at the shortwave edge of a water vapor absorption band. In contrast, wavelengths of 885 nm are transmitted almost without absorption.
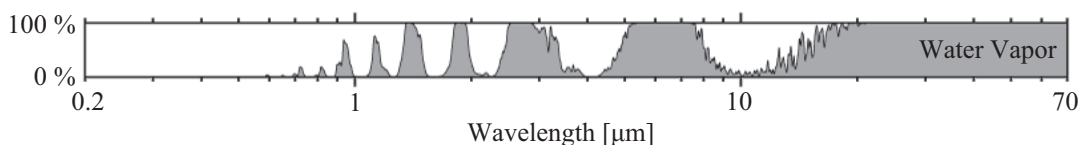
Figure 4.2: Absorption of water vapor from Rohde: channel 15 is located at 900 nm at the shortwave edge of a water vapor absorption band

Based on the law of Lambert-Beer and assuming an idealized non-scattering atmosphere, unsaturated absorption, and monochromatic radiation, the columnar water vapor w can be deduced from the transmission Γ (Fischer and Bennartz [1997])

$$\Gamma(w, \lambda_i) = \frac{L(w, \lambda_{15})}{L(w = 0, \lambda_{15})} = e^{-\alpha(\lambda_{15}) \cdot w} \tag{4.1}$$

where $\alpha(\lambda_i)$ represents the absorption coefficient at the absorption wavelength λ_{15}, and $L(w, \lambda_{15})$ is the measured solar radiance at wavelength λ_{15} after passing the columnar water vapor w.

Consequently:

$$w = -\frac{1}{\alpha(\lambda_{15})} \cdot \ln\left(\frac{L(w, \lambda_{15})}{L(w = 0, \lambda_{15})}\right) \tag{4.2}$$

While $L(w, \lambda_{15})$ is directly measured, an estimation of $L(w = 0, \lambda_{15})$ has to be deduced from observations at the wavelength λ_{14}.

$$w = -\frac{1}{\alpha(\lambda_{15})} \cdot \ln\left(\frac{L(w, \lambda_{15})}{L(\lambda_{14})}\right) \tag{4.3}$$

However, the assumptions made above are still not valid in praxis, and hence, a correction term is added in (4.3) to obtain w:

$$w = k_0 + k_1 \cdot \ln\frac{L(w, \lambda_{15})}{L(\lambda_{14})} + k_2 \cdot \ln^2\frac{L(w, \lambda_{15})}{L(\lambda_{14})} \tag{4.4}$$

The regression coefficients k_0, k_1, and k_2 depend on the surface type (water – land – clouds), the viewing geometry and illumination as well as on the cloud properties. As a result, the algorithm takes into account the different scenarios given in the atmospheric observations by determining the respective coefficients from an adapted lookup table.

4.2 Persistent Scatterer Interferometry with the Stanford Method

The Stanford Method for PS (StaMPS) aims at identifying PS pixels and estimating their interferometric phases even in natural terrains without dominant, man-made scatterers. These resulting phases contain different signal parts that have to be separated depending on the aspired physical observable. The unwrapped phase $\Phi_{x,j}$ in the xth pixel of the jth SAR interferogram corrected for topography and flat earth phases consists of the following components

$$\Phi_{x,j} = \Phi_{def_{x,j}} + \Phi_{atm_{x,j}} + \Phi_{orb_{x,j}} + \Phi_{\varepsilon_{x,j}} + n_{x,j} \tag{4.5}$$

explained by Hooper et al. [2004] as:

$\Phi_{def_{x,j}}$	deformation phase due to the movement of the pixel in the line-of-sight
$\Phi_{atm_{x,j}}$	phase difference due to atmospheric delay between the two passes
$\Phi_{orb_{x,j}}$	phase due to orbit inaccuracies
$\Phi_{\varepsilon_{x,j}}$	residual topographic phase caused by errors in the DEM
$n_{x,j}$	Noise

The atmospheric phase maps were prepared for this study as presented in Alshawaf [2013]. In this section, a very brief overview of the processing steps of StaMPS is presented.

4.2.1 Processing steps within StaMPS

1. First of all, N interferograms are formed from the phases of $N+1$ Single Look Complex (SLC) SAR acquisitions coregistrated to a single common master. This pre-processing step is done within the Delft object-oriented radar interferometric software (Hooper et al. [2010]). In an earlier paper, Hooper et al. [2007] recommend to use at least twelve interferograms in order to properly identify the PS points.

All N interferograms are computed with reference to their common master image:

$$\Phi_{interferogram(j)} = \Phi_{master} - \Phi_{slave(j)} \tag{4.6}$$

with $j = 1 \ldots N$.

As described in Hooper et al. [2007], the master selection is based on a minimization of the sum of decorrelation, or inversely, a maximization of the sum of correlation.

$$\sum_{i=1}^{N} \rho_{total} \to max \tag{4.7}$$

where

$$\rho_{total} = \rho_{temporal} \cdot \rho_{spatial} \cdot \rho_{doppler} \cdot \rho_{thermal} \tag{4.8}$$

with

$\rho_{temporal}$	correlation depending on the temporal baseline B_{temp}
$\rho_{spatial}$	correlation depending on the perpendicular baseline $B_{\perp}$
$\rho_{doppler}$	correlation depending on difference ΔDC in Doppler centroid
$\rho_{thermal}$	correlation depending on thermal noise that is assumed to be constant

All the baselines with reference to the master acquisition 29-11-2004 are visualized in Figure 4.3.
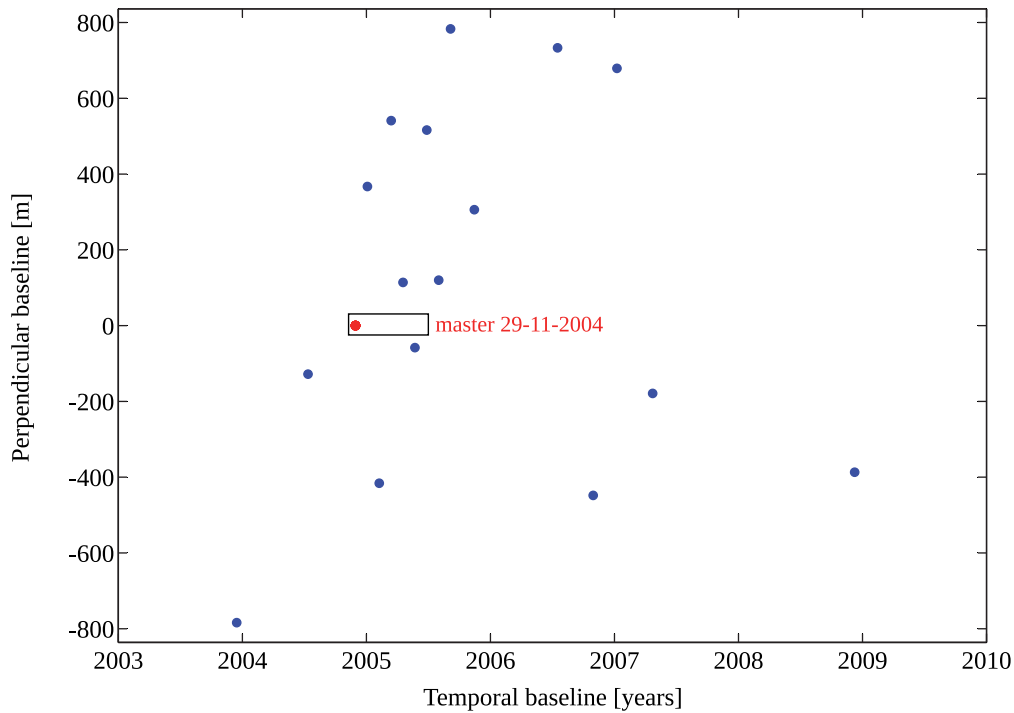
Figure 4.3: Baseline plot with respect to the master 29-11-2004; The SAR images were acquired between 2003 and 2009, but the most concentrate in 2005.

We tested four different master images, hence $4 \cdot 16$ interferograms were analyzed such that they have maximum baselines of

- $B_{temp,\ max} \approx 4$ years

- $B_{\perp,\ max} \approx 1300$ m

However, the master selection based on the approach of Hooper et al. [2007] does not take into account the atmosphere's respective character. Section 4.3 shows that it might make sense to introduce additional information into the master selection process in order to obtain a smooth master atmosphere. This is of particular relevance in case of a small number of available SAR acquisitions. Moreover, the computed interferograms still contain a phase component resulting from the different acquisition geometries of the master and slave acquisitions. These geometric effects are corrected by flattening the interferograms. This is done by assuming a reference ellipsoid scattering surface and estimating the phase difference between this reference ellipsoid and the real topography by means of a Digital Elevation Model. Additionally, the topographic phase component contained within the interferograms has to be removed.

2. In a second step of the StaMPS algorithm, Hooper et al. [2007] estimate the phase stability of each pixel. An initial selection of pixels that might be PS candidates is performed depending on the amplitude dispersion index D_A:

$$D_A = \frac{\sigma_A}{\mu_A} \tag{4.9}$$

The variables σ_A and μ_A in (4.9) represent the standard deviation and the mean value of a series of amplitude values. In a following iterative step, a phase analysis completes the phase stability estimation. The higher the threshold D_A, the more pixels are selected. Typically, a value of $D_A \approx 0.4$ is used in StaMPS, which is also suitable for the test site URG.

3. Based on the determined phase stability, pixels dominated by Persistent Scatterers are selected in the third part of the algorithm.

4. Finally, the estimation of the aspired observable's phase is performed. Only those pixels classified as dominated by Persistent Scatterers are considered. In order to deduce meaningful information without ambiguities on the chosen observable from (4.6), phase unwrapping is necessary.

4.2.2 Application of StaMPS to the available SAR data

The available data set used for the following analysis consist of $N = 17$ SAR acquisitions yielding 16 interferograms. The respective acquisition dates are given in Table 4.1. The number of 17 SAR acquisitions is theoretically large enough for PS InSAR, but in section 4.3 it is demonstrated that information deduced from a small number of interferograms has to be critically analyzed.

Table 4.1: Dates of available SAR acquisitions

15-12-2003	12-07-2004	29-11-2004	03-01-2005	07-02-2005	14-03-2005
18-04-2005	23-05-2005	27-06-2005	01-08-2005	05-09-2005	14-11-2005
17-07-2006	30-10-2006	08-01-2007	23-04-2007	08-12-2008	

It is assumed that the deformation in the Upper Rhine Graben within the analyzed time period from December 2003 to December 2008 is negligible, i.e. assuming $\Phi_{def_{x,j}} = 0$. According to Fuhrmann et al. [2013], this assumption of a stable surface within the GURN region is acceptable. The surface deformation within the GURN region attains maximum values of 0.5 mm per year. After the subtraction of the remaining orbital errors $\Phi_{orb_{x,j}}$ and errors $\Phi_{\varepsilon_{x,j}}$

in the DEM introduced into the processing, atmospheric effects $\Phi_{atm_{x,j}}$ can be extracted from the unwrapped phase from (4.5):

$$\Phi_{atm_{x,j}} = \Phi_{x,j} - \Phi_{def_{x,j}} - \Phi_{orb_{x,j}} - \Phi_{\varepsilon_{x,j}} - n_{x,j} \qquad (4.10)$$

According to Hooper et al. [2007], the estimation of the respective components that have to be reduced is based on a combined temporal and spatial filtering. The noise component $n_{x,j}$ is also removed by this filtering.

Table 4.2: Numbers of PS points detected with reference to the four master acquisitions

Master acquisition date	29-11-2004	07-02-2005	18-04-2005	27-06-2005
Number of PS points	169688	158582	83793	185524
Selection	second master candidate according to Hooper et al. [2007]	Winter acquisition	first master candidate according to Hooper et al. [2007]	MERIS non-cloudy weather conditions

Among the above SAR acquisitions, the four dates 29-11-2004, 07-02-2005, 18-04-2005, and 27-06-2005 have been selected as master images for the comparison of InSAR and MERIS presented in section 4.3 as well as for the rigorous comparison of the contributions of InSAR and GNSS to the wet delay presented in chapter 5. Thus, $4 \cdot 16$ interferograms are available. Two of the four masters (29-11-2004 and 18-04-2005) have been chosen according to the approach of Hooper et al. [2007] as detailed below. Independent of this approach, the SAR acquisition 27-06-2005 has been selected because of the availability of MERIS data. A general consideration of seasonal weather conditions finally led to the choice of the SAR image acquired on 07-02-2005. It is assumed to represent a smooth, dry winter atmosphere. The numbers of PS points detected with reference to the respective master acquisitions are given in Table 4.2. In case of the master acquisition 18-04-2005, only about half of the PS points of the other master images are found. According to StaMPS setup parameters, the amplitude dispersion index was set to $D_A = 0.4$ in the processings of all of the above introduced data sets. The threshold determining the weeding of the noisy PS pixels was set to 0.57 for all cases. All other processing parameters have also been kept constant. Consequently, the obvious change in the number of detected PS points of master 18-04-2005 must be independent of the processing settings. The results of section 4.3 indicate a possible relationship between the number of detected PS points and the neutrospheric characteristics at the master date.

4.3 Analysis of InSAR and MERIS data

When InSAR and MERIS data are to be compared, they first of all have to be converted into comparable quantities. So far, InSAR observations are available in terms of interferometric phases $\Phi_{interferometric_j}$, representing the signal delay on its path from the satellite to the scatterer on the Earth's surface and back to the satellite. In contrast, the available MERIS product describes the Integrated Water Vapor (IWV) measured in vertical direction to the sub-satellite point. Thus, different conversions are necessary to obtain information on the neutrospheric delay from each of the two sensors.

4.3.1 Conversion from InSAR interferometric phases to neutrospheric delays

Four main processing steps illustrated in Figure 4.4 are necessary to convert the interferometric phases $\Phi_{interferometric_j}$ to neutrospheric zenith delays $\Delta_{acq_{i\ interpolated}}^{zenith}$ interpolated within the MERIS resolution cells.

The aim of meteorologists and geodesists is not to obtain information on the difference of neutrospheric delays between two acquisition dates, but to deduce delays of each acquisition time. These can be derived by applying least squares inversion. The 16 maps of interferometric phases have to be transformed into $N = 17$ phase images per

acquisition. The inverse model is under-determined and a condition is introduced to obtain an invertible problem. The constraint is

$$0 = \frac{1}{N} \cdot \Phi_{acq_1} + \frac{1}{N} \cdot \Phi_{acq_2} + \ldots + \frac{1}{N} \cdot \Phi_{acq_{N-1}} + \frac{1}{N} \cdot \Phi_{acq_N} \tag{4.11}$$

For each pixel in the $N-1$ interferograms, we have

$$\underbrace{\begin{pmatrix} \Phi_{interferometric_1} \\ \Phi_{interferometric_2} \\ \vdots \\ \Phi_{interferometric_{N-2}} \\ \Phi_{interferometric_{N-1}} \\ 0 \end{pmatrix}}_{l \qquad N \times 1} = \underbrace{\begin{pmatrix} -1 & & & 1 & & & \\ & \ddots & & 1 & & & \\ & & -1 & 1 & & & \\ & & & 1 & -1 & & \\ & & & 1 & & \ddots & \\ & & & 1 & & & -1 \\ \frac{1}{N} & \cdots & \frac{1}{N} & \frac{1}{N} & \frac{1}{N} & \cdots & \frac{1}{N} \end{pmatrix}}_{A \qquad\qquad N \times N} \cdot \underbrace{\begin{pmatrix} \Phi_{acq_1} \\ \Phi_{acq_2} \\ \vdots \\ \Phi_{acq_{N-1}} \\ \Phi_{acq_N} \end{pmatrix}}_{x \qquad N \times 1} \tag{4.12}$$

$\Phi_{interferometric_j}$

least squares inversion

Φ_{acq_i}

$\Delta^{slant} = -\Phi \cdot \frac{\lambda}{4\pi}$

$\Delta^{slant}_{acq_i}$

$\Delta^{zenith} = \cos\theta \cdot \Delta^{slant}$

$\Delta^{zenith}_{acq_i}$

interpolation

$\Delta^{zenith}_{acq_i\ interpolated}$

Figure 4.4: Conversion from interferometric phases to delays per acquisition

However, the above regularization makes only sense if the pixelwise average of the atmospheric phases of the N acquisitions can really be assumed zero. Otherwise the inversion might yield biased results.

The available 17 SAR acquisitions do not represent a large data set. For this reason, the results of the least squares inversion and their relation to the master atmosphere smoothness are analyzed in chapter 4.3.3 by comparing them to MERIS IWV maps. In a second step, Zebker et al. [1997] convert the obtained phase Φ_{acq_i} with reference to acquisition i into delays Δ_{acq_i} by means of

$$\Delta^{slant}_{acq_i} = -\Phi_{acq_i} \cdot \frac{\lambda}{4\pi} \tag{4.13}$$

As the viewing geometries of InSAR and MERIS are different, the obtained InSAR delays must be mapped from the slant direction to the zenith direction in order to enable a comparison with MERIS data:

$$\Delta^{zenith}_{acq_i} = \cos\theta \cdot \Delta^{slant}_{acq_i} \tag{4.14}$$

Here, a constant value of $\theta = 23.5°$ has been used to convert the slant delays into zenith delays. In reality, according to Holzner et al. [2002], the incidence angle of the Envisat ASAR instrument varies between $18.6°$ and $26.2°$ from near range to far range within the 100 km wide image swath. Finally, InSAR delay values are interpolated within the MERIS resolution cells of about 300 m $\times$ 300 m to enable a direct comparison.

4.3.2 Conversion from integrated water vapor to neutrospheric delays

The zenith wet delay Δ^{zenith}_{wet} is related to the IWV by

$$IWV = \kappa \cdot \Delta^{zenith}_{wet} \tag{4.15}$$

with the scaling factor κ in kg/m^3

$$\kappa = \frac{10^6}{\left[k_2' + \dfrac{k_3}{T_m}\right] \cdot R_v} \tag{4.16}$$

Here, k_2' and k_3 are refractivity constants related to the ratio of the molar masses of water vapor and dry air and R_v is the specific gas constant for water vapor. The value of κ depends largely on the weighted mean temperature T_m of the atmosphere, which determination is explained below.

Bevis et al. [1994] added the density of liquid water ρ to the denominator yielding the Precipitable Water PW

$$\text{PW} = \frac{IWV}{\rho} = \frac{\kappa \cdot \Delta_{wet}}{\rho} = \Pi \cdot \Delta_{wet} \tag{4.17}$$

with the dimensionless scaling factor Π

$$\Pi = \frac{10^6}{\rho \cdot \left[k_2' + \dfrac{k_3}{T_m}\right] \cdot R_v} \tag{4.18}$$

Of course, the unit changes as a function of the density of liquid water ρ. The IWV is expressed in kg/m^2, whereas the PW is known in units of mm. Besides this, the numerical values of both quantities can be considered as equivalent. The scaling factors are related by the equation

$$\Pi = \frac{\kappa}{\rho} \tag{4.19}$$

where ρ for water is

$$\rho = 1 \, \text{g/cm}^3 = 10^{-3} \, \text{kg}/10^{-6} \text{m}^3 = 1000 \, \text{kg/m}^3 \tag{4.20}$$

For the computation of κ and Π, the integrated mean temperature T_m of the atmosphere

$$T_m = \frac{\int\limits_{h_0}^{\infty} (e/T) \, \mathrm{d}z}{\int\limits_{h_0}^{\infty} (e/T^2) \, \mathrm{d}z} \tag{4.21}$$

is used in (4.16) with e standing for the partial pressure of water vapor in hPa and T for temperature in K within the considered vertical profile.

However, in order to obtain values for T_m, vertical profiles of water vapor and of the temperature are necessary. Such profiles can, for example, emanate from radiosonde measurements or numerical weather models. Instead of using measured or predicted water vapor and temperature profiles, T_m can also be estimated by means of an empirical model

$$T_m \approx 70.2 + 0.72 \cdot T_0 \tag{4.22}$$

where T_0 represents the surface temperature in K at the considered observing site.

Within this study, κ or Π have been derived based on (4.22), where the surface temperature T_0 resulted from spatially interpolated meteorological observations at three different sites within the considered SAR frame. One single value of κ or Π has been determined for each of the 17 SAR acquisitions.

Boehm and Schuh [2013] state that errors in Π are mostly caused by errors in the computed mean temperature T_m of the atmosphere.

$$\frac{\partial \Pi}{\partial T_m} = \frac{10^6 \cdot k_3}{\rho \cdot R_v \cdot \left[k_2' + \dfrac{k_3}{T_m}\right]^2 \cdot T_m^2} = \frac{10^6 \cdot k_3}{\rho \cdot R_v \cdot \left(k_2' \cdot T_m + k_3\right)^2} \tag{4.23}$$

Using

$$k'_2 = 0.229733 \text{ Kms}^2\text{kg}^{-1} \tag{4.24}$$

$$k_3 = 3754.64 \text{ K}^2\text{ms}^2\text{kg}^{-1} \tag{4.25}$$

$$R_v = 461.5 \text{ m}^2\text{s}^{-2}\text{K}^{-1} \tag{4.26}$$

as in Boehm and Schuh [2013] and assuming a mean atmospheric temperature of $T_m = 270$ K, values of $\kappa \approx 153$ kg/m^3 and $\Pi = 0.153$ result. Contrary to the value given in the first edition of Boehm and Schuh [2013], an increase of T_m by 4 K then yields a change in κ of 2.2 kg/m^3.

Once the MERIS measurements are converted into zenith wet delays, they still do not correspond to the zenith wet delays deduced from InSAR. This is due to the interferometric nature of InSAR. The observed zenith InSAR delays result from partial phases obtained in (4.6) from two SAR acquisitions of the same SAR frame. Neutrospheric effects of the dry delay are therefore eliminated. Moreover, orbit errors observed as linear ramps within the interferograms are corrected within the InSAR processing. Hence, possible linear trends of the neutrospheric delays are also reduced. In order to achieve a rigorous comparison of MERIS and InSAR data, these topography-dependent and long-wavelength components have to be subtracted from the obtained MERIS delay values.

For this reason, a DEM associated with the MERIS data has been used in order to estimate the linear dependency of the zenith wet delay values on the altitude H. Two parameters k and t are estimated for the $N = 17$ acquisitions.

$$\underbrace{\begin{pmatrix} \Delta^T_{acq_1} \\ \Delta^T_{acq_2} \\ \vdots \\ \Delta^T_{acq_{N-1}} \\ \Delta^T_{acq_N} \end{pmatrix}}_{l \qquad N \times 1} = \underbrace{\begin{pmatrix} H_1 & 1 \\ H_2 & 1 \\ \vdots \\ H_{N-1} & 1 \\ H_N & 1 \end{pmatrix}}_{A \qquad N \times 2} \cdot \underbrace{\begin{pmatrix} k \\ t \end{pmatrix}}_{x \quad 2 \times 1} \tag{4.27}$$

The topography-dependent part with the superscript T is

$$\Delta^T_{acq_i} = k \cdot H_i + t \tag{4.28}$$

These delay components are then subtracted, which yields a topography-independent part labeled with the superscript $\overline{T}$:

$$\Delta^{\overline{T}}_{acq_i} = \Delta_{acq_i} - \Delta^T_{acq_i} \tag{4.29}$$

Additional linear trends L are modeled depending on the longitudes λ and the latitudes φ

$$\underbrace{\begin{pmatrix} \Delta^L_{acq_1} \\ \Delta^L_{acq_2} \\ \vdots \\ \Delta^L_{acq_{N-1}} \\ \Delta^L_{acq_N} \end{pmatrix}}_{l \qquad N \times 1} = \underbrace{\begin{pmatrix} \lambda_1 & \varphi_1 & 1 \\ \lambda_2 & \varphi_2 & 1 \\ \vdots \\ \lambda_{N-1} & \varphi_{N-1} & 1 \\ \lambda_N & \varphi_N & 1 \end{pmatrix}}_{A \qquad N \times 3} \cdot \underbrace{\begin{pmatrix} p_1 \\ p_2 \\ p_3 \end{pmatrix}}_{x \quad 3 \times 1} \tag{4.30}$$

Then the partial wet delay $\Delta^{zenith}_{acq_i \, MERIS}$ from MERIS is

$$\Delta^{zenith}_{acq_i \, MERIS} = \Delta^{\overline{T}}_{acq_i} - \Delta^L_{acq_i} \tag{4.31}$$

Of course these models cannot exactly represent the trends of the delay that are reduced within the InSAR processing. They only constitute a good approximation. The remaining deviations between the obtained InSAR and MERIS zenith partial delays might be eliminated by using more sophisticated models. Figure 4.5 illustrates the contributions of the different components to the delay. Two acquisitions are compared in this figure. On

23-04-2007, turbulent patterns are visible, whereas 05-09-2005 represents an acquisition with a lower neutrospheric activity. The similar behavior of the estimated topography-dependent components is apparent. Yet, due to the changing atmosphere, the linear trend differs clearly between the two data sets. These figures demonstrate the difference between total wet delays (as measured by MERIS or GNSS) and partial wet delays observed by InSAR. Each interferogram produces maps of two partial wet delays, the partial wet delay in the master and the slave acquisitions. The notation "partial" here expresses the fact that some components are missing in these observed delays. In order to get comparable observations, this topography-dependent part as well as a linear trend have been estimated and reduced from the MERIS data before the comparison with InSAR.

4.3.3 Comparison of InSAR and MERIS neutrospheric delays

If both InSAR and MERIS observations are transformed to partial zenith wet delays per acquisition, they can be properly compared. Here, the maps of delays per acquisition deduced from InSAR are compared to MERIS observations at those days, where sufficient MERIS data are available. Large data gaps as shown in Figure 4.6 can occur within the MERIS acquisitions in case of cloudy weather conditions, but for the days 27-06-2005, 05-09-2005, 17-07-2006, and 23-04-2007 accurate information without large gaps is available for the whole SAR frame.

Though, due to clouds there still appear small holes around which the estimated IWV values are not reliable. These data gaps or underestimated observations have been eliminated by simple filtering in the respective regions. After the conversion from IWV to delays and the reduction of the topographic and linear trends, all delay values below a threshold of -5 mm are removed in the framed zone in Figure 4.7. Moreover, outliers deviating more than 4σ from the mean of the remaining cells are detected and removed, with σ representing the standard deviation of the remaining cells.

As SAR acquisitions deduced from different master images are considered, the number of PS points per SAR image changes depending on the respective master. Therefore, all InSAR delays are interpolated by means of quadratic inverse distance weighting onto the PS points of the master acquisition 18-04-2005, containing the fewest PS points (83793). Alternatively, Alshawaf [2013] achieved the interpolation by ordinary Kriging to compare MERIS and InSAR data.

In the case of inverse distant weighting, a data set X_2 shall be interpolated to a data set X_1. For each PS point x_i of the data set X_1, the distances to all PS points x_j of this source data set X_2 lying within a certain interpolation radius r_{int} around x_i are computed. Here, this is done based on the geographic coordinates λ_i, φ_i, λ_j, and φ_j of the points x_i and x_j. The interpolation radius r_{int} is set to 300 m by referring approximately to the MERIS resolution cell size.

$$d(x_i, x_j) = \sqrt{(\lambda_i - \lambda_j)^2 + (\varphi_i - \varphi_j)^2} \qquad (4.32)$$

with

$$x_j(x_i, r_{int}) = \left\{ x \in X_2 \mid d(x_i, x_j) < r_{int} \right\} \qquad (4.33)$$

Once the distances are known, a weight

$$w(x_j) = \frac{1}{d(x_i, x_j)^P} \qquad (4.34)$$

is assigned to each point x_j lying within the interpolation radius around x_i. In the case of quadratic inverse distance weighting, the power is set to $P = 2$. Finally, the delay values Δ_i at the interpolated point x_i are obtained from the delays Δ_j that have to be interpolated by

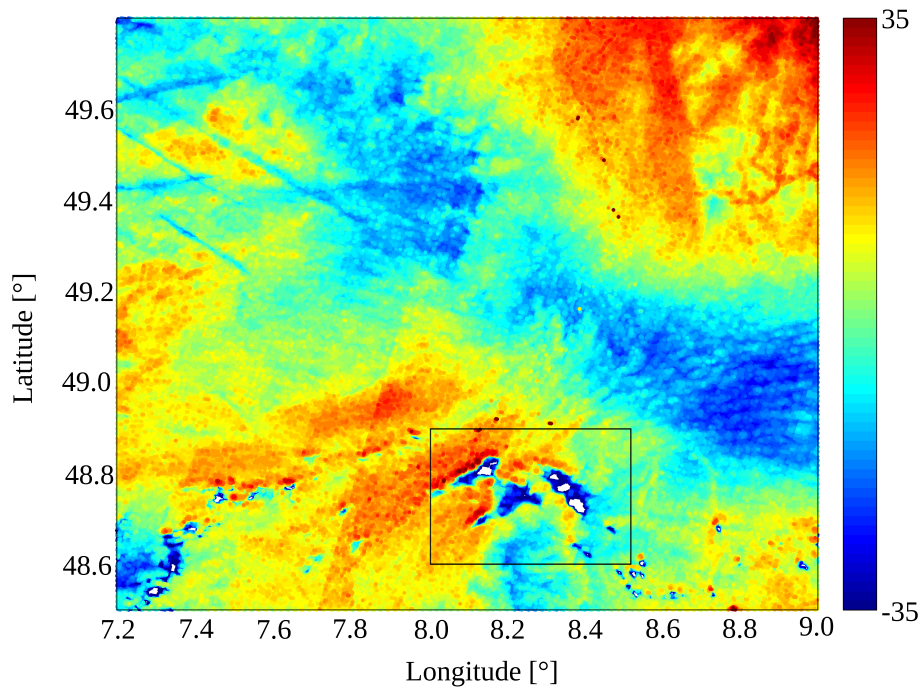$$\Delta_i = \sum_{j=0}^{N} \frac{w(x_j)}{\sum\limits_{j=0}^{N} w(x_j)} \cdot \Delta_j \qquad (4.35)$$

where N is the number of points x_j found within r_{int} around x_i.
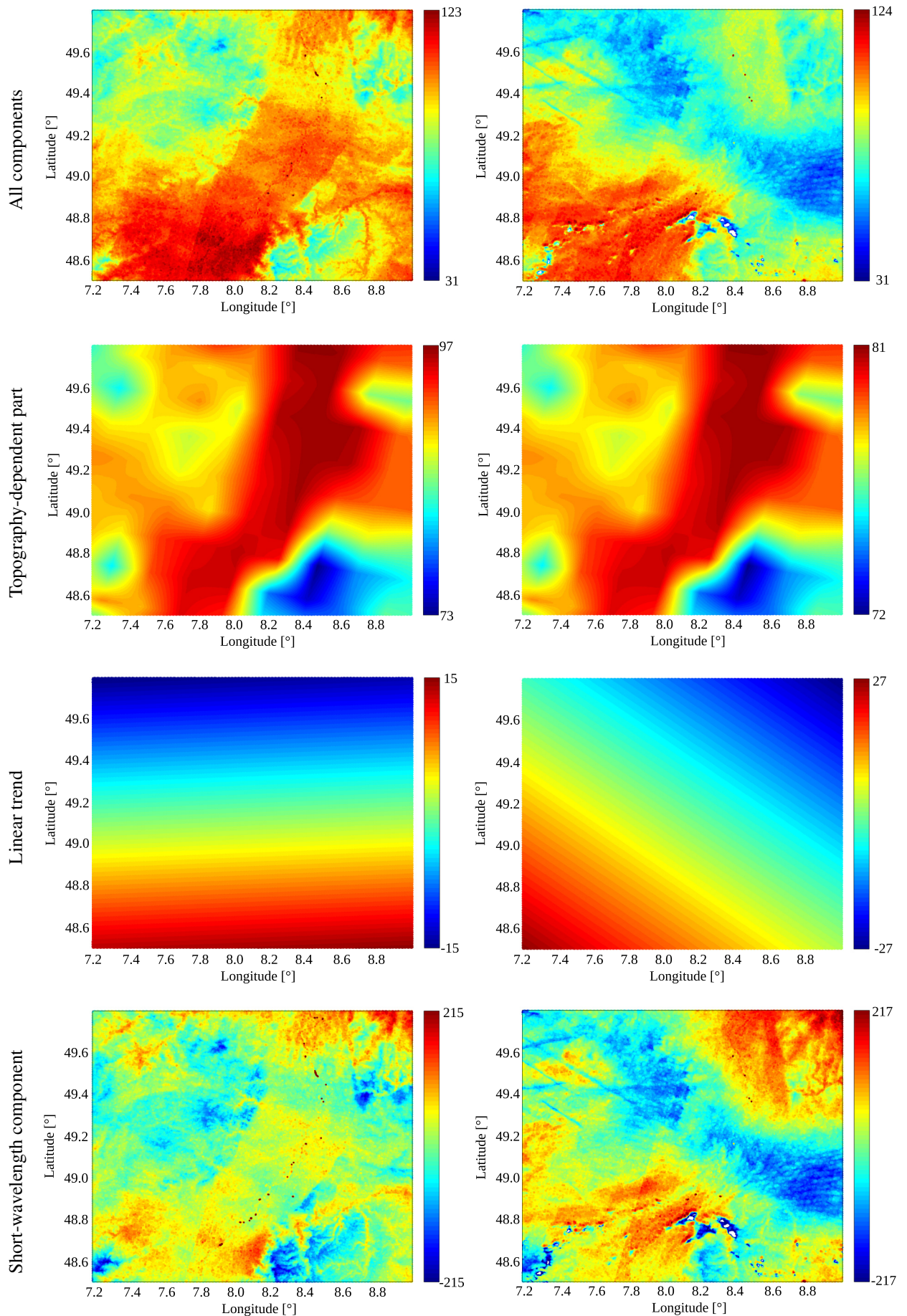
**Figure 4.5:** MERIS zenith wet delay components [mm]; left: 05-09-2005; right: 23-04-2007
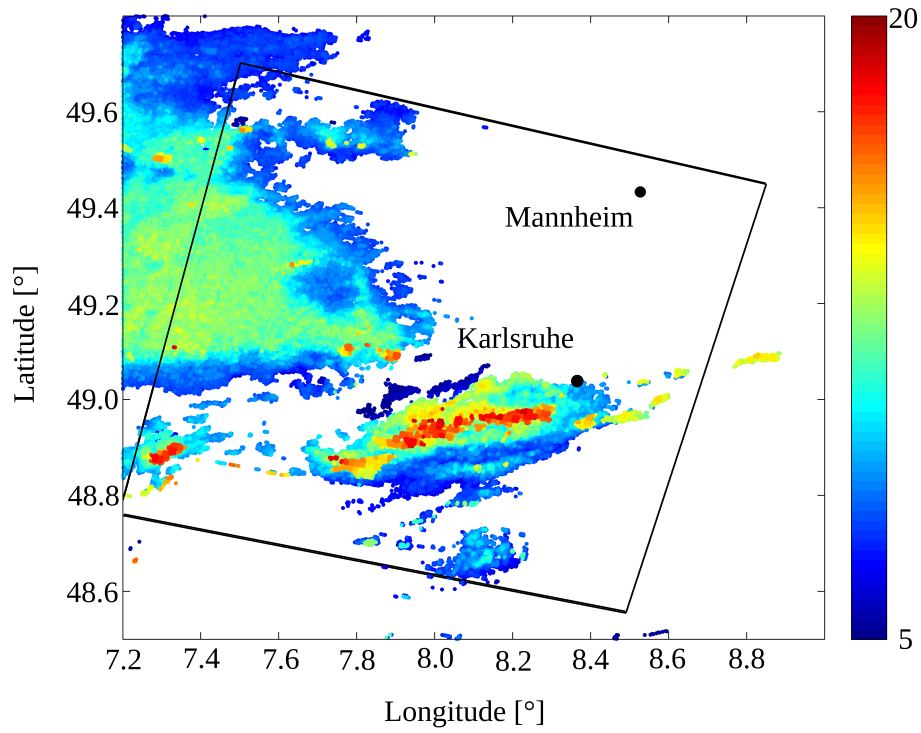
Figure 4.6: IWV from MERIS at acquisition 29-11-2004 [kg/m^2]; data gaps due to cloudy weather conditions

Figure 4.7: MERIS zenith wet delay of 23-04-2007 [mm]. The topography-dependent and linear trends are reduced. Due to clouds, data gaps occur within the rectangular.

In a further step, after the conversion from IWV values to delays, all those PS points lying within MERIS cells are searched and averaged within these cells. In this way comparable resolutions are obtained for both MERIS and InSAR. After this preparation, the delay values obtained from InSAR and MERIS can be compared with respect to different criteria. First, the standard deviations of the InSAR delays in Figure 4.8 were computed for each acquisition and with respect to each of the four master images. In 12 out of 17 cases, the standard deviations of the delays that were computed with reference to the master acquisition 29-11-2004 are the smallest ones. MERIS standard deviations were added to the plot. The standard deviations calculated from MERIS are larger than those deduced from InSAR. Since the reduced MERIS components are only approximated by means of simple linear models, the remaining components that are not contained in InSAR partial delays might cause these differences in the standard deviations.
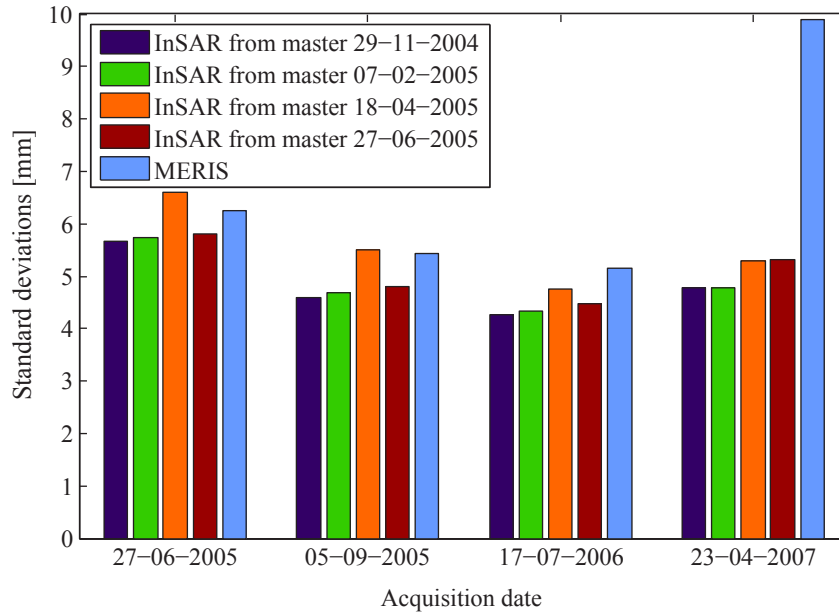
**Figure 4.8:** Comparison of InSAR and MERIS standard deviations

Besides the standard deviations, root mean square values of the difference maps MERIS − InSAR have been computed. Figure 4.9 illustrates that InSAR and MERIS agree best if the SAR acquisition 29-11-2004 is chosen as master. On 23-04-2007, the master 07-02-2005 yields the same root mean square value, but it has to be remembered that this master was not selected by means of the approach of Hooper et al. [2007]. Finally, the correlation coefficient R representing the dependence between the delays derived from InSAR and MERIS has been evaluated. It can attain values between $+1$ and -1. A total positive correlation corresponds to a value of $+1$, whereas 0 stands for no correlation:

$$R(InSAR, MERIS) = \frac{C(InSAR, MERIS)}{\sqrt{C(InSAR, InSAR) \cdot C(MERIS, MERIS)}} \tag{4.36}$$

where $C(InSAR, MERIS)$ is the covariance of the InSAR and MERIS delays and $C(InSAR, InSAR)$ and $C(MERIS, MERIS)$ stand for the variances of the InSAR and MERIS delays. Figure 4.10 gives the degree of correlation (in percent) between InSAR and MERIS delay maps for different master acquisitions.

Again, the acquisition 29-11-2004 leads to the highest correlation between the delays derived from InSAR and MERIS observations. As a consequence, the master 29-11-2004 seems likely to be a particularly good master acquisition. As illustrated in Figure 4.11, the maps obtained from InSAR and MERIS agree very well when choosing acquisition 29-11-2004 as master.

Against the expectation, the master selected based on the approach of Hooper et al. [2007], i.e., the acquisition 18-04-2005, does not show good results. The standard deviations of the delay maps computed with reference to this master are the worst. Also, the root mean square values are larger when using the acquisition of 18-04-2005
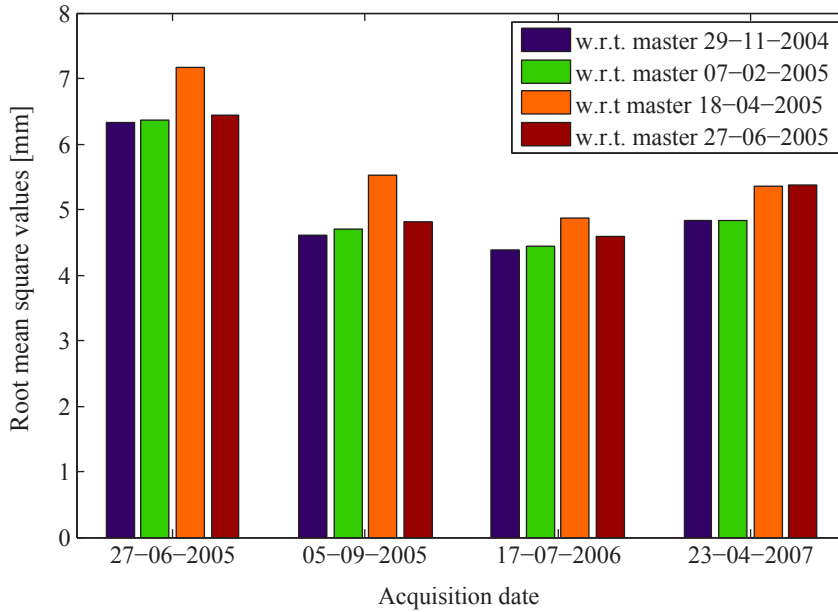
Figure 4.9: Root mean square values obtained from the difference maps MERIS − InSAR

as a master image. The degree of correlation also is the lowest when choosing 18-04-2005 as master, except for the last example (23-04-2007).

As visible in Figure 4.5, a particular neutrospheric pattern was observed on 23-04-2007. Strong short-wavelength variations appeared on this day. These variations are easily separated from the topography-dependent component as well as from the linear trend. Moreover, such a turbulent atmosphere can be clearly reconstructed by the inversion which is applied to obtain delays per acquisition from the SAR interferograms. As a consequence, the remaining short-wavelength components from MERIS and InSAR observations agree better on this date.

Altogether, it can be concluded that a master selection exclusively relying on the algorithm of Hooper et al. [2007] is not sufficient to obtain good results in neutrospheric modeling by means of InSAR. For this reason, section 4.3.4 presents a new, extended master selection approach.

4.3.4 Master selection criteria

The inversion used to obtain delay maps per acquisition from the interferograms, in section 4.3.1, is based on a zero-mean condition. It has been indicated that the small number of 17 available SAR acquisitions might have an impact on the results of the inversion. The comparisons with MERIS in section 4.3.3 give the idea that a master acquisition might be particularly good if it contains a smooth atmospheric signal without any turbulent activities.

For this reason, an enhanced master selection approach has been developed. It is schematically presented in Figure 4.12. The basic idea is to combine the master selection approach of Hooper et al. [2007] with additional external information. The aim is a minimization of the sum of decorrelation, i.e. a maximization of the total correlation $\sum_{i=1}^{N} \rho_{total}$. Though, due to the small number of SAR acquisitions within the analyzed stack, the inversion will be critical, especially in case of high neutrospheric activities during the master acquisition time. For this reason, the master atmosphere should be as smooth as possible. This can be explained as follows:

$$\Phi_{interferogram(j)} = \Phi_{master} - \Phi_{slave(j)} \tag{4.37}$$
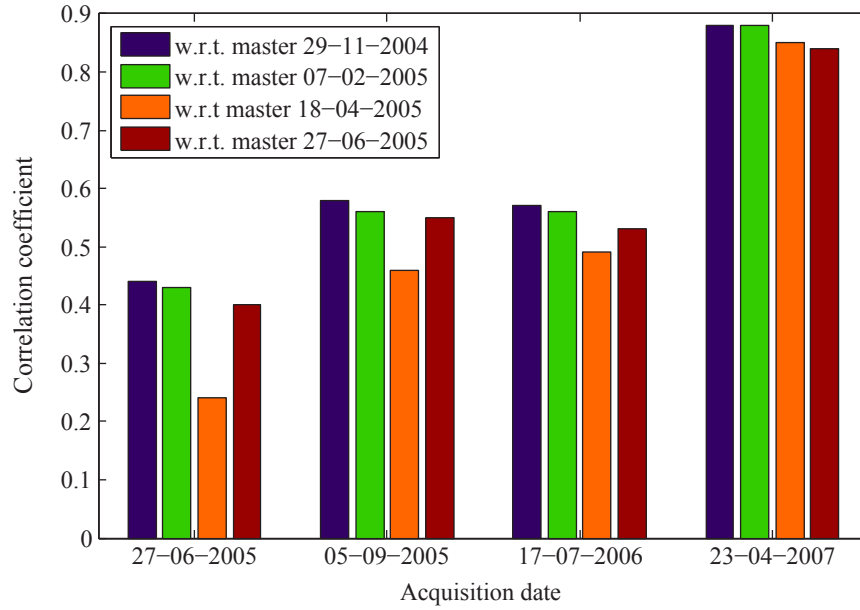
Figure 4.10: Degree of correlation of MERIS and InSAR with reference to different masters

An interferogram results from the difference of the master and the slave phase. If Φ_{master} is smooth, i.e., if the phase values of the master image vary hardly with respect to their mean, it can be approximated

$$\Phi_{interferogram(j)} \approx mean(\Phi_{master}) - \Phi_{slave(j)} \tag{4.38}$$

Then, the deduction of the neutrospheric phases of the slave from the interferometric phases is simple. Though, at any rate, if the interferogram formation is based on a smooth master atmosphere, the present turbulent patterns within the interferogram can be ascribed to the slave atmosphere, so this simplifies the interpretation of the results.

The smoothness of the four selected master acquisitions above has been analyzed in the previous chapter. Moreover, root mean square values with reference to MERIS observations as well as the correlation coefficients have been computed in order to decide which of the selected images represents the "best" master. This required processing the whole stack of SAR images with respect to the selected master candidates. These time-consuming pre-processing steps will be omitted, if the "best" master acquisition is determined by using external, i.e., data from GNSS or MERIS, as suggested in Figure 4.12.

However, there is no guarantee to obtain good MERIS observations without or only with few data gaps. This is why a comparison of MERIS and GNSS as in Lindenbergh et al. [2006] is useful. In their study, a correlation coefficient of 0.79 was obtained between the IWV deduced from GNSS and the surrounding MERIS IWV pixels situated within an appropriate interpolation radius of 1.75 km. If the water vapor observations of both sensors correspond to each other, the restricted availability of MERIS can be overcome by using only GNSS data for the master selection. Otherwise, other information sources are required (e.g., Sentinel-3, NWM).

In the following, histograms of the delays and meteorological measurements are two more criteria for the neutrospheric activity. It is also shown that, even in case of large data gaps, absolute IWV values within MERIS observations could be indicators for the neutrospheric activity. The smoothness of the atmosphere can be described by analyzing histograms of the observed delays. In case of a smooth atmosphere, the delays should follow a Gaussian distribution. However, turbulent atmospheres as that of 23-04-2007 shown in Figure 4.11 may deviate clearly from normality as can be seen in Figure 4.13.

Moreover, meteorological information can be used to estimate whether the observed atmosphere is rather turbulent or calm. Central-European climate is typically characterized by cold, dry winters and warm, wet summers. As
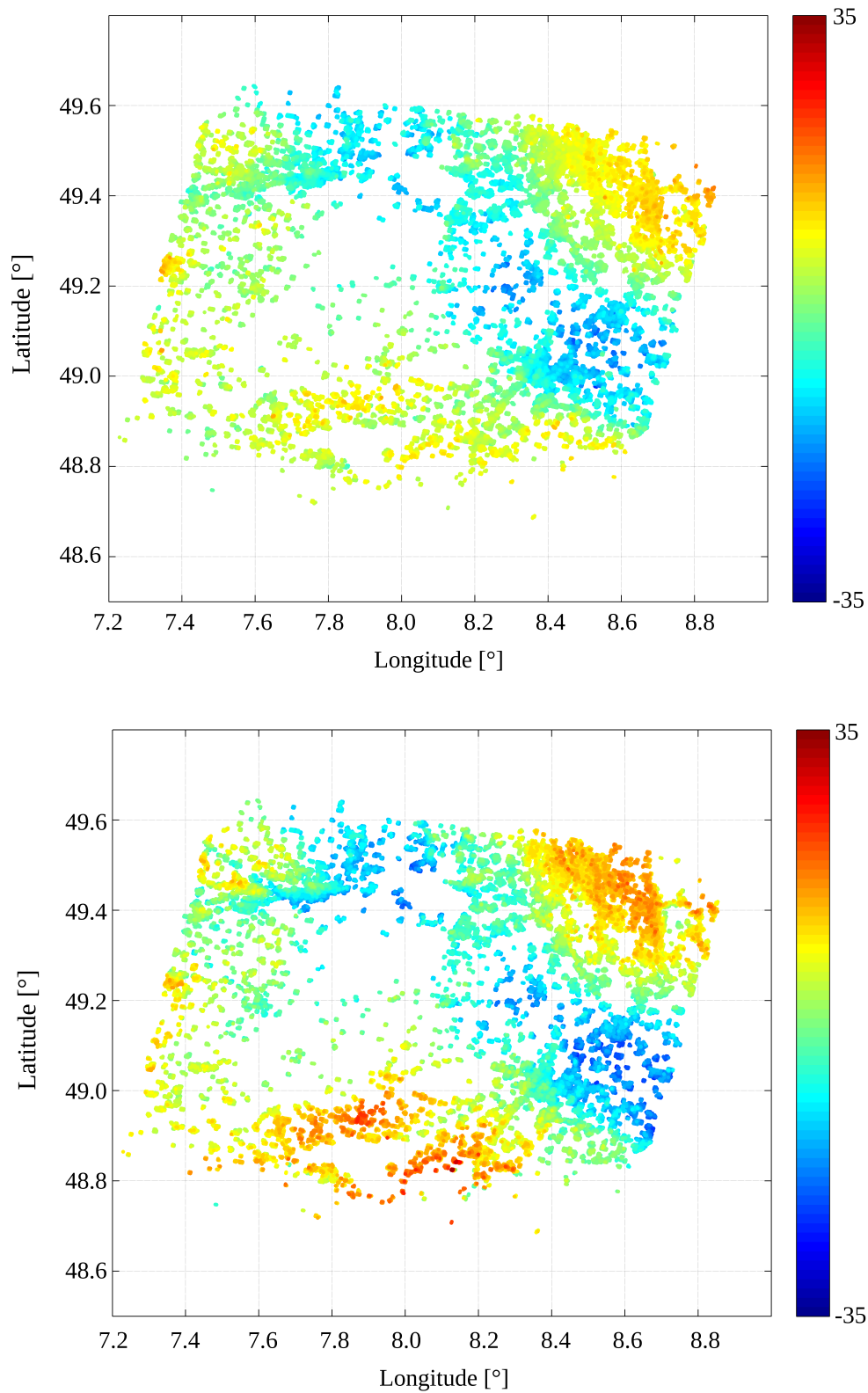
Figure 4.11: Turbulent atmosphere: upper: partial zenith wet delays [mm] of acquisition 23-04-2007 from InSAR (w.r.t. master 29-11-2004); lower: partial zenith wet delays [mm] of acquisition 23-04-2007 from MERIS observations
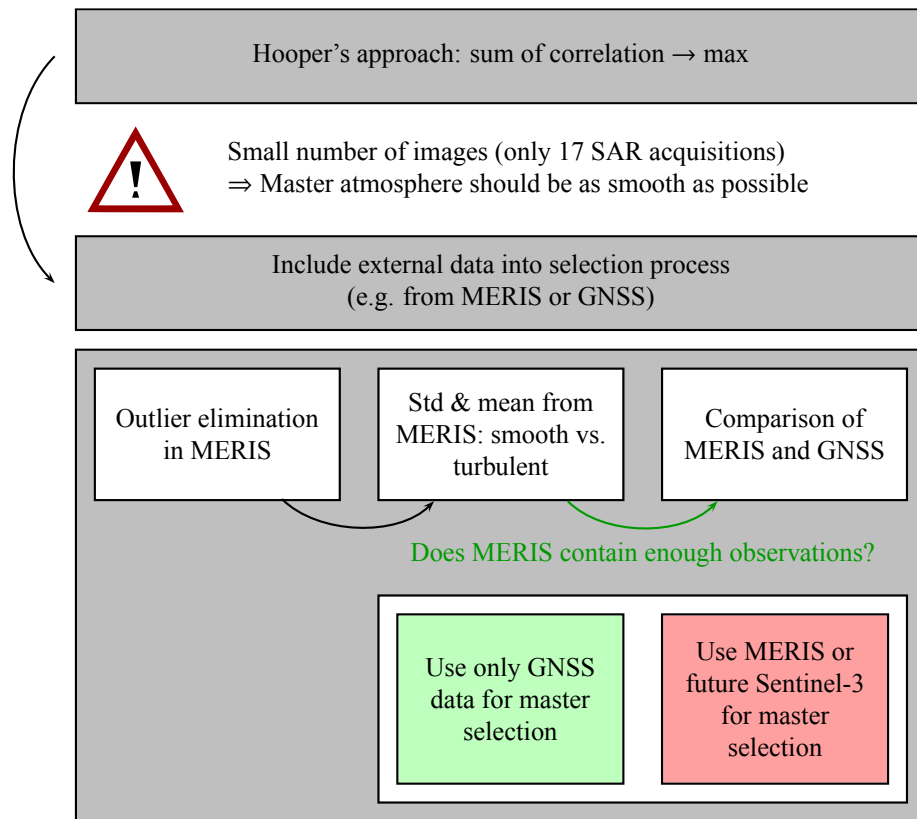
Figure 4.12: Flowchart representing the enhanced master selection approach developed for atmospheric applications of InSAR
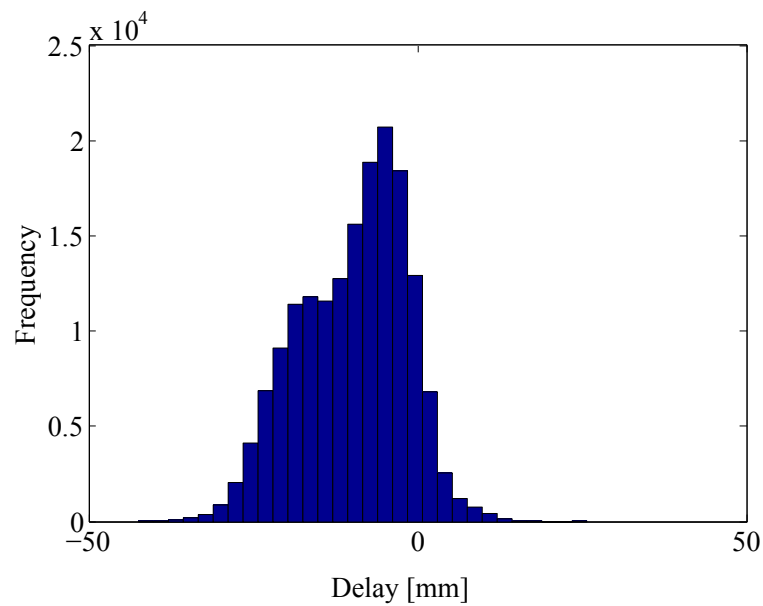
Figure 4.13: Histogram of the delays of acquisition 23-04-2007 referred to master 29-11-2004: Delay distribution within a turbulent atmosphere

the master 18-04-2005 yields worse results than the master 29-11-2004 in section 4.3.3, the temperatures and partial pressures of water vapor occuring on the days around these two acquisition dates have been analyzed. Figure 4.14 compares the partial pressure of water vapor and the temperature on 29-11-2004 and 18-04-2005 at the meteorological observing site Karlsruhe. In both cases, two days before and two days after the SAR acquisition are shown and the acquisition time is highlighted. It can be seen that the daily temperature differences in November are smaller than those in April. Furthermore, the partial pressure of water vapor seems to be more variable in the considered days in April than within the time interval in November. These findings might be an indicator for a more active atmosphere in April. However, this should be analyzed in more details to get information about the atmospheric activity.
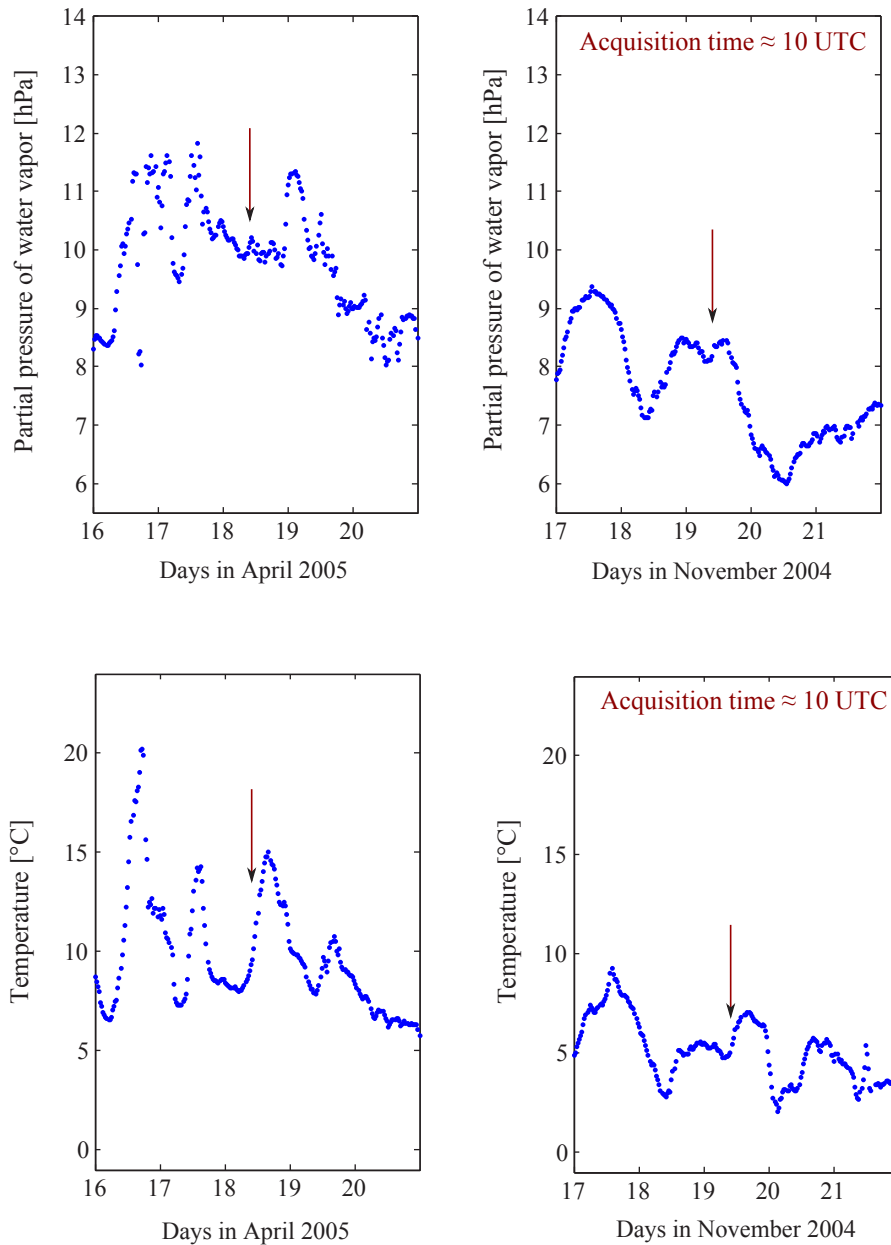

Figure 4.14: First row: Partial pressure of water vapor at the meteorological observing site Karlsruhe; Second row: Temperatures at the meteorological observing site Karlsruhe

Finally, MERIS acquisitions can be examined. Even in case of large data gaps as in the case of the two different master acquisitions on 29-11-2004 and 18-04-2005 shown in Figure 4.15 and Figure 4.16, MERIS provides a certain insight into the atmospheric activity.

At both dates, there were many clouds that made the observation of IWV underestimated in large parts of the MERIS acquisition. Though, clouds usually are composed by droplets of liquid water or small ice cristals and therefore do not directly indicate a high amount of water vapor. Independently on the cloud coverage, the water vapor measured in the regions in which data are available is apparently much higher on 18-04-2005 than on 29-11-2004.
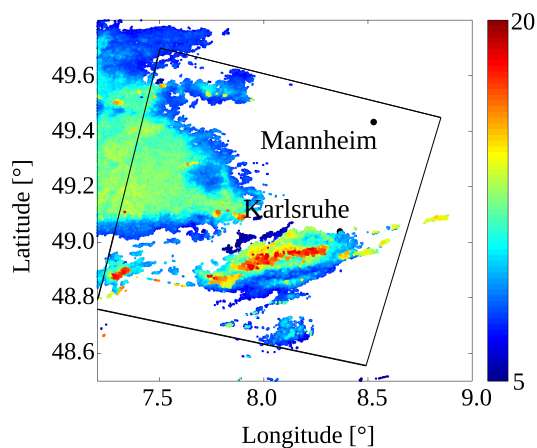
Figure 4.15: IWV observations in kgm^{-2} from MERIS on 29-11-2004
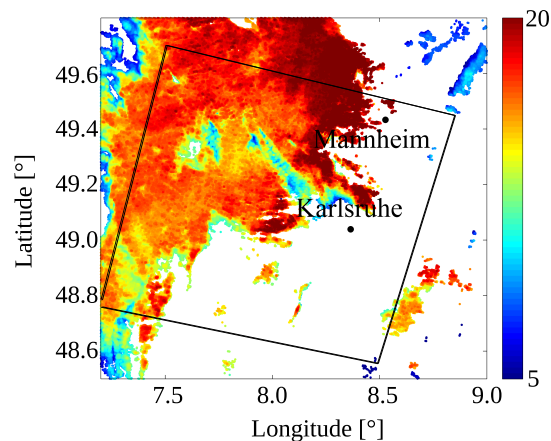
Figure 4.16: IWV observations in kgm^{-2} from MERIS on 18-04-2005

As a conclusion, the atmospheric activity appears to be higher during the acquisition in April than during that in November, and hence, the analysis of MERIS acquisitions might also already provide useful information for the selection of the master that might be the best in terms of the smoothness of the atmosphere.

4.4 Summary

In this chapter, the extraction of neutrospheric maps based on PS InSAR observations was described. MERIS measurements of the IWV were transformed into partial zenith wet delays after subtracting a topography-dependent component and a linear trend. A correlation of up to 88% was attained between the resulting partial zenith wet delays from MERIS and corresponding delays per acquisition obtained after inversion of the InSAR observations. The atmospheric smoothness of four different master acquisitions was comparatively analyzed. Particularly smooth atmospheric patterns turned out to be the best master candidate with respect to an inversion based on a small stack of only 17 SAR acquisitions. As the separation of the master and the slave atmosphere is less complex in case of a smooth master atmosphere, an enhanced master selection algorithm extending the approach of Hooper et al. [2007] was presented. This algorithm aims at including external information on the atmospheric status into the master selection.

5 Comparison of the wet delays from GNSS and InSAR data

Within this section, the main focus is on the joint exploitation of wet delays in InSAR and GNSS. When aiming at a rigorous comparison of GNSS and InSAR data, attention has to be paid to the different viewing geometries of these two sensors, analyzed in the two previous chapters. After a comparison of the observation scenarios of GNSS and InSAR, GNSS satellites in the topocentric direction of the SAR are searched. Then, the wet delay contained in the GNSS and InSAR observations is compared.

5.1 Comparison of the observing geometries of GNSS and InSAR

Figure 5.1 shows the differences in the observation scenarios of GNSS and InSAR propagating into the wet delay estimates of these sensors. GNSS yield pointwise measurements averaged over a cone above the receiver and defined by the minimum elevation angle ε_{min}. One single zenith delay value is computed from the observations from all visible satellites within a specific time window. Here, the spatial resolution is restricted by the distances between the respective GNSS sites. In contrast, the temporal resolution is very high (30 s for an analysis taking into account residuals) and each determined delay value refers to one single time instant within the sampling.
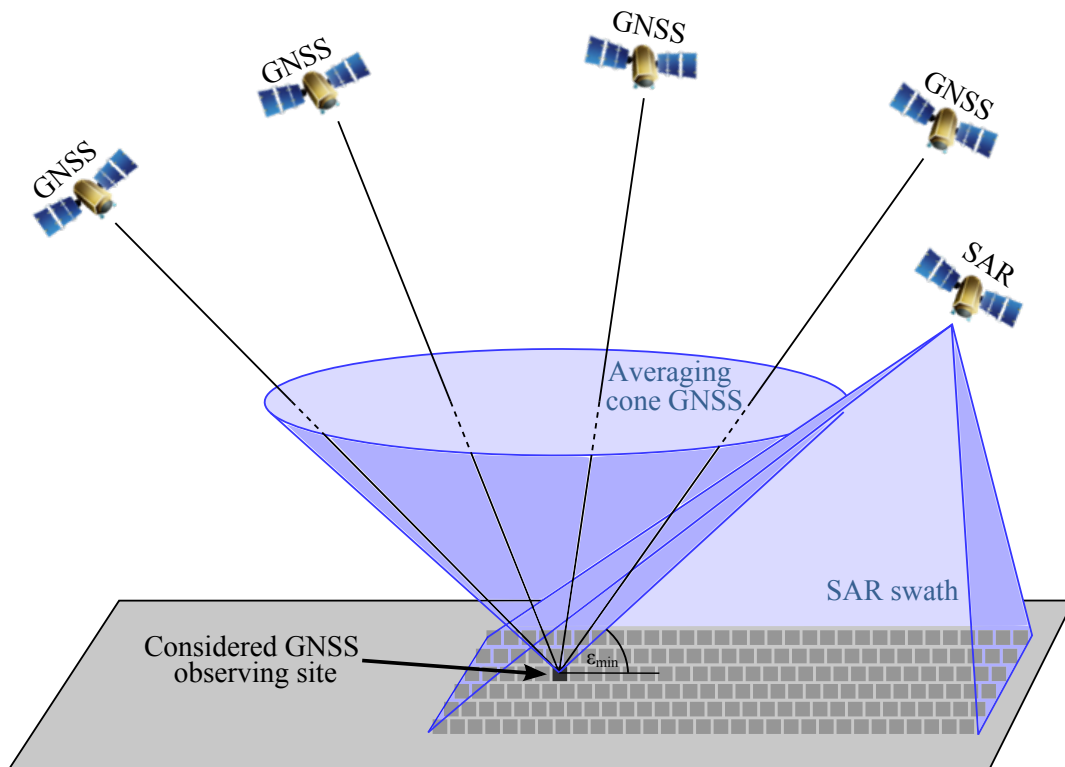
Figure 5.1: Schema of the comparison w.r.t. the different viewing geometries of GNSS and InSAR

In contrast to GNSS, a SAR sensor observes images. From two of these SAR acquisitions, interferograms can be deduced. Hence, InSAR provides spatially much higher resolved data than GNSS. Though, these measurements do not correspond to a single date but represent the differences between the scenes at two overpass times. This already implies that their temporal resolution is considerably lower than that of the GNSS observations. Due to the 35-day repeat cycle of the Envisat orbit, only ten acquisitions per year are possible, which results in a maximum of nine interferograms per year, if they are computed with respect to one single master acquisition. The delays are determined based on the interferometric phases observed along the line-of-sight of the SAR. Figure 5.1 shows only schematically the differences in the viewing geometry. In reality, the GNSS satellites fly in much higher orbits (about 20000 km orbital height) with respect to the SAR satellite (about 800 km orbital height). In addition, both sensors do not cover identical parts of the atmosphere.

5.2 Finding GNSS satellites in the direction of the SAR satellite

While Envisat is a single satellite flying always within a single orbit, at least 24 GPS satellites arranged within six equally-spaced orbital planes (e.g., inclination: 55°, repeat time: 11h 58min) were in space in 2005. Moreover, visible GPS satellites can be observed from a GNSS receiver at any time of the day. The satellite constellation changes within a day and from day to day, which results in different viewing geometries. In contrast, when flying over, the ASAR acquires only one image. Within the processed SAR stack, the acquisitions started between 9:51:13 and 9:51:30 UTC and the acquisition time equaled 28 s in each case.

GPS orbit information, i.e. azimuth and elevation angles of the GPS satellites detected at the respective observing sites, are available within the residual files with the file extension *.FRS calculated by the Bernese software based on accurate IGS orbits. For this reason, the SAR orbits have been transformed from the Earth Centered Earth Fixed (ECEF) Cartesian coordinates X_{SAR}, Y_{SAR}, and Z_{SAR}, given with reference to the WGS84 ellipsoid, to values of the local azimuth and elevation of the considered GNSS site. According to Bauer [2011] and Hofmann-Wellenhof et al. [2001], WGS84 agrees with the International Terrestrial Reference Frame ITRF2005 in the order of 1 cm. The conversion to azimuth and elevation is done in three steps. First, the ECEF Cartesian WGS84 coordinates X_{site}, Y_{site}, and Z_{site} of the considered observing site are iteratively transformed into ellipsoidal coordinates λ_{site}, φ_{site}, and H_{site} based on Heck [2003]. In the second step, the difference vector

$$\Delta \vec{x} = \vec{X}_{SAR} - \vec{X}_{site} = \begin{pmatrix} X_{SAR} \\ Y_{SAR} \\ Z_{SAR} \end{pmatrix} - \begin{pmatrix} X_{site} \\ Y_{site} \\ Z_{site} \end{pmatrix} = \begin{pmatrix} \Delta x \\ \Delta y \\ \Delta z \end{pmatrix} \tag{5.1}$$

is transformed to $\vec{x}' = (\Delta x', \Delta y', \Delta z')$. This is done by

$$\vec{x}' = R \cdot \vec{x} \tag{5.2}$$

with the rotation matrix R

$$R = \begin{pmatrix} -\sin \varphi_{site} \cdot \cos \lambda_{site} & -\sin \varphi_{site} \cdot \sin \lambda_{site} & \cos \varphi_{site} \\ -\sin \lambda_{site} & \cos \lambda_{site} & 0 \\ \cos \varphi_{site} \cdot \cos \lambda_{site} & \cos \varphi_{site} \cdot \sin \lambda_{site} & \sin \varphi_{site} \end{pmatrix} \tag{5.3}$$

In the third step, the local elevation ε and azimuth A of the considered satellite follow with respect to the selected observing site:

$$\varepsilon = \arcsin \left(\frac{\Delta z'}{D} \right) \tag{5.4}$$

$$A = \arctan \left(\frac{\Delta y'}{\Delta x'} \right) \tag{5.5}$$

Here, the length D of the vector $\vec{x}'$ is computed by

$$D = \sqrt{\Delta x'^2 + \Delta y'^2 + \Delta z'^2} = |\Delta \vec{x}'| \tag{5.6}$$

Additionally, to obtain equal orbit information from InSAR and GPS, a time shift has to be applied. The azimuth and elevation angles of the GPS satellites are computed per epoch, i.e. every 30 s. Here, however, they are not given in the Coordinated Universal Time (UTC), but in GPS time. On January 5, 1980, at 24:00:00, both systems corresponded to each other. According to Prasad and Ruggieri [2005] and Bauer [2011], the differences between GPS time and UTC have accumulated since then with each integer leap second that had been added in order to match Earth rotation. In 2005, the difference between the two time systems (GPS − UTC) equaled 13 s. These 13 s are added to the InSAR orbits given in UTC to enable a rigorous comparison in GPS time.

Based on these preparations, GPS satellites in the direction of the SAR can be searched in order to enable a rigorous comparison of the neutrospheric delays deduced from both sensors within this direction. Figure 5.2 shows how much the elevation of the GPS satellites deviates from the elevation of the SAR during its acquisition time.
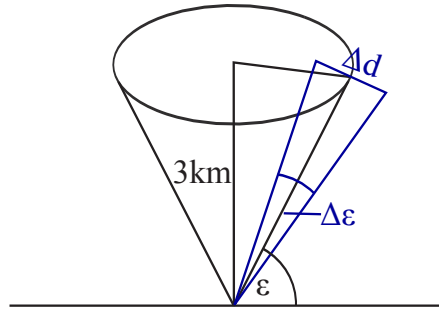
Figure 5.2: Change of the line-of-sight to the GPS satellite due to a change in the satellite's elevation

If the elevation ε of the GPS satellite changes by $\Delta\varepsilon/2$, the piercing point of the line-of-sight from the receiver to the satellite with an atmospheric layer of 3 km resp. 1 km height above the surface moves by $\Delta d/2$ resp. $\Delta d'/2$. The following approximation should hold:

$$\frac{\Delta d}{3 \text{ km}} \approx \Delta\varepsilon \text{ [rad]} \qquad \text{resp.} \qquad \frac{\Delta d'}{1 \text{ km}} \approx \Delta\varepsilon \text{ [rad]} \tag{5.7}$$

For a maximum accepted change in distance $\Delta d_{max} = 1500$ m, it follows in degree

$$\Delta\varepsilon_{max} \approx 29° \tag{5.8}$$

This tolerated change in the elevation angle is obtained, if a change in distance by $\Delta d'_{max} = 500$ m is accepted at a height of 1 km above the surface. Consequently, all those GPS satellites of elevations deviating less than $\Delta\varepsilon_{max}/2 = 14.5°$ from the mean elevation $\varepsilon_{SAR\ mean\ acq_i}$ of the SAR satellite at acquisition i could be considered as "close" satellites, i.e.,

$$\varepsilon_{SAR\ mean\ acq_i} = \frac{1}{2} \cdot \left(\varepsilon_{SAR\ max\ acq_i} + \varepsilon_{SAR\ min\ acq_i} \right) \tag{5.9}$$

In this case, the difference in elevation between two arbitrary GPS satellites classified as "close" would never exceed the threshold value of $\Delta\varepsilon_{max} = 29°$, which corresponds to an accepted change in distance of 1500 m at 3 km height or to a deviation of 500 m at 1 km height. The height of 3 km has been initially selected for this estimation because Rocken et al. [1997] assume that most of the atmospheric water vapor is concentrated within the lowest 3 km of the Earth's atmosphere. If, at this height, the GPS signal direction deviates more than 750 m from the elevation of the SAR, the satellite is considered as too far to observe comparable neutrospheric characteristics. Alshawaf [2013] rather supposed water vapor to be concentrated in the lowest kilometer of the atmosphere, which turns out to be reasonable when considering the averaging regions for the InSAR observations below.

However, the elevation of the Envisat during the acquisition time varies from acquisition to acquisition. If the threshold value of $14.5°$ is now subtracted from or added to the respective mean SAR elevation $\varepsilon_{SAR\ mean\ acq_i}$, it is not accounted for the variation in the change of elevation. Hence, the maximum allowed elevation difference between the GPS and the SAR, would change for each acquisition time. If the SAR elevation change equals $7°$, a maximum deviation of the GPS elevation from the mean SAR elevation of $14.5° - 7°/2 = 11°$ would be accepted. In contrast, a SAR elevation change of $1°$ would yield deviations up to $14.5° - 1°/2 = 14°$. The search region for "close" satellites would also change its size for different acquisition times.

To avoid this drawback, an alternative approach was chosen for the following analysis. Instead of the difference with respect to the mean elevation, the deviation from the minimum or maximum elevation of the SAR at the respective acquisition is analyzed. As detailed below, this point of view can easily be adapted to the restriction of the accepted azimuth angles. In this way, by adding or subtracting the threshold $\Delta\varepsilon_{max}/2$ to the maximum SAR elevation, a searching window slightly bigger than $\Delta\varepsilon_{max} = 29°$ might be obtained. For this reason, the maximum allowed deviation in elevation is reduced from $\Delta\varepsilon_{max}/2 = 14.5°$ to

$$\Delta\varepsilon_{search} = \frac{1}{2} \cdot \Delta\varepsilon_{max} - \frac{1}{2} \cdot max\left(\Delta\varepsilon_{SAR}\right) \tag{5.10}$$

where $max\left(\Delta\varepsilon_{SAR}\right)$ is the maximum SAR elevation change observed within the available SAR acquisitions. In this way, it is assured that the difference in elevation does not exceed the threshold $\Delta\varepsilon_{max}$ for any combination of two GPS satellites declared as "close".

Thus, a GPS satellite is declared as "close" to the SAR, if

$$\varepsilon_{SAR\ min\ acq_i} - \Delta\varepsilon_{search} < \varepsilon_{GPS} < \varepsilon_{SAR\ max\ acq_i} + \Delta\varepsilon_{search} \tag{5.11}$$

holds for this satellite, and if (5.12) is valid:

$$\Delta A_{SAR\ min\ acq_i} - \Delta A_{search} < A_{GPS} < \Delta A_{SAR\ max\ acq_i} + \Delta A_{search} \tag{5.12}$$

with

$$\Delta A_{search} = \Delta\varepsilon_{search} \tag{5.13}$$

Here, $A_{SAR\ max\ acq_i}$ and $A_{SAR\ min\ acq_i}$ represent the maximum and minimum SAR azimuth angle observed during the considered acquisition, and the temporal search window has been restricted to one minute, i.e. to the two closest epochs to the SAR acquisition time.

Due to the big change in azimuth observed during the SAR acquisition, the search window in azimuth is much less restraining than that in elevation. Depending on the observing site, the azimuth varies more or less, but at all sites the change observed in azimuth is much larger than that in elevation. It reaches up to $62°$ at the site Geislingen (0391), whereas the maximum change in elevation during a SAR acquisition equals $7°$ for the selected ten observing sites. Compared to this value, the change in azimuth is enormous. However, azimuth angles do not directly represent a distance covered by the satellite. As a simple example, a satellite flying in North-South direction over a site is imagined. As long as the satellite is viewed in the north of the site its elevation might increase and the azimuth angle will stay constant at $0°$. When the zenith (an elevation of $90°$) is passed through, the satellite suddenly appears on the southern side of the observing site and the azimuth changes to $180°$. Hence, without covering a large distance with the satellite, a difference in the azimuth angle of $180°$ is observed. Large azimuth changes are therefore possible within the short acquisition time of the ASAR sensor. Of course, this example does not represent reality. Envisat did neither fly in North-South direction, nor was it observed in the zenith. However, due to its high orbit inclination of $98.55°$, the descriptive showcase is helpful for the understanding of the observed changes in azimuth during the SAR acquisition.

In any case, an azimuthal symmetry is assumed during the estimation of the SSNP. The computed site-specific neutrosphere parameters correspond to an average of all those observations falling within a cone with a height of 3 km resp. 1 km (depending on the statements of Rocken et al. [1997] and Alshawaf [2013]) and an opening angle

depending on the minimum elevation introduced into the analysis. Here, ε_{min} has been set to $3°$ and $H = 1$ km, then

$$r_{cone} = \tan(90° - \varepsilon_{min}) \cdot H\,[\mathrm{km}]$$ (5.14)

in a cone with a diameter of about 38 km illustrated in Figure 5.3. The GPS satellite's azimuth angle only is of importance when considering the residuals that are expressed within the slant direction from the receiver to the satellite.
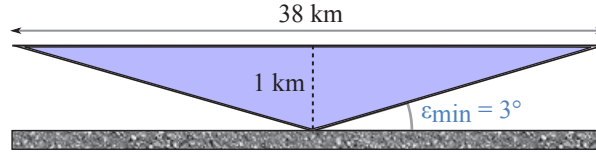
Figure 5.3: Averaging cone for SSNP at a minimum elevation of $3°$

Based on the estimation of (5.14), the InSAR observations are averaged over a 38 km × 38 km large rectangular area on the ground in order to compare them with the GPS measurements composed of the SSNP averaged within a cone around the GNSS site. Considering Figure 5.4, an averaging over even larger areas is definitely not recommended.

According to Wanninger [2000], the height of the considered observing site does not significantly influence the elevation angle at which the GPS satellite is viewed. An iterative approach is used to compute the difference in elevation caused by a difference in height:

$$\varepsilon_B = \varepsilon_A + \arcsin\left(\frac{r_e}{r_s} \cdot \cos\varepsilon_A\right) - \arcsin\left(\frac{r_e + \Delta H_{AB}}{r_s} \cdot \cos\varepsilon_B\right)$$ (5.15)

with

ε_A elevation at height H_A
ε_B elevation at height H_B
ΔH_{AB} difference in height $H_A - H_B$

and

$r_e = 6371$ km   "radius" of the Earth
$r_{s\ GNSS} = r_e + 20200$ km   "radius" of the GNSS satellites' orbits
$r_{s\ SAR} = r_e + 800$ km   "radius" of the SAR satellite's orbit

A difference in height of $\Delta H_{AB} = 1000$ m then results in a difference in elevation of $0.002°$ (in the case of GNSS) or $0.038°$ (in the case of SAR). As a consequence, the height of the observing site does not have any significant effects on whether or not a GPS satellite is found in the direction of the SAR.

In this work, GPS satellites "close" to the SAR are found at each of the four observing sites lying within the SAR frame. The averaging area of 38 km × 38 km is specified in Figure 5.4 that shows the interferograms deduced from the slaves 03-01-2005 and 23-05-2005 with reference to master 27-06-2005.

The azimuth-elevation diagram in Figure 5.5 shows that many satellites traverse the spatial search windows colored in blue. Yet, the temporal constraint selected in order to observe the "same" atmospheric characteristics as the SAR severely reduces the number of "close" satellites that can be found.
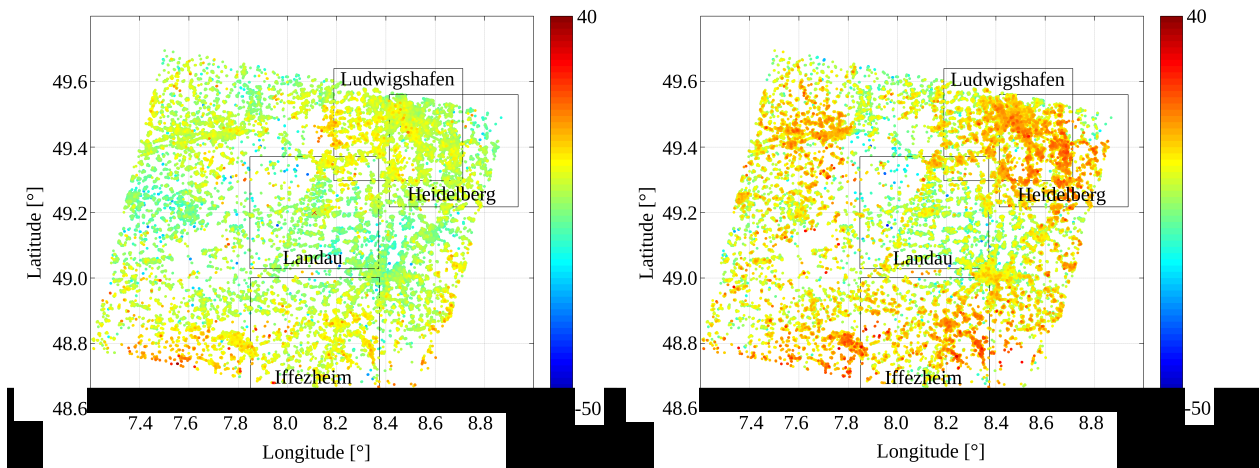
Figure 5.4: Partial wet delays [mm] from InSAR and averaging regions around the observing sites from which close GPS satellites are observed; left: master 27-06-2005, slave 03-01-2005; right: master 27-06-2005, slave 23-05-2005
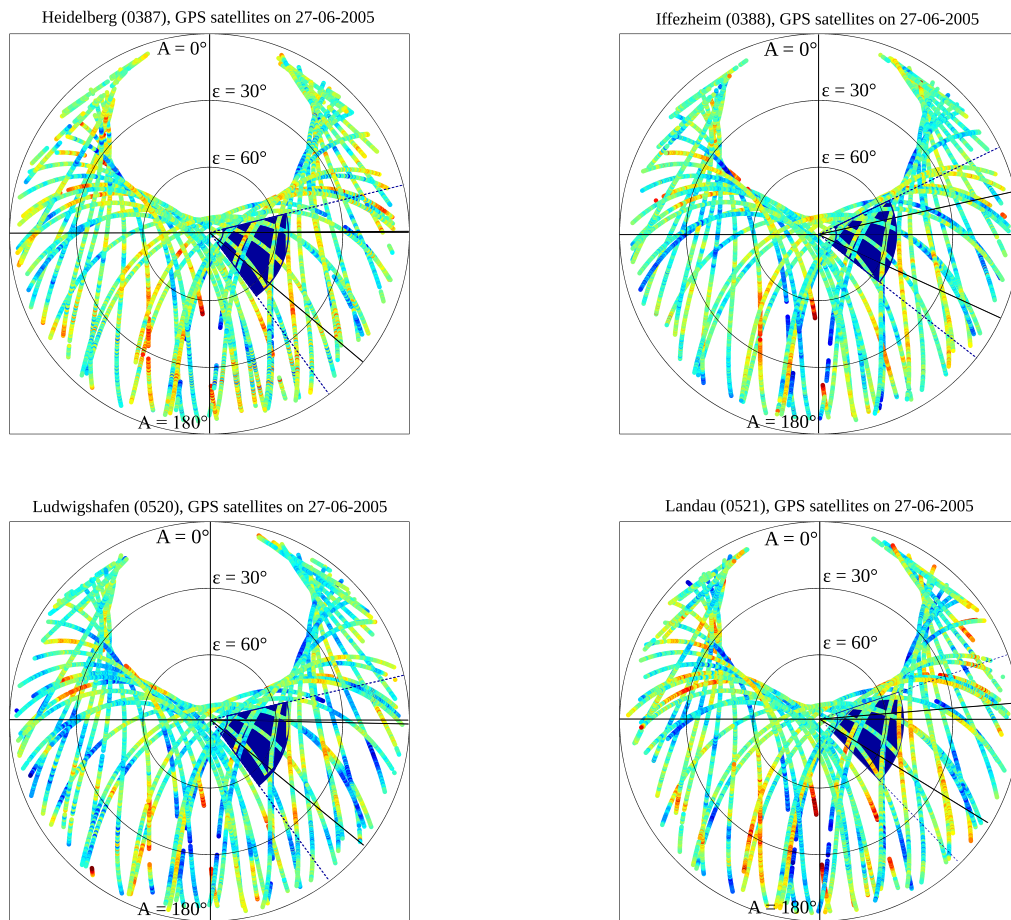
Figure 5.5: Azimuth-elevation diagram of the GPS satellites on 27-06-2005; spatial search window in blue

5.3 Contributions of GNSS and InSAR to the wet delay

In section 4.3.2, MERIS observations were converted into partial wet delays with the aim of obtaining comparable quantities from both MERIS and InSAR acquisitions. In the section thereafter, these partial wet delays deduced from MERIS are compared to delays per acquisition derived from InSAR phase observations as described in section 4.3.1. An essential finding of these two chapters is the partial nature of the InSAR delays. According to Alshawaf [2013], dry delays are commonly supposed to show a repeatable behavior. Due to their vertical stratification, their effect is largely removed during the interferogram formation. However, a SAR interferogram represents the difference of the total wet delay values from the master and the slave images. Therefore, two main components of this wet delay are already missing. Hereafter, similar to the notations of the MERIS components in section 4.3.2, they shall be denoted as the topography-dependent part and a linear trend. The topography-dependent part cancels out when forming the interferograms or reducing the topographic phase and related topography-dependent errors. The linear trend cannot be separated from the orbit ramps and is removed with them. For this reason, the contribution of InSAR to the wet delay is not at all the same as that of GNSS observations in PPP mode.

In contrast to InSAR, PPP measures the absolute neutrospheric delay composed of a dry and a wet component as introduced in section 2.2. If the computations in Bernese are based on the model of Saastamoinen for the estimation of the dry component, it can again be assumed that this dry part of the delay is removed when subtracting the observations of the master and the slave date. This is the case when using the option DRY_NIELL for the a priori model in Bernese. For this reason, the following analysis is based on this mapping function and this a priori model. For the wet component, the option WET_NIELL has been selected in the Bernese software. As the a priori model MOD_U from the Bernese *.TRP file cancels out, the considered contributions of GNSS to the wet delay are

- SSNP in zenith direction (CORR_U in Bernese)

- horizontal gradients in Northing and Easting (CORR_N and CORR_E in Bernese), and the

- real residuals converted to L1, referring to the line-of-sight between the receiver and the satellite.

Figure 5.6 illustrates the differential wet delay components from GNSS as well as the differential wet delays deduced from InSAR. The standard deviations of these InSAR delays are also plotted.

The influence of the horizontal gradients, computed based on observations down to $3°$, is negligible at the considered elevation angles of $\varepsilon > 66°$. The smaller the elevation, the higher the effect of the atmospheric tilting becomes. As introduced in (3.16), the effect of the horizontal gradients in Northing (effect_$\Delta^{N, slant}$) and Easting (effect_$\Delta^{E, slant}$) on the slant wet delay from GNSS is expressed by

$$
\begin{aligned}
\text{effect\_}\Delta^{N, slant} &= \Delta^N \cdot \frac{\partial mf_{wet}}{\partial \varepsilon} \cdot \cos A \\
\text{effect\_}\Delta^{E, slant} &= \Delta^E \cdot \frac{\partial mf_{wet}}{\partial \varepsilon} \cdot \sin A
\end{aligned}
\tag{5.16}
$$

Setting mf_{wet} to $\cos z$ and applying $z = 90° - \varepsilon$ it can be written

$$
\begin{aligned}
\text{effect\_}\Delta^{N, slant} &= -\Delta^N \cdot \cos \varepsilon \cdot \cos A \\
\text{effect\_}\Delta^{E, slant} &= -\Delta^E \cdot \cos \varepsilon \cdot \sin A
\end{aligned}
\tag{5.17}
$$

Knowing that $\varepsilon \in [0°, 90°]$ yields $\cos \varepsilon \in [0, 1]$. Consequently, the largest effect of the horizontal gradients on the observed wet delay occurs in case of

$$
\cos \varepsilon = 1 \qquad \Leftrightarrow \qquad \varepsilon = 0°
\tag{5.18}
$$

For higher elevations, the effects decrease with the cosine of the elevation angle. The worst case of $\varepsilon = 0°$ results in an effect of the horizontal gradients of

$$
\begin{aligned}
\text{effect\_}\Delta^{N, slant} &= -\Delta^N \cdot \cos A \\
\text{effect\_}\Delta^{E, slant} &= -\Delta^E \cdot \sin A
\end{aligned}
\tag{5.19}
$$
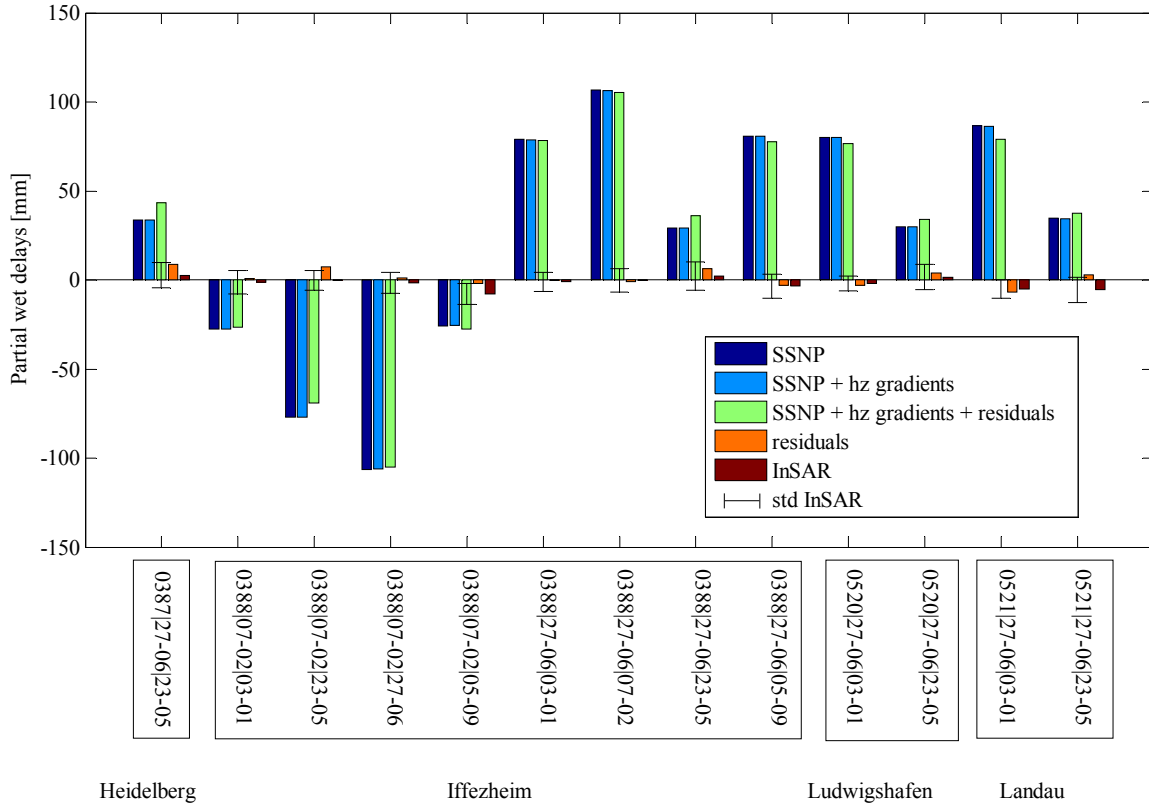
Figure 5.6: Comparison of differential components of the wet delay deduced from GNSS and differential wet delays derived from InSAR

Due to the SAR satellite appearing in the East during the acquisition time, it is easy to predict that the pure horizontal gradients in Northing do not have an important influence on our study. These gradients cause a tilting of the atmospheric layer in the direction North-South, whereas the gradients in Easting tilt the atmosphere in the direction East-West. As a consequence, the effect of the horizontal gradients in the Easting direction is larger, even though their absolute mean values over the year in the considered region are slightly smaller than those in Northing. The mean horizontal gradients observed in 2005 at the four considered observing sites equal

$$\begin{aligned} \Delta^N_{mean} &= -0.39 \text{ mm} \\ \Delta^E_{mean} &= 0.17 \text{ mm} \end{aligned} \tag{5.20}$$

Maximum absolute values of

$$\begin{aligned} \Delta^N_{max} &= 3.0 \text{ mm} \\ \Delta^E_{max} &= 2.8 \text{ mm} \end{aligned} \tag{5.21}$$

are reached in this time period. If the gradients maximum influence on the delay does not exceed

$$\text{effect}\_\Delta^{N,\,slant} \le 1 \text{ mm} \tag{5.22}$$

they can be considered as negligible. In Northing, this is the case as long as the gradients attain up to $\Delta^N = 3$ mm at the mean SAR azimuth of about $110°$. Gradients up to 1.1 mm can be accepted in Easting if no gradient in Northing affects the delay. Within the whole year, at the four observing sites, about 1% of the observed gradients exceeded this threshold value. However, both the gradients in Northing and Easting have to be considered at a time to get a clear estimation of their total effect. The complete effect of both gradients can be deduced from

$$\text{effect}\_\Delta^{N\,\&\,E,\,slant} = -\Delta^N \cdot \cos\varepsilon \cdot \cos A - \Delta^E \cdot \cos\varepsilon \cdot \sin A = -\cos\varepsilon \left(\Delta^N \cdot \cos A + \Delta^E \cdot \sin A \right) \tag{5.23}$$

A maximum of effect_$\Delta^{N \& E, slant}$ is reached, if

$$
\frac{\partial \text{effect\_}\Delta^{N \& E, slant}}{\partial A} = 0 \qquad \Leftrightarrow \qquad -\Delta^{N} \cdot \sin A + \Delta^{E} \cdot \cos A = 0
$$

$$
\Delta^{E} \cdot \cos A = \Delta^{N} \cdot \sin A \qquad (5.24)
$$

$$
\frac{\Delta^{E}}{\Delta^{N}} = \tan A
$$

If the horizontal gradients in Northing and Easting are equal, their maximum effect is attained at azimuth angles of $A_1 = 45°$, $A_2 = 135°$, $A_3 = 225°$ or $A_4 = 315°$. An estimation based on gradients equaling $\Delta^{N} = 1$ mm and $\Delta^{E} = 1$ mm gives an idea of a possible effect. If the total effect of both gradients shall not exceed 1 mm, and if the azimuth angle equals 45° (if the worst case is assumed), the elevation may not be lower than $\varepsilon = 45°$.
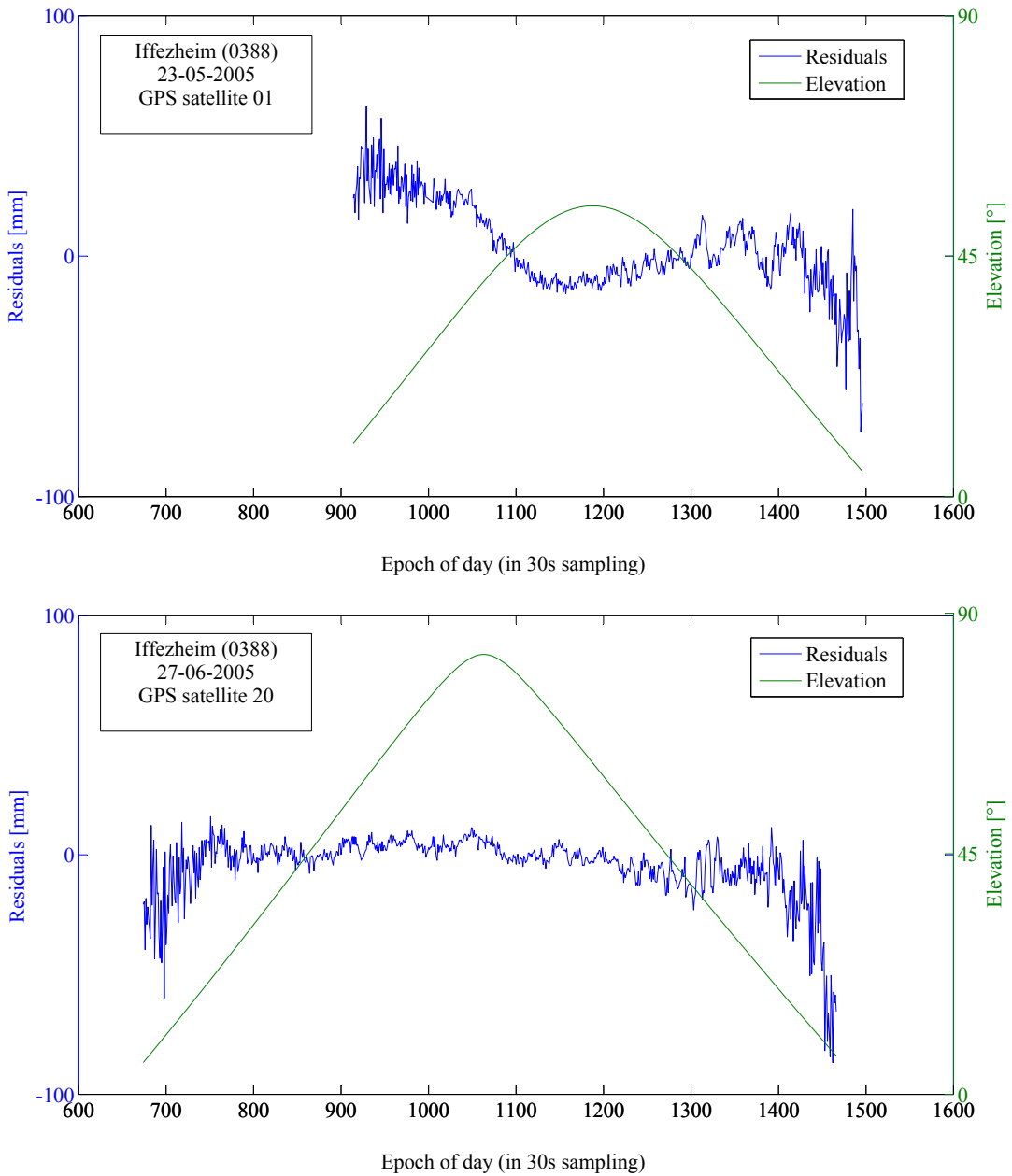
Figure 5.7: Real residuals (converted to L_1) of the satellites 01 and 20 observed from Iffezheim (0388); SAR acquisition time: between epochs 1183 and 1184; top: 23-05-2005; bottom: 27-06-2005

In reality, varying azimuth angles are considered and the two gradients differ. For these reasons, the estimation of the gradients influence becomes much more complex and a non-linear optimization problem has to be solved in order to estimate the minimum elevation at which the horizontal gradients may be neglected. Nevertheless, as no satellites appearing at elevations below $45°$ are included in this analysis, the horizontal gradients computed from observations down to $3°$ are assumed to be negligible.
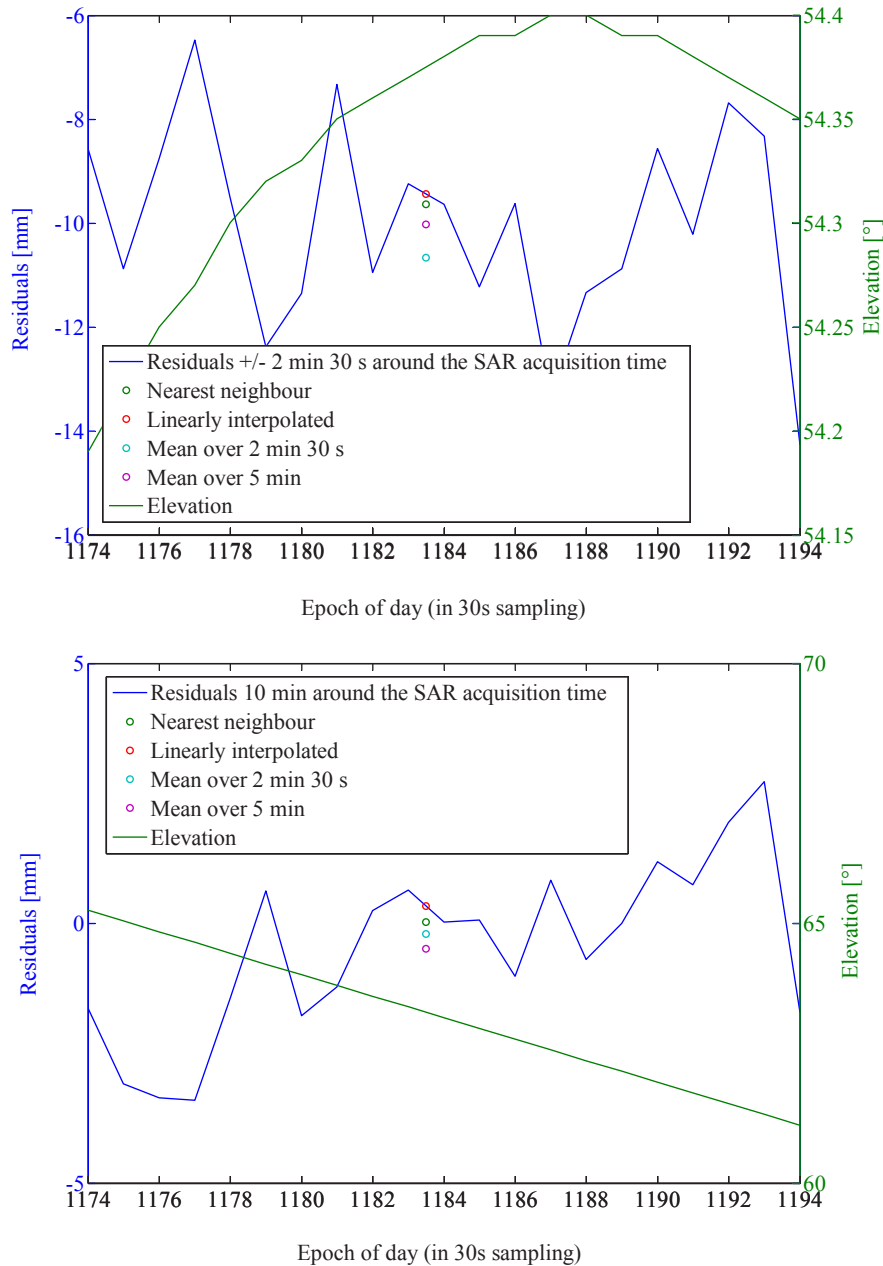
Figure 5.8: Residuals within 10 min around the SAR acquisition time; top: Iffezheim (0388) on 23-05-2005; bottom: Ludwigshafen (0520) on 27-06-2005

In contrast to the horizontal gradients, the estimated residuals have a higher effect on the total wet delay deduced from the GNSS data. Depending on the considered date and observing site, the residuals can change the total wet delay significantly. Within the least squares adjustment in Bernese, the residuals are supposed to follow an unbiased Gaussian distribution. Considering the whole day, this might be the case, but especially in case of shorter time periods, the residuals might deviate significantly from the zero mean. Their long-term trend is superposed by short-scale variations such as those in Figure 5.7. This is why the residuals were not introduced epoch-wise into

the computations. Instead, a temporal mean residual over 5 min around the SAR acquisition time was calculated. Comparative values for the temporal mean over 2 min 30 s, for a linear interpolation between the two closest epochs and for the nearest neighbor have also been analyzed. Their differences at two exemplary sites and dates are illustrated in Figure 5.8.

Comparing the phase residuals in Figure 5.6, large differences occur between the partial wet delays from InSAR and the differential wet delays from GNSS (represented, e.g., by the SSNP, the SSNP and the horizontal gradients, resp. the SSNP, the horizontal gradients, and the residuals). The reduction of the GNSS observations by a topography-dependent component and a linear trend as in the case of MERIS enables a more valid comparison. In this context, the studies of Alshawaf [2013] are recommended for more details. Instead of the linear model for the topography-dependent component applied for the MERIS observations in this thesis, Alshawaf [2013] uses the more sophisticated exponential approach

$$\Delta_{wet,\,topo}^{zenith}(H) = C \cdot \exp(-\alpha \cdot H) + H \cdot \alpha \cdot C \cdot \exp(-\alpha \cdot H) + \Delta_{wet,\,min}^{zenith} \qquad (5.25)$$

proposed by Onn and Zebker [2006]. Here, $\Delta_{wet,\,topo}^{zenith}(H)$ stands for the topography-dependent component of the zenith wet delay at a site of height H. C and α represent model parameters, and $\Delta_{wet,\,min}^{zenith}$ is the zenith wet delay observed at the site with the highest altitude. Alshawaf [2013] does not focus on the different satellite-directed contributions to the path delays but compares partial zenith wet delays from InSAR with comparable quantities deduced from the SSNP at ten observing sites within the SAR frame. In addition to her analyses, horizontal gradients and residuals are considered here besides the SSNP representing the mean neutrospheric characteristics within a cone over the considered site. In eleven out of 13 cases, the slant residuals lie within the 1σ interval around the partial InSAR wet delay, if σ stands for the standard deviation of the delay differences deduced from InSAR. Only the differential partial delays from master 07-02-2005 and slave 23-05-2005 at Iffezheim (0388) as well as those from master 27-06-2005 and slave 23-05-2005 at site Landau (0520) do not agree.

Yet, it has to be reminded that the residuals introduced into the computations are raw residuals resulting from Bernese. They have not been stacked as it is been done, e.g., for the determination of neutrospheric water vapor by Fuhrmann et al. [2010] or in Knöpfler et al. [2014]. In this regard, the term "stacking" shall denote a directional analysis of the phase residuals within a hemisphere subdivided in cells. Such an analysis is usually performed based on the residuals of several successive days. If the mean value of the residuals falling within a cell deviate systematically and significantly from zero as in some cases in Figure 5.9, this is assumed to be due to site-specific effects such as multipath or errors in the antenna model.
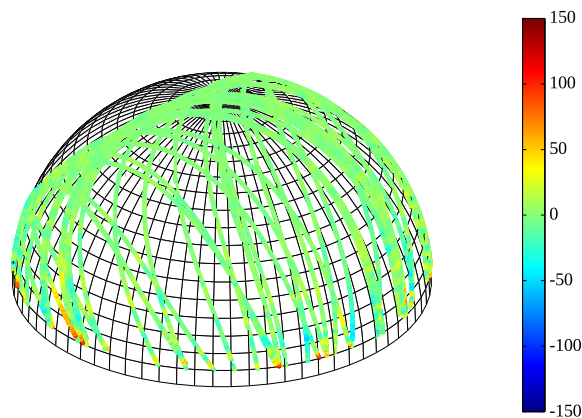
Figure 5.9: 3D stacking map for the observing site Stuttgart (0384) from Knöpfler et al. [2014]; raw residuals from a PPP processing of *DOY* 199 2013 [mm]

Based on these analyses of the residuals, corrections can be introduced into the Bernese processing. Figure 5.10 summarizes this iterative process. The stacking procedure consists of different (at least two) processing steps.

First, phase residuals are computed within Bernese. This is done for all considered sites and several following days. Only in case of no systematic errors due to e.g., multipath resp. antenna model within one cell, the mean of the residuals within this cell is assumed to equal zero. Consequently, all those stacking cells deviating from zero mean can be considered as affected by multipath effects or inaccurate antenna calibrations. According to Knöpfler et al. [2014], the obtained stacking map is then, in a second step, introduced as correction into a second Bernese processing. This results in phase residuals less affected by the site-specific effects mentioned above. This stacking procedure may be repeated iteratively. While Knöpfler et al. [2014] is aiming at improved coordinate time series, their strategy is able to improve the residuals contribution to water vapor exploitations based on GNSS as well.
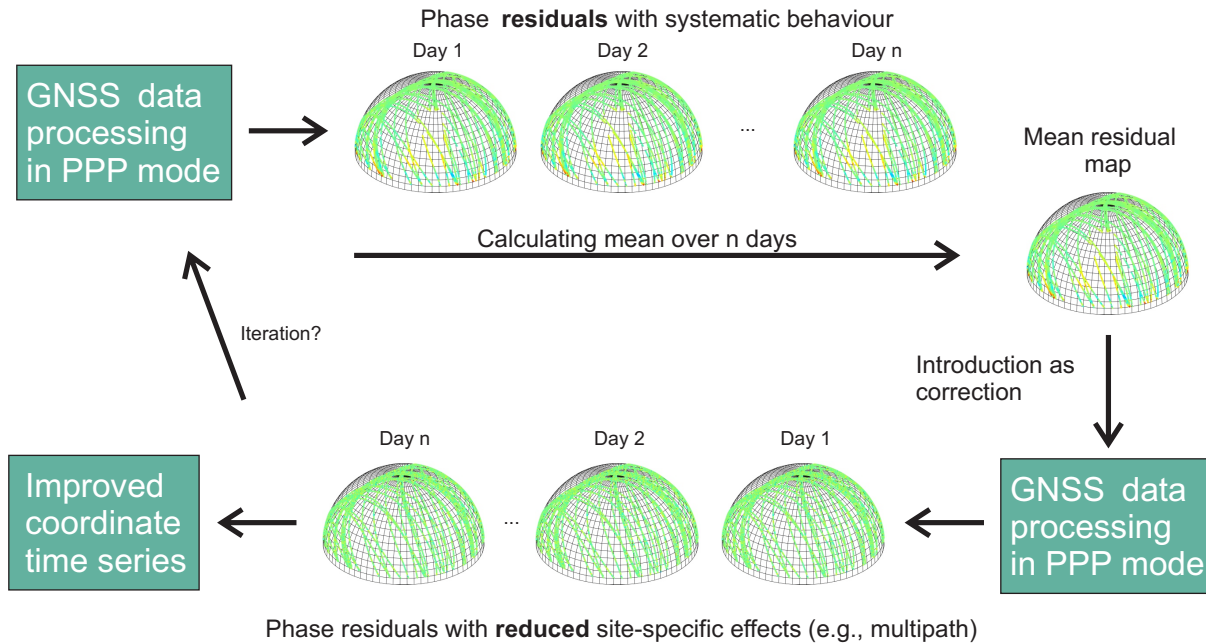
Figure 5.10: Scheme of stacking procedure within GNSS data processing from Knöpfler et al. [2014]

Besides the projects of Knöpfler et al. [2014] and that of Alshawaf [2013] carried out at GIK and IPF, Song et al. [2008] and Cheng et al. [2011] use a similar approach as Alshawaf [2013] to model InSAR atmospheric signals using GPS data based on a topography-dependent and turbulent-mixing model. In contrast, van Hoeven et al. [2002] assume a model of a frozen atmosphere moving with the prevailing wind in order to convert GPS time series to spatial zenith delay profiles. By doing that, they overcome the restriction of GPS to pointwise observations.

5.4 Summary

In this chapter, the viewing geometries of GNSS and InSAR were compared. Particular attention was paid to the spatial averaging in GNSS. Due to spatial averaging in GNSS, the InSAR observations have to be averaged within a region of about 38 km $\times$ 38 km. As the GNSS cutoff elevation angle ε_{min} determining the spatial averaging shall not be increased, a reduction of the interpolation region for the InSAR data is not possible. The definition of search windows for GNSS satellites situated "close" to the Envisat satellite during the InSAR observation represents a big challenge. This can be explained by the different orbits of GNSS and Envisat and the necessity of both a temporal and a spatial closeness of the two satellites. A final comparison of the contributions of GNSS and InSAR to the wet delay showed that the horizontal gradients from GNSS are insignificant at the considered elevation of $\varepsilon > 45°$. Furthermore, the SSNP turned out to attain important values, even though they do not yield any directional information. The phase residuals from GNSS represents a significant and non-isotropic contribution of GNSS to the wet delay. In eleven out of 13 cases of the described case study, the partial wet delays from InSAR corresponded within a 1σ-interval to the phase residuals from GNSS.

6 Outlook

In the future, the SAR incidence angle θ, set to a constant value of $23.5°$ for this analysis, should be adapted to the respective viewing geometry. In section 4.3.1, it has been recognized that this angle varies between $18.6°$ and $26.2°$ from near range to far range. Assuming a slant wet delay of 20 mm, zenith wet delays of 19.0 mm and 17.9 mm are obtained for $\theta = 18.6°$ and $\theta = 26.2°$. Depending on the incidence angle, the wet delays obtained in zenith direction change by more than one millimeter. Therefore, the correct value of θ increasing from near range to far range should be used for any further studies.

Also, the determination of the scaling factor Π used for the conversion from IWV to zenith wet delays is essential for rigorous comparisons. The atmospheric mean temperature depends strongly on topography. The higher a meteorological observing site is situated, the lower is the measured temperature. For this reason, the rule of thumb setting Π to 0.15 should not be used. In contrast, a determination of Π based on data deduced from meteorological observing sites as in this study or from the Weather Research and Forecasting model (WRF) is mandatory. Section 4.3.2 showed that imprecise values of T_m introduced into the determination of Π cause significant changes in the resulting wet delay.

The consideration of more GNSS sites within the SAR frame is recommended for future studies. Moreover, the temporal search window for the comparison of the satellite-directed contributions of GNSS and InSAR to the wet delay can be extended to, for example, five minutes. An analysis within this time interval would still represent comparable atmospheric characteristics, although it would be extended up to 10 minutes when considering that the used residuals are averaged over five minutes, respectively. Both the use of more observing sites as well as the larger temporal search window would increase the number of "close" satellites. Of course, a larger sample yields more representative information. Moreover, the computation of the contributions of more GNSS sites to the wet delay enables a least squares estimation of the topography-dependent component and of the linear trend contained in the GNSS observations as in Alshawaf [2013]. Here, future analyses might also take advantage of the upcoming European GNSS Galileo, its standard of multi-frequency observations, and the increasing number of satellites that facilitates the search of "close" satellites.

In this context, a critical review of the maximum accepted size of the search window is recommended. Here, a deviation of up to 250 m at a height of 1 km has been accepted for the line-of-sight to the GPS satellite with respect to the position of the SAR satellite during its acquisition. However, a smaller search window might yield more precise results, but the priority is set to a reduction of the averaging area of the InSAR observations. So far, mean values computed from all those PS points lying within a rectangular area of 38 km $\times$ 38 km have been introduced into the analysis. The size of the averaging region depends on the selected minimum cutoff GNSS elevation ε_{min}. Of course, this minimum elevation may be increased to $5°$ or $7°$. However, there is no silver bullet for the choice of ε_{min}. The higher the minimum elevation, the smaller becomes the averaging region in InSAR. In contrast, the higher ε_{min}, the more difficult becomes the decorrelation of height and neutrospheric delay observed by GNSS.

Another remaining issue concerns the negligence of the horizontal gradients. At the considered elevation angles, this contribution of GNSS to the wet delay has been graded as having no significant influence on the total wet delay. This raises the question whether the information contained in the gradients would a) be lost or b) still be included in other contributions to the wet delay, in case of their omission within the processing. Here, the gradients are part of the least squares estimation and simply omitted afterwards during the reconstruction of the total wet delay. However, if from the very beginning no gradients are introduced into the adjustment, their effect might, for example, be contained in the resulting residuals.

Finally, future work should aim at a validation of the results with data deduced from WRF and use more sophisticated models for the topography-dependent component of the wet delay. Solutions for the separation of the neutrospheric phase from other phase components contained in the InSAR observations shall be developed for regions affected by deformation. With the development of the new European GNSS Galileo, the spatial resolution of ionosphere-free GNSS observations might easily be improved by establishing a dense network of simple low-cost receivers. The new Sentinel-1 mission assuring C-band SAR data continuity will dispose of a 12 days repeat orbit cycle for one satellite or of a six days repeat cycle within the constellation of the two satellites. In this way, the temporal resolution of InSAR will be improved, too. Hereby, the future potential in this field is great, and both geodetic positioning and climate research or weather forecasting can benefit of it.

A Main steps and settings within the processing in Bernese

The processing of the GPS observations has been performed with Berner GPS Software Version 5.2. This tool uses different panels allowing the user to select or to enter the necessary input files or values. The processing itself is then implemented within a so-called Bernese Processing Engine (BPE) consisting of all required panels arranged in an order that is pre-defined by the user. Depending on the panels, parallel or sequential processing of the respective panels is possible or not. Here, the sequence shown in Figure A.1 is applied.

nb	panel	from folder		nb	panel	from folder
1	GS01_COP	GS01GEN		20	PPPEDTAP	GS01GEN
2	DUMMY	GS01GEN		21	PPPEDT_P	GS01GEN
3	POLUPDH	GS01GEN		22	GPSXTR	GS01GEN
4	ORBMRGH	GS01GEN		23	PPPRESAP	GS01RES
5	PRETAB	GS01GEN		24	PPPRES_P	GS01RES
6	ORBGENH	GS01GEN		25	RESFMT	GS01RES
7	CCRNXCH	GS01GEN		26	RES_SUM	GS01AUX
8	RNXCLK	GS01GEN		27	CRDMERGE	GS01AUX
9	DUMMY	NO_OPT		28	ADDNEQ2	GS01AUX
10	RNXGRA	GS01GEN		29	PPP_HLM	GS01AUX
11	RNXSMTAP	GS01GEN		30	CCRNXC	GS01AUX
12	RNXSMT_H	GS01GEN		31	ADDNEQ2	GS01SNX
13	RXOBV3AP	GS01GEN		32	DUMMY	NO_OPT
14	RXOBV3_H	GS01GEN		33	GS01_SUM	GS01GEN
15	CRDMRDAT	GS01GEN		34	GS01_SAV	GS01GEN
16	CODSPPAP	GS01GEN		35	GS01_DEL	GS01GEN
17	CODSPP_P	GS01GEN		36	BPE_CLN	GS01GEN
18	CODXTR	GS01GEN		37	DUMMY	NO_OPT
19	DUMMY	NO_OPT				

Figure A.1: Selected panels within the processing in Bernese

The two panels CODSPP.INP and GPSEST.INP are of particular interest for neutrospheric modeling. The latter panel does not directly appear in the list in Figure A.1 but is used within PPPEDT_P. The settings within COD-SPP.INP are needed for the code processing during which the receiver clock is synchronized with the GPS time, approximate coordinates are estimated, and outliers are detected. Here, special attention has to be paid to the following settings, where the bold options correspond to those options that have been selected for the comparison of the effects of NMF and VMF in 3.4:

1	Filenames:	Input Files:	in the case of VMF: **Maps of VMF1 coeff.** / else: **-**
2	Input Options:	Parameters:	Frequency: L_1, L_2 or $\boldsymbol{L_3}$
3	Input Options:	Observation Selection:	Minimum elevation: **3 degrees**

Within PPPEDT_P the parameter estimation is performed during the run of GPSEST.INP, outliers are detected, and the parameter estimation in GPSEST.INP is then repeated. As a result, the settings in GPSEST.INP are of

interest for the derivation of neutrospheric parameters. All those parts of the input file GPSEST.INP that have to be considered in particular are indicated in the following. The bold options correspond again to the selected options.

1.1 Input Files 1:

– General Files and Processing Mode: Differencing level: DOUBLE, **ZERO**

– Main Input Files: in the case of VMF: **Gridded VMF1 coefficients**

3.1 General Options 1: Observation Selection:

– Frequency/linear combination: L_1, L_2, $\mathbf{L_3}$, L_4, L_5, L_1&L_2, L_3&L_4, MELWUEBB, DTEC

– Elevation cutoff angle: **3 degree**

– Elevation-dependent weighting: NONE, **COSZ**, COS2Z, COS2C

– Type of computed residuals: REAL, **NORMALIZED, modified according to section 3.5**, NORM_APRIORI

3.2 General Options 2: A Priori Troposphere Modeling:
ZPD model and mapping function: NONE, VMF, **DRY_VMF**, GMF, DRY_GMF,
NIELL, **DRY_NIELL**, SAASTAMOINEN,
DRY_SAAST, HOPFIELD

6.1.1 Site-Specific Troposphere Parameters 1:

– Zenith Path Delay Parameters: Mapping function: **WET_VMF**, DRY_VMF, WET_GMF, DRY_GMF, **WET_NIELL**, DRY_NIELL, COSZ, HOPFIELD

– Horizontal Gradient Parameters: NONE, TANZ, **CHENHER**, TILTING, LINEAR

Moreover, the copy script GS01_COP has been completed by adding a line copying the grid files for the Vienna mapping function from the datapool area

DATAPOOL/VMF1/VMFG_yyyyDOY.GRD

to the active campaign

G_ST01/GRD/VMFG_yyyyDOY.GRD.

As illustrated in Figure A.2, the final values for the neutrospheric delay estimated within GPSEST.INP result from the computations of several subroutines called by TDELAY.f90.
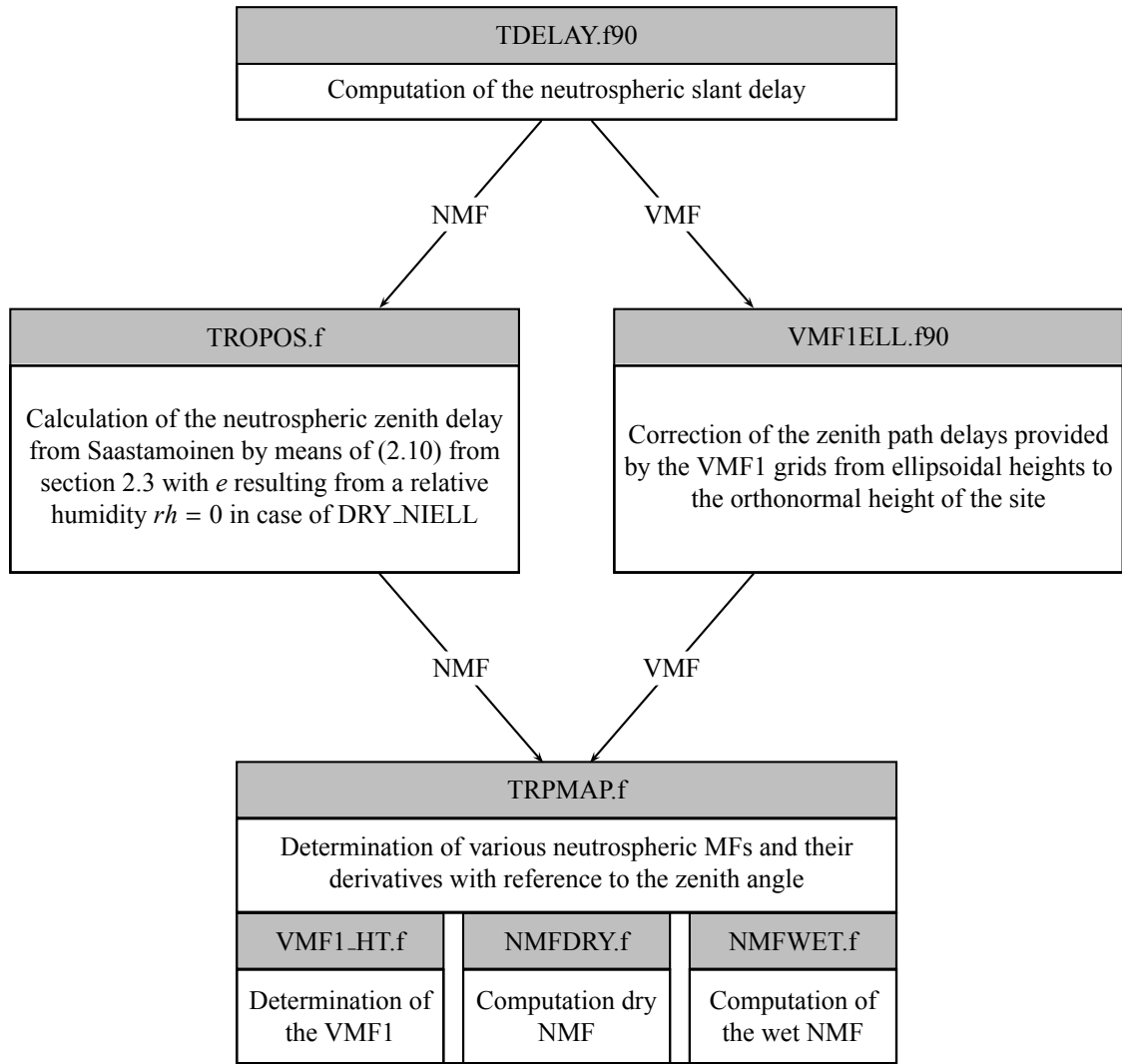
Figure A.2: Flowchart of the neutrospheric delay estimation within Bernese

Bibliography

Alshawaf, F. (2013). *Constructing water vapor maps by fusing InSAR, GNSS, and WRF data*. PhD thesis, Karlsruhe Institute of Technology, Karlsruhe.

Bauer, M. (2011). *Vermessung und Ortung mit Satelliten*. Wichmann, Berlin.

Berg, H. (1948). *Allgemeine Meteorologie*. Dümmler Verlag, Bonn.

Bevis, M., Businger, S., Chiswell, S., Herring, T. A., Anthes, R. A., Rocken, C., and Ware, R. H. (1994). GPS meteorology: Mapping zenith wet delays onto precipitable water. *Journal of Applied Meteorology*, 33(3):379–386.

Bevis, M., Businger, S., Herring, T. A., Rocken, C., Anthes, R. A., and Ware, R. H. (1992). GPS meteorology: Remote sensing of atmospheric water vapor using the Global Positioning System. *Journal of Geophysical Research: Atmospheres (1984–2012)*, 97(D14):15787–15801.

Boehm, J. (2004). *Troposphärische Laufzeitverzögerungen in der VLBI*. Geowissenschaftliche Mitteilungen 68.

Boehm, J. (2010). Readme file (vmf). http://ggosatm.hg.tuwien.ac.at/DELAY/readme.txt. 08.07.2014.

Boehm, J. and Schuh, H. (2003). Vienna mapping functions. In *Proceedings of the 16th Working Meeting on European VLBI for Geodesy and Astrometry*, pages 131–143.

Boehm, J. and Schuh, H. (2004). Vienna mapping functions in VLBI analyses. *Geophysical Research Letters*, 31(1).

Boehm, J. and Schuh, H. (2013). *Atmospheric Effects in Space Geodesy*. Springer.

Boehm, J., Werl, B., and Schuh, H. (2006). Troposphere mapping functions for GPS and VLBI from European Centre for Medium-Range Weather Forecasts operational analysis data. *Journal of Geophysical Research: Solid Earth*, 111(B2).

Cheng, S., Perissin, D., Chen, F., and Lin, H. (2011). Atmospheric delay analysis from GPS and InSAR. In *Geoscience and Remote Sensing Symposium (IGARSS), 2011 IEEE International*, pages 1650–1653.

Dach, R., Hugentobler, U., Fridez, P., and Meindl, M. (2007). *User manual of the Bernese GPS Software Version 5.0*. Astronomical Institute, University of Berne, Berne.

Doin, M.-P., Lasserre, C., Peltzer, G., Cavalié, O., and Doubre, C. (2009). Corrections of stratified tropospheric delays in SAR interferometry: Validation with global atmospheric models. *Journal of Applied Geophysics*, 69(1):35–50.

ESA (2006). *MERIS Product Handbook 2.1*. European Space Agency.

Fischer, J. and Bennartz, R. (1997). Retrieval of total water vapour content from MERIS measurements. *Algorithm Theoretical Basis Document PO-TN-MEL-GS-0005*.

Forssell, B. (2008). *Radionavigation Systems*. GNSS Technology and Applications Series. Artech House, Boston.

Fuhrmann, T., Heck, B., Knöpfler, A., Masson, F., Mayer, M., Ulrich, P., Westerhaus, M., and Zippelt, K. (2013). Recent surface displacements in the Upper Rhine Graben - Preliminary results from geodetic networks. *Tectonophysics*, 602(0):300 – 315.

Fuhrmann, T., Knöpfler, A., Mayer, M., Luo, X., and Heck, B. (2010). *Zur GNSS-basierten Bestimmung des atmosphärischen Wasserdampfgehalts mittels Precise Point Positioning (KIT Scientific Reports; 7561)*. KIT Scientific Publishing, Karlsruhe.

Heck, B. (2003). *Rechenverfahren und Auswertemodelle der Landesvermessung: klassische und moderne Methoden*. Wichmann, Heidelberg, 3rd edition.

Hofmann-Wellenhof, B., Lichtenegger, H., and Collins, J. (2001). *GPS: Theory and Practice*. Springer, Wien.

Holzner, J., Eineder, M., and Schättler, B. (2002). First analysis of Envisat/ASAR image mode products for interferometry. *Envisat Calibration Review*.

Hooper, A., Segall, P., and Zebker, H. (2007). Persistent scatterer interferometric synthetic aperture radar for crustal deformation analysis, with application to Volcán Alcedo, Galápagos. *Journal of Geophysical Research: Solid Earth (1978–2012)*, 112(B7).

Hooper, A., Spaans, K., Bekaert, D., Cuenca, M. C., Arikan, M., and Oyen, A. (2010). *StaMPS/MTI Manual*. Delft Institute of Earth Observation and Space Systems, Delft University of Technology.

Hooper, A., Zebker, H., Segall, P., and Kampes, B. (2004). A new method for measuring deformation on volcanoes and other natural terrains using InSAR persistent scatterers. *Geophysical Research Letters*, 31(23).

Knöpfler, A., Masson, F., Mayer, M., Ulrich, P., and Heck, B. (2010). GURN (GNSS Upper Rhine Graben Network) – Status and First Results. *FIG Congress 2010 – Facing the Challenges – Building the Capacity*. Sydney.

Knöpfler, A., Mayer, M., and Heck, B. (2014). Using stacking to reduce site-specific errors and to improve quality of GNSS-based coordinate time series within GURN (GNSS Upper Rhine Graben Network). *74. Jahrestagung der Deutschen Geophysikalischen Gesellschaft; Geodäsie/Fernerkundung; Poster 001*.

Kouba, J. (2008). Implementation and testing of the gridded Vienna Mapping Function 1 (VMF1). *Journal of Geodesy*, 82(4-5):193–205.

Kraus, H. (2004). *Die Atmosphäre der Erde: Eine Einführung in die Meteorologie*. Springer, Berlin.

Leick, A. (2004). *GPS Satellite Surveying*. Wiley, Hoboken, NJ.

Lindenbergh, R., Keshin, M., van der Marel, H., and Hanssen, R. (2006). Combining water vapor data from GPS and MERIS. *ISPRS Commission VII Mid-term Symposium Remote Sensing: "From Pixels to Processes"*, pages 8–13.

Malberg, H. (2007). *Meteorologie und Klimatologie: Eine Einführung*. Springer, Berlin, Heidelberg.

Massonnet, D., Feigl, K., Rossi, M., and Adragna, F. (1994). Radar interferometry mapping of deformation in the year after the Landers earthquake. *Nature*, 369:227–230.

Mayer, M. (2006). *Modellbildung für die Auswertung von GPS-Messungen im Bereich der Antarktischen Halbinsel*. PhD thesis, Deutsche Geodätische Kommission, C, 597.

Moreira, A. (2000). *Radar mit synthetischer Apertur – Grundlagen und Signalverarbeitung*. Oldenbourg Verlag, München. Habilitation.

Nafisi, V., Madzak, M., Boehm, J., Ardalan, A. A., and Schuh, H. (2012). Ray-traced tropospheric delays in VLBI analysis. *Radio Science*, 47(2).

Niell, A. (1991). Vertical change and atmosphere correction in VLBI. In *AGU Chapman Conference Proceedings on Geodetic VLBI: Monitoring Global Change, NOAA Tech. Rep. NOS 137 NGS*, volume 49, pages 147–158.

Niell, A. E. (1996). Global mapping functions for the atmosphere delay at radio wavelengths. *Journal of Geophysical Research: Solid Earth*, 101(B2):3227–3246.

Onn, F. and Zebker, H. A. (2006). Correction for interferometric synthetic aperture radar atmospheric phase artifacts using time series of zenith wet delay observations from a GPS network. *Journal of Geophysical Research: Solid Earth*, 111(B9).

Prasad, R. and Ruggieri, M. (2005). *Applied Satellite Navigation Using GPS, GALILEO, and Augmentation Systems*. Artech House, Boston.

Rocken, C., Van Hove, T., and Ware, R. (1997). Near real-time GPS sensing of atmospheric water vapor. *Geophysical Research Letters*, 24(24):3221–3224.

Rohde, R. A. Atmospheric transmission.
http://www.globalwarmingart.com/wiki/File:Atmospheric_Transmission_png. (09.03.2014).

Saastamoinen, J. (1973). Contributions to the theory of atmospheric refraction. *Bulletin géodésique*, 107(1):13–34.

Seeber, G. (2003). *Satellite Geodesy*. de Gruyter, Berlin.

SIDC. Monthly Sunspot Numbers from the Solar Influences Data Analysis Center.
http://wattsupwiththat.files.wordpress.com/2012/03/sidc_ssn1976-2012.png. (27.02.2014).

Song, X., Li, D., and Liao, M. (2008). Reproduction of InSAR atmospheric signal using GPS data based on topography-dependent and turbulent mixing model. *Proceedings of the Dragon Programme Final Results*.

Torge, W. (2001). *Geodesy*. de Gruyter, Berlin.

van Hoeven, A., Hanssen, R. F., and Ambrosius, B. (2002). Tropospheric delay estimation and analysis using GPS and SAR interferometry. *Physics and Chemistry of the Earth, Parts A/B/C*, 27:385 – 390. Geodesy and Meteorology.

Wanninger, L. (2000). *Präzise Positionierung in regionalen GPS-Referenzstationsnetzen*. Deutsche Geodätische Kommission, C, 508. München. Habilitation.

Xu, G. (2003). *GPS: Theory, Algorithms, and Applications*. Springer, Berlin.

Zebker, H. A., Rosen, P. A., and Hensley, S. (1997). Atmospheric effects in interferometric synthetic aperture radar surface deformation and topographic maps. *Journal of Geophysical Research*, 102(B4):7547–7563.

SCHRIFTENREIHE DES STUDIENGANGS GEODÄSIE UND GEOINFORMATIK

Die Bände sind unter www.ksp.kit.edu als PDF frei verfügbar oder als Druckausgabe bestellbar.
(ISSN 1612-9733)

2003/1   **Daniel Koenig, Kurt Seitz**
Numerische Integration von Satellitenbahnen unter Berücksichtigung der Anisotropie
des Gravitationsfeldes der Erde. 2003
ISBN 3-937300-00-7

2004/1   **Marcus Ulrich Schmidt**
Objektorientierte Modellierung zur geodätischen Deformationsanalyse. 2004
ISBN 3-937300-06-6

2005/1   **Stephan Kupferer**
Anwendung der Total-Least-Squares-Technik bei geodätischen Problemstellungen. 2005
ISBN 3-937300-67-8

2007/1   **Andreas Knöpfler, Michael Mayer, André Nuckelt, Bernhard Heck, Günter Schmitt**
Untersuchungen zum Einfluss von Antennenkalibrierwerten auf die Prozessierung
regionaler GPS-Netze. 2007
ISBN 978-3-86644-110-1

2007/2   **Xiaoguang Luo, Miachel Mayer, Bernhard Heck**
Bestimmung von hochauflösenden Wasserdampffeldern unter
Berücksichtigung von GNSS-Doppeldifferenzresiduen. 2007
ISBN 978-3-86644-115-6

2007/3   **Michael Mürle**
Aufbau eines Wertermittlungsinformationssystems. 2007
ISBN 978-3-86644-116-3

2007/4   **Heinrich Derenbach, Michael Illner, Günter Schmitt, Martin Vetter, Siegrfied Vielsack**
Ausgleichsrechnung – Theorie und aktuelle Anwendungen aus der Vermessungspraxis. 2007
ISBN 978-3-86644-124-8

2007/5   **André Nuckelt**
Dreidimensionale Plattenkinematik. 2007
ISBN 978-3-86644-152-1

2007/6   **Hermann Bähr, Zuheir Altamimi, Bernhard Heck**
Variance Component Estimation for Combination of Terrestrial Reference Frames. 2007
ISBN 978-3-86644-206-1

2009/1   **Cornelia Eschelbach**
Refraktionskorrekturbestimmung durch Modellierung des Impuls-
und Wärmeflusses in der Rauhigkeitsschicht. 2009
ISBN 978-3-86644-307-5

SCHRIFTENREIHE DES STUDIENGANGS GEODÄSIE UND GEOINFORMATIK

2009/2   **Bernhard Heck, Michael Mayer (Hrsg.)**
Geodätische Woche 2009
22.–24. September 2009, Messe Karlsruhe, Rheinstetten im Rahmen der INTERGEO –
Kongress und Fachmesse für Geodäsie, Geoinformation und Landmanagement. Abstracts. 2009
ISBN 978-3-86644-411-9

2010/1   **Thomas Grombein, Kurt Seitz, Bernhard Heck**
Untersuchungen zur effizienten Berechnung topographischer Effekte auf
den Gradiententensor am Fallbeispiel der Satellitengradiometriemission GOCE. 2010
ISBN 978-3-86644-510-9 / KIT Scientific Reports 7547

2010/2   **Thomas Fuhrmann, Andreas Knöpfler, Michael Mayer,**
Xiaoguang Luo, Bernhard Heck
Zur GNSS-basierten Bestimmung des atmosphärischen Wasserdampfgehalts mittels Precise
Point Positioning. 2010
ISBN 978-3-86644-539-0 / KIT Scientific Reports 7561

2010/3   **Geodätisches Institut (Hrsg.)**
Vernetzt und ausgeglichen
Festschrift zur Verabschiedung von Prof. Dr.-Ing. habil. Dr.-Ing. E.h. Günter Schmitt. 2010
ISBN 978-3-86644-576-5

2012/1   **Michael Mayer, Claudia P. Krueger, Bernhard Heck (Hrsg.)**
Highly Precise Positioning and Height Determination using GPS. Results of a
PROBRAL project by Universidade Federal do Paraná (UFPR, Curitiba, Brazil)
and Karlsruhe Institut für Technologie. 2012
KIT Scientific Reports 7604

2013/1   **Melanie Müßle, Bernhard Heck, Kurt Seitz, Thomas Grombein**
Untersuchungen zur planaren Approximation im Geodätschen Randwertproblem. 2013
ISBN 978-3-7315-0095-7 / KIT Scientific Reports 7652

2013/2   **Hermann Bähr**
Orbital Effects in Spaceborne Synthetic Aperture Radar Interferometry. 2013
ISBN 978-3-7315-0134-3

2014/1   **Marion Heublein**
Towards a rigorous fusion of GNSS and InSAR observations for the purpose of water vapor
retrieval. 2014
ISBN 978-3-7315-0270-8

SCHRIFTENREIHE DES STUDIENGANGS GEODÄSIE UND GEOINFORMATIK

KARLSRUHER INSTITUT FÜR TECHNOLOGIE (KIT)

Incompletely or incorrectly modeled atmospheric effects limit the quality of the exploitation of observations of space-based geodetic sensors, such as GNSS (Global Navigation Satellite Systems) and InSAR (Interferometric Synthetic Aperture Radar). In contrast, state variables of the Earth's atmosphere, especially water vapor, contain valuable information for climate research and weather forecasting.

In the framework of the rigorous fusion of GNSS and InSAR observations, the presented work carries out at a straightforward comparison of the wet delay, caused by water vapor, derived from GNSS and InSAR. The contributions of the two sensors to the wet delay caused by water vapor are compared in the line of sight towards the SAR satellite. Therefore, the InSAR neutrospheric phase has to be separated from other components contained in InSAR measurements. Comparisons of GNSS observations with the satellite-directed InSAR data show that only a partial component of the wet delay remains after the interferogram formation.